Development of Industrial
n-PERT Rear Junction Solar Cells
with Screen-Printed Aluminum Point Contacts

vorgelegt von
Zih-Wei Peng
aus Taipeh/Taiwan

Declaration

I hereby declare that the work presented in this thesis has not been submitted
for any other degree or professional qualification, and that it is the result of
my own independent work.

Signature Doctoral Candidate

September, 2019

Date

Publications associated with this research

1. Peng, Z.-W., Buck, T., Theobald, J., Eibl, O., and Kopecek, R., "Investigation of laser contact opening pitch affecting the void formation on *n*-type rear emitter silicon solar cells," *Energy Procedia*, **2017**, *124*, 665–670.

2. Peng, Z.-W., Buck, T., Theobald, J., Mihailetchi, V.D., and Kopecek, R., " Laser ablation induced recombination losses of *n*-PERT-RJ solar cells with rear contacts formed by Al evaporation," in *Proceedings of 33rd European Photovoltaic Solar Energy Conference and Exhibition, Amsterdam, The Netherlands*, **2017**, 624–627.

3. Peng, Z.-W., Buck, T., Dörr, M., Hain, A., Nagel, H., Hartmann, P., Wohl fart, P., Kopecek, R., "Investigation of In-situ annealing during physical vapour deposition of Al rear contacts on *n*-PERT rear junction crystalline silicon solar cells," in *Proceedings of 33rd European Photovoltaic Solar Energy Conference and Exhibition, Amsterdam, the Netherlands*, **2017**, 600–603.

4. Cabrera, E., Schneider, A., Buck, T., Peng, Z.-W., Fischer, T., and Kopecek, R., "Advances in the development of a novel module design based on electrical conductive adhesive glue for contacting highly efficient *n*-type solar cells with PVD Al back contact," in *Proceedings of 33rd European Photovoltaic Solar Energy Conference and Exhibition, Amsterdam, the Netherlands*, **2017**, 1758–1761.

5. Peng, Z.-W., Nakahara, M., Buck, T., and Kopecek, R., "Towards 22% efficiency *n*-PERT rear junction solar cells with screen printed Al point back contact," *AIP Conference Proceedings*, **2018**, *1999(1),* 100002.

6. Hain, A., Nagel, H., Dörr, M., Buck, T., Peng, Z.-W., Lorenz, R., Fischer, T., Gledhill, S., Kroyer T., Huber M., Wohlfart, P., "PVD metallization for high-efficiency c-Si solar cells: scenario for implementation in production," in *Proceedings of 35th European Photovoltaic Solar Energy Conference and Exhibition, Brussels, Belgium*, **2018**, 810–813.

7. Kopecek, R., Peng, Z.-W., Buck, T., Comparotto, C., Mihailetchi, V.D., Koduvelikulathu, L.J., Libal J., Lossen, J., Nakahara, M., Tsuji, K., Dhamrin, and M., Jooss, W., "Low-cost standard nPERT solar cells towards 23% efficiency and 700mV voltage using Al paste technology," *Photovoltaics International,* **2019**, *42*, 74–84.

8. Peng, Z.-W., Buck, T., Koduvelikulathu, L.J., Mihailetchi, V.D., and Kopecek, R., "Industrial screen-printed *n*-PERT-RJ solar cells: efficiencies beyond 22% and open-circuit voltages approaching 700 mV," *IEEE Journal of Photovoltaics*, **2019**, *9(5)*, 1166–1174.

9. Peng, Z.-W., Nakahara, M., Buck, T., and Kopecek, R., "Investigation on Industrial screen-printed aluminum point-contact and its application in *n*-PERT rear junction solar cells," *IEEE Journal of Photovoltaics*, **2019**, *9(6)*, 1554–1562.

10. Peng, Z.-W., Buck, T., Koduvelikulathu, L.J., Joris, L., Mihailetchi, V.D., and Kopecek, R., "693 mV V_{OC} Industrial screen-printed n-PERT rear junction solar cells with stable efficiency beyond 22%," *AIP Conference Proceedings*, **2019**, *2147(1),* 100001.

Acknowledgements

I would like to thank:

Table of contents

List of figures

List of tables

List of symbols and abbreviations

[Si]	Silicon concentration
4PP	Four-point probe
Ag	Silver
Al	Aluminium
a-Si	Amorphous silicon
BB	Busbars
BBr$_3$	Boron tribromide
BO	Boron-oxygen
BOS	Balance of system
BSG	Borosilicate glass
CdTe	Cadmium telluride
CID	Carrier-induced degradation
CIGS	Copper indium gallium selenide
CoBo	Conductive boundary
COO	Cost of ownership
COP24	24th conference of the parties to the United Nations framework convention on climate change
c-Si	Crystalline silicon
Cz-Si	Czochralski-Si
d_{lateral}	Carriers travelling distance in the Al layer before reaching and being collected by the rear busbars
DuP	Dual printing
ECV	Electrochemical capacitance-voltage
EQE	External quantum efficiency
FELA	Free energy loss analysis
FF	Fill factor
FiT	Feed-in tariff
f_{m}	Metal contact fraction
FSF	Front surface field
H$_2$O$_2$	Hydrogen peroxide
H$_2$SO$_4$	Sulfuric acid
HCl	Hydrochloric acid
HF	Hydrofluoric acid
IBC	Interdigitated back contact
IQE	Internal quantum efficiency
ITRPV	International technology roadmap for photovoltaic
$J_{0,\text{ Bulk}}$	Bulk recombination current density
$J_{0,\text{ Emitter}}$	Passivated emitter recombination current density
$J_{0,\text{ FSF}}$	Passivated FSF recombination current density
$J_{0,\text{ Met (Ag)}}$	Ag contact-induced recombination current density
$J_{0,\text{ Met (Al)}}$	Al contact-induced recombination current density
$J_{0,\text{ Total}}$	Total recombination current density of the device
J_{SC}	Short-circuit current density

KOH	Potassium hydroxide
LCO	Laser contact opening
LCOE	Levelized cost of electricity
LeTID	Light and elevated temperature induced degradation
LFC	Laser-fired contact
LID	Light induced degradation
LSM	Laser scanning microscopy
mc-Si	Multicrystalline silicon
monoPoly	Monofacial deposition of poly-Si layer
$mono$-Si	Monocrystalline silicon
MPP	Maximum power point
NaOH	Sodium hydroxide
n-PERT-RJ	n-type passivated emitter and rear totally diffused rear junction
N_{surf}	Surface doping concentration
O_2	Oxygen
PECVD	Plasma-enhanced chemical vapor deposition
PERC	Passivated emitter and rear cell
PERL	Passivated emitter rear locally diffused solar cells
PERPoly	Passivated emitter and rear polysilicon
PERT	Passivated emitter and rear totally diffused
$POCl_3$	Phosphorus oxychloride
POLO	Poly-Si on oxide
p_r	Contact pitch on rear side
PR	Performance ratio
PSG	Phosphosilicate glass
PV	Photovoltaics
PVD	Physical vapor deposition
QE	Quantum efficiency
QSSPC	Quasi-Steady-State Photoconductance
r	Contact radius on rear side
R_{alloy}	Al-Si alloy resistance
$R_{c\text{-}Al}$	Contact resistance between Al-Si alloy and Al-doped p^+ region
R_L	Line resistance of Ag finger
R_S	Series resistance
$R_{sh\text{-}Al}$	Al sheet resistance
$R_{sheet, Emitter}$	Sheet resistance of boron-p^+ emitter
$R_{sheet, FSF}$	Sheet resistance of phos.-n^+ FSF
R_{shunt}	Shunt resistance
RSVR	Rear surface recombination velocity
RTP	Rapid thermal processing
SAM	Scanning acoustic microscopy
SE	Selective emitter
SEM	Scanning electron microscopy
Si-add	Silicon additives

SiN$_x$	Silicon nitride
SP	Single printing
SP-Al	Screen printed aluminium
SRH	Shockley-Read-Hall
STC	Standard test conditions
TLM	Transfer length method
TOPCon	Tunnel Oxide Passivating Contact
T$_{peak}$	Peak temperature
V_{OC}	Open-circuit voltage
w	Contact width on front side
wt%-Si	Weight percent silicon
ΔEta	Efficiency drop
ΔFF	FF loss
ΔR_S	R_S increment
ρ_b	Bulk resistivity
ρ_c	Specific contact resistivity
ρ_f	Contact resistivity on front side
ρ_r	Contact resistivity on rear side
τ_{bulk}	Bulk lifetime

Chapter 1: Introduction

1.1 Why solar photovoltaics

The CO_2 emissions target of 65g CO_2/kWh should be achieved by 2050[1–3] in order to honor the Paris Agreement[4]. The urgent need for a de-carbonization of the power sector was re-emphasized during the 24th session of the Conference of the Parties (COP24) meeting in Katowice, Poland in December 2018. The key role of solar photovoltaics (PV) in realizing this goal in a cost-effective manner is outlined in many 100% renewable energy scenarios[5–8]. The total global installed PV capacity in 2018 is over 0.5 TW and a global electricity generation share of 2.2%. In Fig. 1.1, it is predicted will pass the following milestones over the next 5 years: 600 GW in 2019, 900 GW in 2021 and 1.1 TW in 2022[9]. The long term target is to surpass 21.9 TW (up to 70% of the electricity generation) by 2050[10]. This huge installation increase was mainly due to the supply of high-quality PV technology around the world, the continuous manufacturing costs decline, and to being the lowest cost source of electricity.
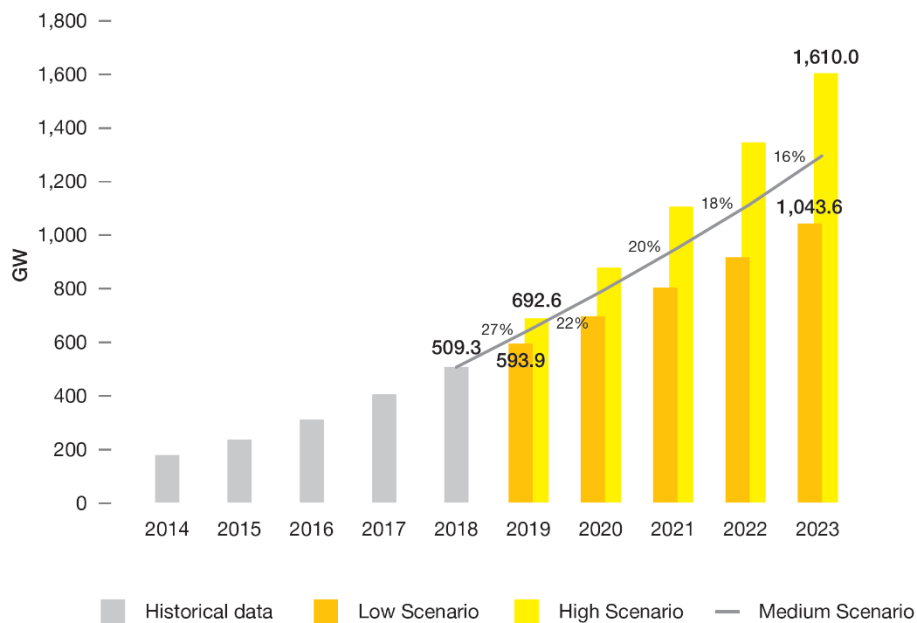
FIGURE 1.1. The word total solar PV market scenarios 2019-2023. (*Data source*: ref.[9])

1.2 PV installation and production

1.2.1 The global installations

In addition to China, the growth of PV deployments has shifted from government-driven incentive programs to market-driven investment decisions over the past two decades. 2018 will be remembered as the year solar broke the 100 GW threshold of annual installations (Fig. 1.2). And around 44% is contributed by China: a year-on-year decrease of 16% from the record additions of 52.8 GW and 53% growth in 2017. Figure 1.3 reveals that China added over four times more solar than the second largest market (US) in the world, and more than the remaining top 10 combined.
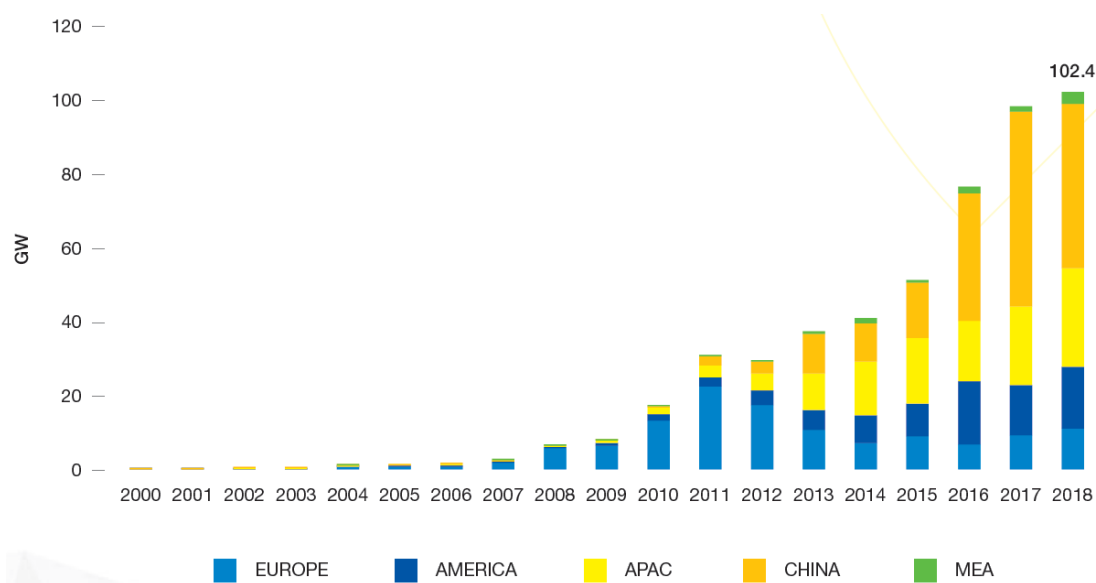
FIGURE 1.2. Evolution of the global annual solar PV installed capacity 2000-2018. (*Data source*: ref.[9])
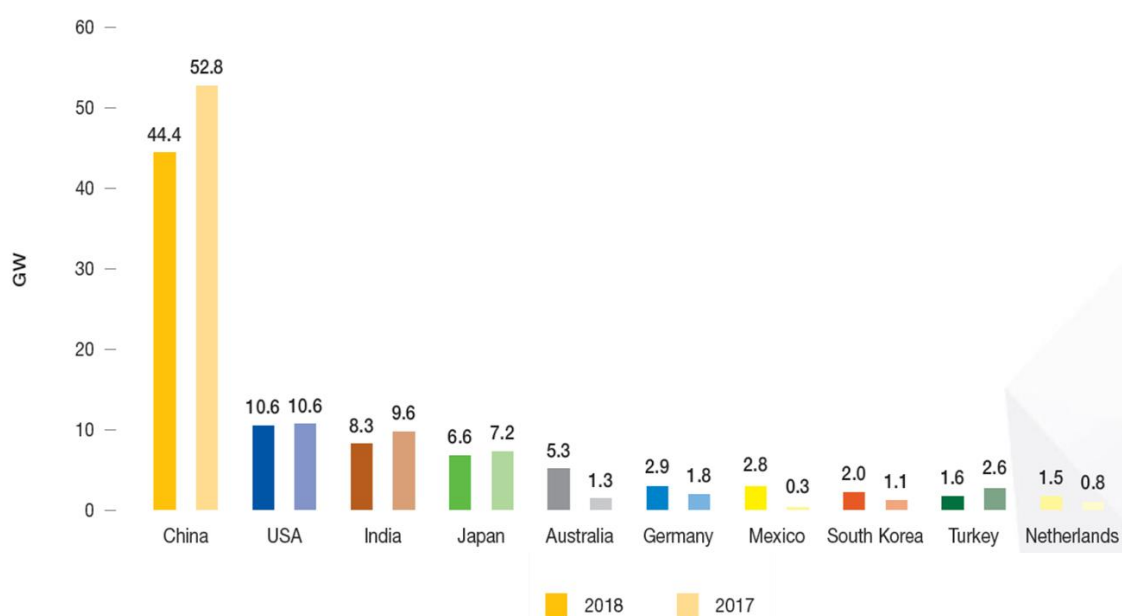
FIGURE 1.3. The global top 10 annual solar PV installed capacity in 2017 and 2018. (*Data source*: ref.[9])

1.2.2   The global productions

After discussing the PV market share in last section, the PV industry manufacturing is also being led by China since 2007 (Fig. 1.4). Production of PV devices (cell and module) has increased more than fivefold over the past decade. In 2017, Chinese PV manufacturing companies ranked among the top 10 in the world. The numbers are as follows: polysilicon - six companies; solar cells and solar modules - eight each, solar inverters - four (51 % market share)[11]. State subsidies may have played a decisive role in helping Chinese industry achieve the global leadership in solar photovoltaics. Despite serious uncertainties in the market, the PV module market remained stable in 2018. At the same time, the production capacity of c-Si PV has increased to approximately 150 GW[12]. Overcapacity has caused the average module price to drop significantly.
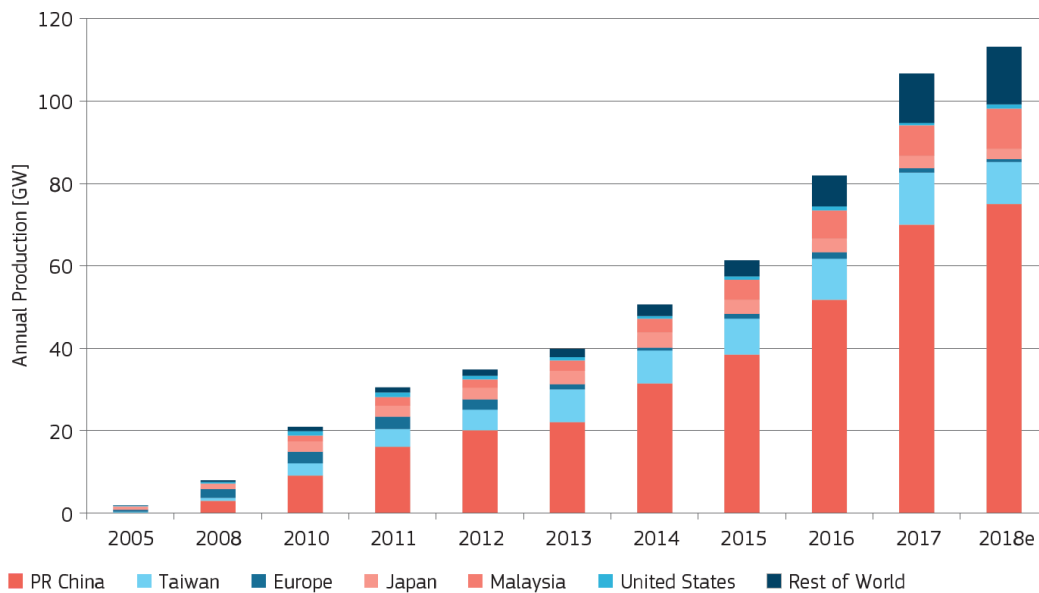
FIGURE 1.4. The global PV solar cell production from 2005 to 2018 (estimate). (*Data source*: ref.[11])

1.3   Solar cell technologies

1.3.1   Why crystalline silicon photovoltaics

Since the 1950s, crystalline silicon (c-Si) solar cells have dominated the photovoltaic market. The c-Si wafers for solar cell production continue to dominate the global PV manufacturing supply, partly because of the nontoxicity and abundance available in the earth's crust, as well as due to the crystalline structure[13], and the fact that c-Si PV modules have shown their long-term stability and longer lifespan over decades in practice. This is the key factor that

creates a huge demand for *c*-Si PV installation worldwide. At the end of 2018, the market share is more than 95%. Now, only two prominent companies are still pursuing thin-film based technologies: First Solar (Tempe, US) using cadmium telluride (CdTe) and Solar Frontier (Tokyo, Japan) with copper indium gallium selenide (CIGS)[14]. Figure 1.5 shows the global market share contributions from c-Si variants and thin-film production.
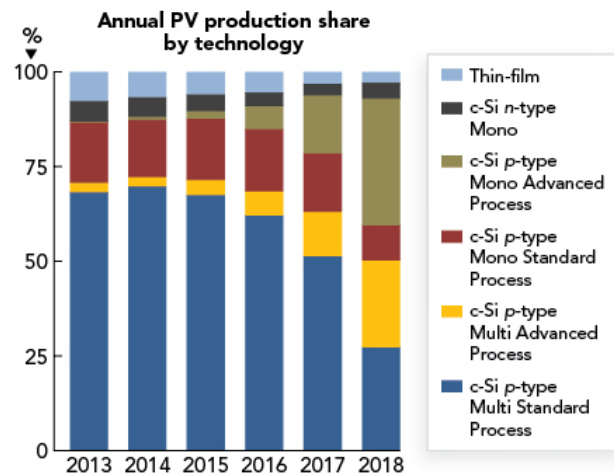
FIGURE 1.5. The silicon solar cells global production market share. Until 2016, standard processed *p*-type *mc*-Si solar cells dominated PV production; during 2017, *p*-type *mono*-Si cells have increased market-share contributions in addition to advanced process flows including PERC cells. (*Data source*: PV Module Tech, Malaysia 2018)

1.3.2   *c*-Si PV solar cell concepts

Since 2012, several cell concepts (e.g., PERC/PERT/PERL) using dielectric layer stack for rear-side passivation have been introduced to the production processes. In 2018, the PERC solar cell concept had a breakthrough in the market share. The IHS (Information Handling Services) Markit data indicated that for 2018 the PERX (e.g., PERC/PERT/PERL) solar cell concepts have around 45% market share in this near 150 GW production capacity[15]. In Fig. 1.6, the ITRPV predicts that PERX will gain significant market share and will enter the mainstream market after 2021[16].
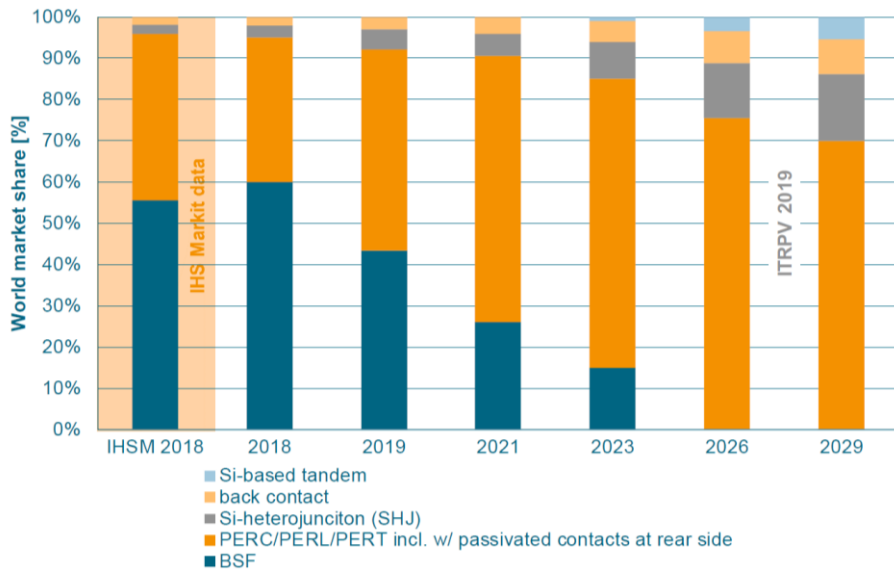
FIGURE 1.6. The global market share of different solar cell technologies. (*Data source*: ref[16])

1.4   Why *n*-type monocrystalline Si

1.4.1   Roadmap of market share and solar cell performance

It's predicted that from 2019, monocrystalline silicon (*mono*-Si) will replace the market share leadership of multicrystalline silicon (*mc*-Si)[16]. All silicon ingot crystallization capacity expansions are focusing on the "mono" variant, which has fewer defects than "multi", enabling the production of higher solar cell efficiencies. As shown in Fig. 1.7, *mono*-Si will attain an assumed share of 80% in 2029, and the *n*-type *mono*-Si will share half of it. There should have no cost difference between *p*-type and *n*-type wafers by then.
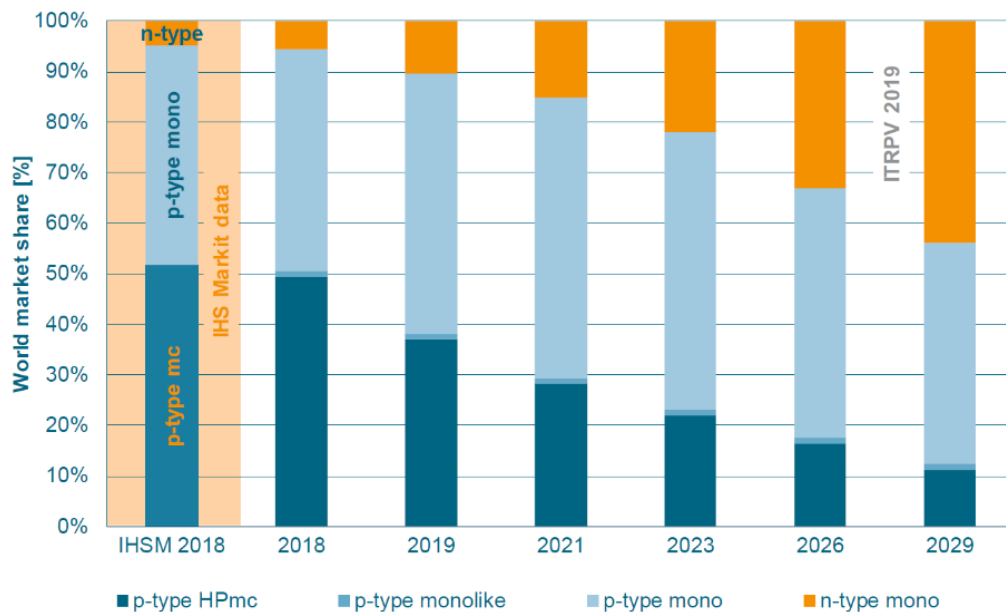
FIGURE 1.7. The global market share of different wafer types. (*Data source*: ref[16])

The wafer market share of *mc*-Si has dropped sharply because of the *mono*-Si PERX solar cell concepts replacing the traditional *mc*-BSF solar cell concept as the mainstream in the PV market. The mass production performance of the *p*-type PERC solar cells now is almost saturated. Shifting from *p*-type to *n*-type PERX solar cell concepts will be a solution for the manufacturing company achieving further higher solar cell efficiency and module output power. The efficiency of *n*-type PERX solar cell concepts are predicted 0.5% higher than *p*-type (see Fig. 1.8).
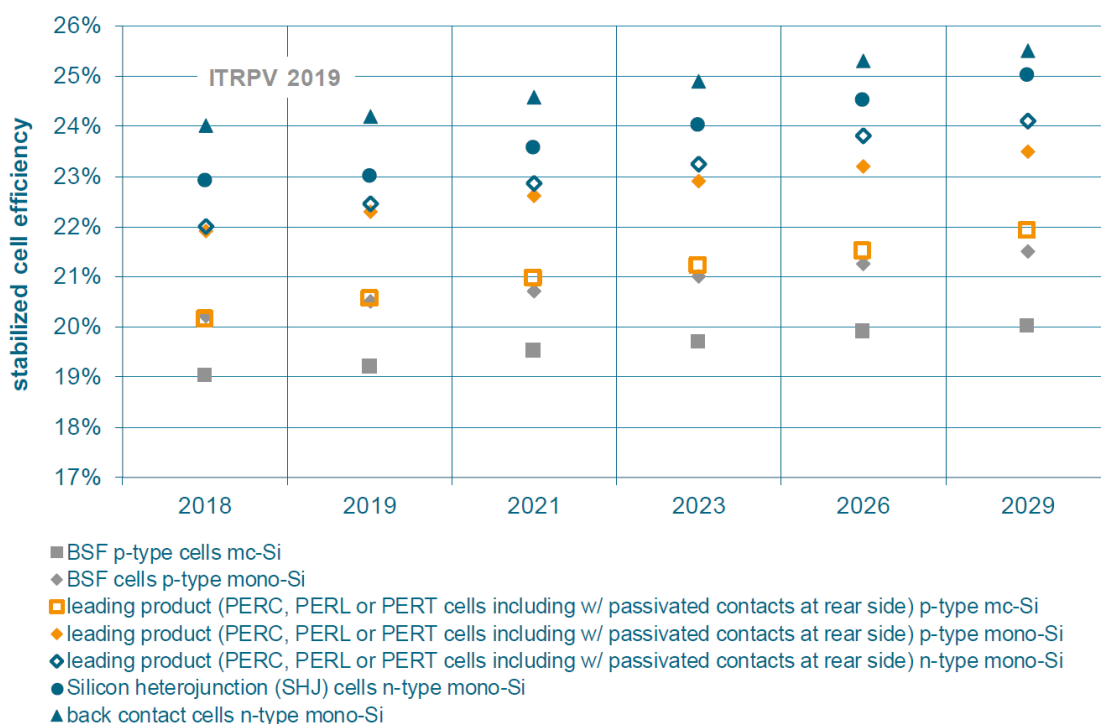
FIGURE 1.8. Average stabilized efficiency values for Si solar cells in mass production; (156.75 x 156.75 mm²) measured with busbars (no BB-less measurement) and front side STC. (*Data source*: ref[16])

1.4.2   Degradations in *p*-type *mono*-Si PERC solar cells

In addition to the solar cell performance, the *n*-type PERX solar cell concepts have better long-term stability. What is happening there in the *p*-type PERC solar cells? A schematic of a typical PERC solar cell cross-section with the so far three most severe degradation mechanisms which are shown in Fig. 1.9.
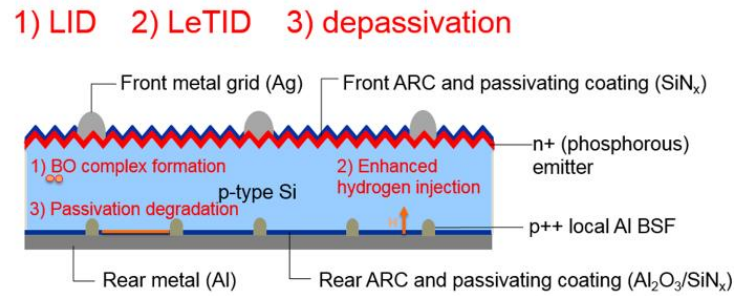
FIGURE 1.9. Three major degradation mechanisms in *p*-type PERC solar cell concept: 1) LID, 2) LeTID and 3) depassivation of rear dielectrics. (*Data source*: ref.[17])

1) LID

The very well-known and mostly understood degradation mechanism LID (light induced degradation) is based on the formation of boron and oxygen (BO) complexes[18]. The BO complexes are considered defects which depend on the square of the oxygen concentration and increases almost linearly with the boron concentration. LID occurs independently of light wavelength as shown by Hashigami et al. [19] and even during carrier injection in the dark, as demonstrated by Knobloch et al.[20] and Glunz et al.[21]. This implies that a more precise term for the effect would be carrier-induced degradation (CID), as light only contributes indirectly via carrier generation. Or, more precisely, the effect is termed to as the boron-oxygen defect lifetime degradation or short BO-degradation. A degradation of 3-5% relative conversion efficiency of solar cells fabricated on $1\,\Omega\cdot\text{cm}$ *p*-type Cz substrates during 12 h illumination with light. The degradation was found to be reversible by annealing at 200 °C in the dark for several minutes in the dark, the defect so being converted into what is referred to as the "annealed state." However, on subsequent exposure to light, degradation occurs again. This degradation cycle can be eliminated by annealing at elevated temperatures under illumination so forming what is referred to as the "stabilized state." Unfortunately, this "stabilized" state is also metastable and can be returned to the annealed state by dark annealing at ~200 °C for ~100 min. The cycles are illustrated in Fig. 1.10. It can be partly eliminated by a couple of methods which are described in Table 1.1. After the power returns to higher levels, there is no further LID effect. But it takes time to complete the process, and production capacities will be greatly influenced.

Manufacturers need to find a balanced way to treat the LID effect at an optimum level, i.e., in the most cost-effective way[22,23], otherwise, the cost will increase.
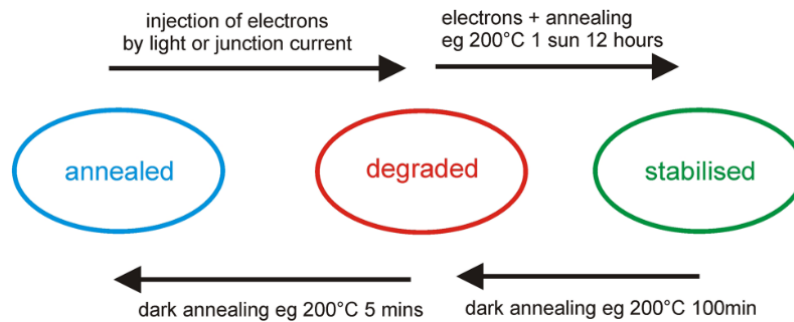
FIGURE 1.10. Block diagram of the BO LID-related defect states and processes. Overview of the ground and two metastable states of the BO-related defect using the nomenclature of ref.[24]. (*Data source*: ref.[25])

TABLE 1.1 Summary of PERC degradations and possible solutions. (*Data source*: ref.[17])

Degradation mechanism	LID	LeTID	Passivation degradation
Cause	BO complex formation	High [H]	Depassivation of dielectrics on undiffused surfaces
Reduction on cell level	· Low [O] Si wafer · High R_{bulk} Si wafer · regen. process · Ga-doping wafer · *n*-type devices	· w/ H-pure dielectric layers · Adapted process temp. kinetics · Lower firing temp. · Thin wafer	· w/ low doped BSFs · Upgrade to PERT

2) LeTID

The Light and elevated Temperature Induced Degradation (LeTID) was first found in *p*-type *mc*-Si PERC solar cells and also happens in *mono*-Si PERC[26]. This degradation is due to too much hydrogen content in the cell devices - which is also beautifully summarized with the bucket theory analogy of late Professor Stuart Wenham[26]. This is the case because the rear side passivation is in most cases realized by rather thick (compared to front side passivation) hydrogen-rich dielectrics. This additional hydrogen can penetrate into the Si bulk and lead to degradation. As for LeTID, the measures which can be taken to minimize are summarized in Table 1.1.

3) Passivation degradation on bare Si-wafer

It is very difficult to find out in cells/module, the real dominating cause of degradation. Recently, Herguth *et al.,* have discovered that the observed degradation in PERC solar cells is partly also based on the depassivation effect of the rear side dielectrics[27].

Much less degradation occurs in *n*-type devices; however, some scientists have claimed that LeTID can also impact *n*-PERT solar cells. Degradation test results conducted as part of this doctoral work will be shown in Section 5.3.4.

1.5 Why *n*-PERT-RJ solar cell

1.5.1 Process steps

After the discussion of the performance potential and the long-term stability between the *p*-type and *n*-type *mono*-Si solar cells, process step comparisons between the state-of-art mass-production type *p*-PERC and our *n*-PERT rear junction (RJ) solar cells will now be made. An industrial *n*-PERT-RJ solar cell concept will be introduced in this thesis, the process does not need laser selective front surface field (FSF), and so the front-side process is simpler than that for many PERC record cells. The efficiency potential in production is higher for *n*-PERT-RJ solar cell, as a result of the *n*-type wafers used as well as the totally diffused surfaces; moreover, these two factors guarantee not only high but also stable efficiencies, as explained in Table 1.1. For preventing LID and achieving higher solar cell efficiency, anti-LID regeneration and laser doping of selective emitter are needed for *p*-PERC solar cells. In our *n*-PERT-RJ solar cell process, the AlO_x passivation tool can be replaced by a highly productive low-pressure BBr_3 diffusion furnace, which provides diffusion of the rear emitter and in-situ SiO_2 passivation with good homogeneity[28]. When it comes to *n*-PERT solar cell technology, people always think it needs more process steps than *p*-PERC, but in fact, as shown in Table 1.2, there is no difference. This opens an upgrade solution for the existing cell manufacturing lines and the solar cell concept has strong compatibility with existing equipment, thereby giving the equipment a longer service life. For the traditional *mc*-BSF cell manufacturing lines it is only required to add two more process tools: ablation laser and boron diffusion

furnace; for the *p*-type *mono*-PERC manufacturing lines, only an additional boron diffusion furnace is required. The *n*-PERT-RJ solar cell concept plays a bridging role not only on the material switching from *p*-type to *n*-type, but also assists migrating from the traditional *mc*-BSF to the future advanced solar cell concepts (e.g., IBC or tandem). This is why the *n*-PERT-RJ solar cell concept is investigated in this thesis.

TABLE 1.2. Mass production process flow comparison between *p*-PERC and *n*-PERT-RJ solar cells. (AOI means automated optical inspection)

p-PERC (mass production)	*n*-PERT-RJ (ISC-Konstanz)
Clean/Texturing	Clean/SDE
Front POCl$_3$	Rear BBr$_3$
Laser SE doping	BSG etching
Rear etching	Rear SiN$_x$
Annealing	Texturing
Rear AlO$_x$/SiN$_x$	POCl$_3$ diffusion
Front SiN$_x$	PSG etching
Laser opening	Front SiN$_x$
Printing/Co-firing	Laser ablation
AOI	Printing/Co-firing
LID regeneration	AOI
Sorter	Sorter

1.5.2 Bifaciality and LCOE

Some will argue that the wafer price of the *n*-type is still higher than *p*-type, which makes the higher cost on the *n*-PERT-RJ solar cell. However, the higher cost of the *n*-PERT-RJ module in a system environment is already offset by the advantages of higher efficiency, better stability, and slightly higher bifaciality[29]. Bifaciality is defined as the ratio between front and rear solar cell efficiency or module output power[30]. The value of the bifacility will be affected by the following factors: (1) different bifacial solar cels (modules), for example, *p*-PERC+ >70%, *n*-PERT-RJ >80%, Heterojunction (HJT) >95%, higher bifaciality generates higher energy yield; (2) location of site, content of diffuse radiation and direct radiation; (3) tilt angle, the increasing tilt angle will cause increased reflected light and hence contributes to energy yield; (4) albedo factor, reflectivity of horizontal surface and (5) row to row distance, if inter-row space is increased reflected light will increase on the rear side and hence contributes

to energy yield. The research on bifacial PV systems dates back as early as the 1960s. The first functioning prototype was designed by the Japanese researcher H. Mori in 1966[31], and the first bifacial PV system was a part of the Russian Space Program in the 1970s[32]. The reason for it becoming more implemented in our society today is due to the rapid expansion of the solar cell market. The globally growing demand has lowered the prices on PV technology and enabled the bifacial technology to grow. Because the additional bifacial gain will lower the levelized cost of electricity (LCOE) further. The bifacial gain means $(Y_B-Y_M)/Y_M$ where Y_B and Y_M are the electricity yields in kWh for bifacial and monofacial solar modules, respectively. With larger commercial systems, realistic bifacial gains are expected in a range from 5% to 15%[16]. The expected market trend for bifacial cells is shown in Fig. 1.11. The 2019 market share of about 13% is expected to increase significantly to more than 60% within the next 10 years.
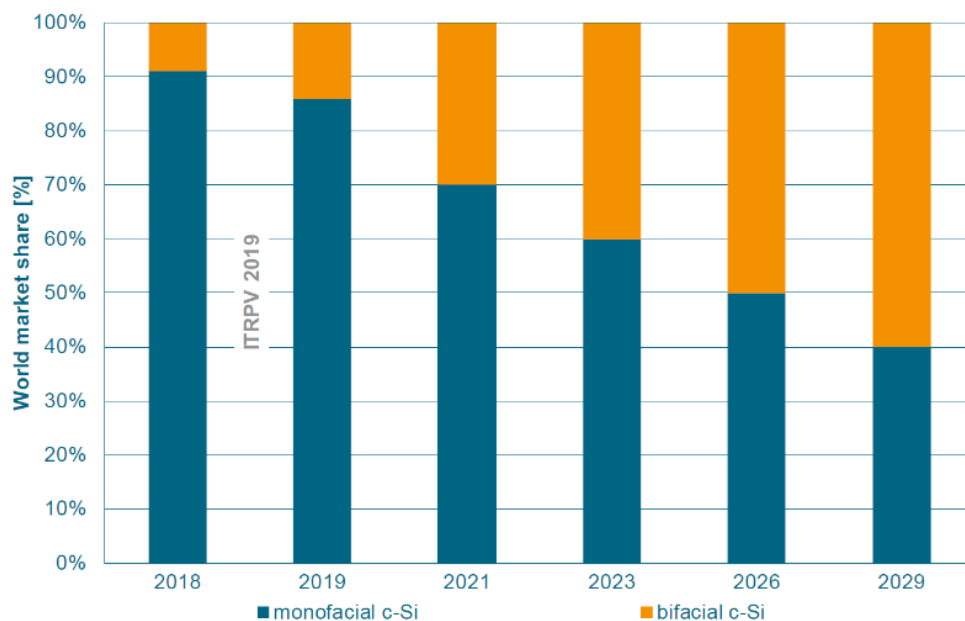
FIGURE 1.11. Worldwide market shares for bifacial cell technology. (*Data source:* ref[16])

Since the PV cumulative power generation capacity has increased greatly in the last ten years, for example in the European Union, the PV cumulative power generation had been exceeding 100 GW (Fig. 1.12), new calculation models for evaluating cost-effectiveness and comparability must be considered. The "**cost of ownership**" (COO, which is normally used on the solar cell level) and **"Cost/Wp"** are no longer sufficient as indicators to evaluate the
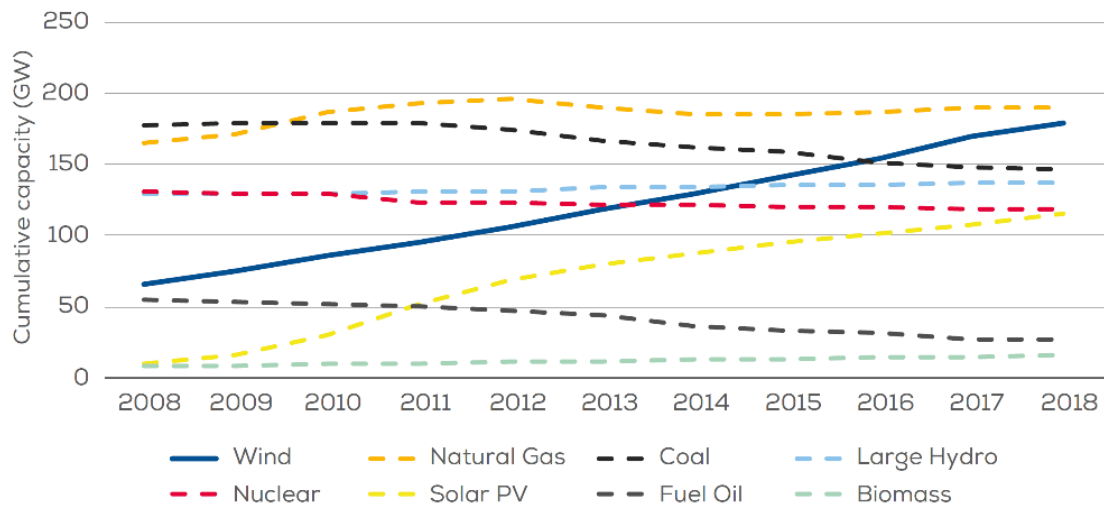
FIGURE 1.12. Total power generation capacity in the European Union 2008-2018. (*Data source:* ref.[35])

development of PV technologies, and are not suitable to compare the cost of the electricity to the other renewable (e.g., wind, biomass, hydro) or traditional energy technology (e.g., coal, fuel oil, natural gas). Based on ref. [33], in the beginning (before 1998), the module costs dominated. Hence, the use of "**module prices/Wp**" under standard test conditions (STC), even till today, this is still used very often to compare the cost between modules. The first grid-connected installations had an output of 1–3kWp then were followed by the installation sizes between 3–100kWp. During this period (before 2000), the non-module costs, so-called balance of system (BOS) costs, were added to the module costs. In this way, a comparative value was obtained, namely the "**system costs/Wp**". In the following period (before 2005), the installation sizes grew into the MW range, and the performance ratio (PR) was introduced. The PR means kWh/kWp which enabled a comparison of different PV installations.

The launch of the feed-in tariff (FiT) in Germany induced the construction of large-scale power plants in the MWp range which called not only for solutions to the technical challenges but also for new financing models. The "**cost/kWh**" and the target of grid parity was first to be mentioned in that time (after 2005). With the continuing expansion of PV electricity generation, its efficiency then began to be compared to other energy sources in the energy mix. The **"levelized cost of electricity (LCOE)"** method was introduced in the PV industry in around 2010, and the detailed LCOE calculation is shown in ref. [34]. LCOE enables different energy sources to be compared to each other in a standardized

way and to assess their cost-effectiveness. The target for PV development is to reduce the LCOE value lower than the grid parity at residential prices.

1.6   Thesis outline

This thesis is divided into 7 chapters. The introductory chapter is followed by **Chapter 2.** In this chapter, the large-area n-type Passivated Emitter and Rear Totally diffused Rear Junction (n-PERT-RJ) solar cell structure with a dot-shaped laser contact opening (LCO) pattern on the rear side is presented. The screen-printed solar cell devices are investigated for fully rear side aluminium (Al) paste metallization with various silicon additives (Si-add) content. An hypothesis regarding the screen printed point contact formation and the role that the Si-add played in the alloying process is proposed, based on the analysis of microstructure and electrical properties of the solar cells. Adapted process conditions led to an n-PERT-RJ solar cell with 21.78% efficiency and 686 mV open-circuit voltage (V_{OC}). The process fits simple industrial implementation and has the potential to exceed the 22% efficiency level in mass production.

Chapter 3 is the application and extension of **Chapter 2**. In this chapter, the development history of point contacts will first be introduced, and will then be followed by the understanding on the impacts of the Si-add on the performance our n-PERT-RJ solar cells. Detailed loss analysis of the V_{OC}, short-circuit current density (J_{SC}) and fill factor (FF) are performed separately. The relationships between point contact characteristic, amount of Si-add and pitch of LCO are also investigated. An innovative "point-line" contact concept on the rear side is introduced, which is composed of point LCO and Al metal finger design resulting in an n-PERT-RJ solar cell that reaches V_{OC} of 692 mV and peak efficiency of 22%. The 60% bifaciality of the device opens the way for an additional power output on module level which provides further reductions in the levelized cost of electricity (LCOE). These bring the rear-side point contact design more flexibility to be applied in industrial mass production.

Chapter 4 first introduces the developing history of the n-PERT-RJ solar cell, then presents the optimization of a large area n-PERT-RJ solar cell to reach V_{OC} exceeding 690 mV and 22% stable solar cell efficiencies by using industrial diffusions and screen-printed metallization on both sides. Solar cells with high voltages have lower temperature coefficients and therefore higher energy yield

in PV systems, particularly for those exposed to high temperatures (e.g., in desert regions). With a free energy loss analysis and Quokka3 simulations, the recombination and resistive loss mechanisms in the n-PERT-RJ solar cells are identified and a guideline for future development is given, showing a practical roadmap toward 700 mV V_{OC} and solar cell efficiencies approaching 23%. Stable high voltages in solar cells can be transferred directly to modules with no losses and are becoming increasingly important.

Chapter 5 is a continuation of **Chapter 4.** In this chapter, a dash pattern for the firing through silver (Ag) contact is applied instead of performing the selective doping on the front surface field (FSF) of the n-PERT-RJ solar cell concept, and this effectively reduces the area-weighted metal-induced recombination current $J_{0, \text{Met (Ag)}}$. The impact of different n-bulk properties on the n-PERT-RJ solar cell performance is revealed by Quokka3 simulation. This industrial type n-PERT-RJ solar cell demonstrates the same performance level as the advanced passivating contact solar cell concepts, has a cost of ownership (COO) close to the p-PERC solar cells, and last but not least, shows performance stability after light and elevated temperature induced degradation (LeTID) tests.

Chapter 6 presents the mechanism of the non-destructive dot-shaped LCO, the introduction of an innovative evaporation type Al-PVD system and a series of detailed comparisons between the PVD- and screen printed (SP)-Al point contact (from contact properties to solar cell performance). Embedding Al point contacts on the rear side of the n-PERT-RJ solar cell can effectively reduce the contact area fraction and successfully limit the metallization induced recombination current ($J_{0, \text{Met}}$) impacting on the performance of V_{OC}. The previous chapters demonstrate that the Al contacts on the dot-shaped LCO can also be formed by screen printing with Al pastes, hence physical vapor deposition (PVD) is no longer the only solution. In addition to $J_{0, \text{Met}}$, the specific contact resistivity (ρ_c) is another criterion for the Al contact performance. The biggest challenge for the PVD-Al point contact application on the rear of the solar cells with SP-Ag front contact is to prevent a higher ρ_c due to the growth of the oxide layer at the Al/LCO-Si interface. The Quokka3 simulation with varying ρ_c is also performed for fitting the ρ_c of the point contact and revealing

the potential efficiency and challenges of n-PERT-RJ solar cells with PVD-Al rear point contact.

Lastly, **Chapter 7** will summarise the findings of the thesis and provide an outlook for future work.

Chapter 2: Screen-printed point contact formation by using Al pastes containing Si sdditives

2.1 Introduction

N-type Cz silicon solar cell concepts offer two main advantages compared to *p*-type: first, they are free of light-induced degradation (LID)[18,36] and second, less sensitive to metal impurities[37]. The investigation in this chapter will focus on the *n*-type Passivated Emitter and Rear Totally diffused Rear Junction (*n*-PERT-RJ) solar cell structure, and the detail of this solar cell concept will be discussed in Section 4.1. The point contact design was proposed nearly 20 years ago[38] with the aim to reduce the proportion of the contact area since the carrier recombination is strongly increased in the contact region. The development of the point contact design concepts will be discussed in Section 3.1. However, most of the design concepts are not simply compatible with the general screen printing process. In this chapter, the difficulties that occur for screen-printed point contacts with the Al pastes and how Si-add in Al paste affects the contact formation will be discussed. Finally, the electrical properties of the processed *n*-PERT-RJ solar cells are shown, illustrating the potential of cell efficiency approaching 22% and the option for an easily feasible industrial solar cell process.

2.2 Experimental

2.2.1 Precursors of the *n*-PERT-RJ solar cell

Fig. 2.1 illustrates the process flow of our *n*-PERT-RJ solar cells. The M2-sized (area: 244.32 cm²) *n*-type *Cz*-Si wafers (orientation <100>) with 180 µm thickness and 4 $\Omega \cdot$ cm base resistivity were used for substrates. After saw damage removal in sodium hydroxide (NaOH), a "Piranha clean" consisting of sulfuric acid and hydrogen peroxide (H_2SO_4/H_2O_2) was performed. The process then underwent a boron diffusion in a quartz tube furnace using boron tribromide (BBr_3) as a precursor gas, the drive-in phase at a temperature plateau with a peak temperature of 1000 °C under oxygen (O_2) atmosphere. This boron emitter was in-situ passivated by silicon dioxide (SiO_2) layer during the drive-in step. After proper selectively BSG etching in dilute HF and a rear capping layer deposition, the subsequent front side texture in potassium

hydroxide (KOH) was followed by a phosphorus diffusion using phosphorus oxychloride (POCl₃) with a 960 °C drive-in temperature under O₂ atmosphere in a tube furnace. A lightly doped homogeneous FSF was formed and well passivated by an in-situ grown SiO_2 layer. After PSG removal in dilute HF, the precursors were finished by the deposition of a silicon nitride (SiN_x) layer with plasma-enhanced chemical vapor deposition (PECVD) technique after the phosphosilicate glass (PSG) removal.
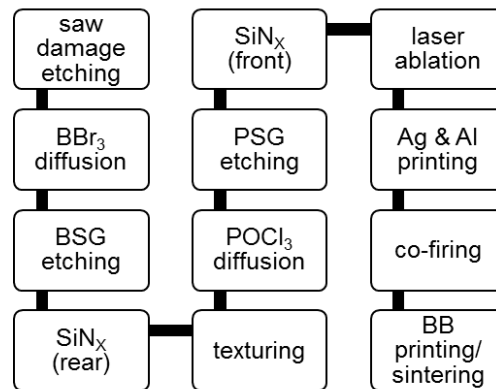
FIGURE 2.1. Process flow of the *n*-PERT-RJ solar cells.

2.2.2 The laser contact opening

At the rear boron side, a pulsed green laser was used to perform the dot-shaped LCO with a 40 µm spot diameter and a 450 µm pitch on the rear passivation stack (Fig. 2.2).
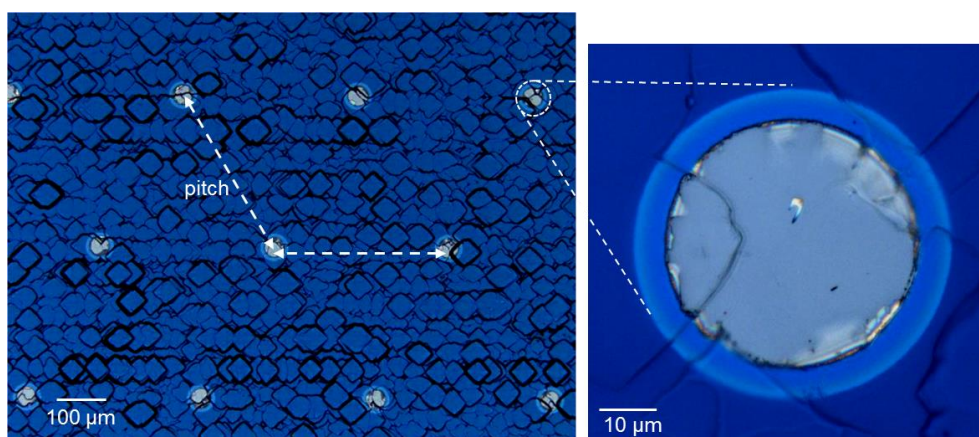
FIGURE 2.2. The top view images of the dot-shaped laser contact opening (LCO) in a hexagonal pattern and 450 µm pitch taken by laser scanning microscopy (LSM).

2.2.3 The metallizations

Afterwards, a fully covered Al electrode on the rear and Ag fingers on the front was printed that is co-fired in a fast-firing belt furnace for sintering and

alloying of the metal contacts. Figure 2.3 shows the *n*-PERT-RJ solar cell structure investigated in this thesis. The rear sides of the solar cells were metallized with four different Al pastes which are: (a) without Si-add; (b) with low wt% Si-add; (c) with mid wt% Si-add and (d) with high wt% Si-add. "Low" wt% means that the proportion of Si-add in Al paste is a hypoeutectic composition (<12.2 wt%) while "mid" and "high" wt% means that the proportion of Si-add in Al paste is a hypereutectic composition (>12.2 wt%). The amount of Si-add ranges from 0-20 wt%.
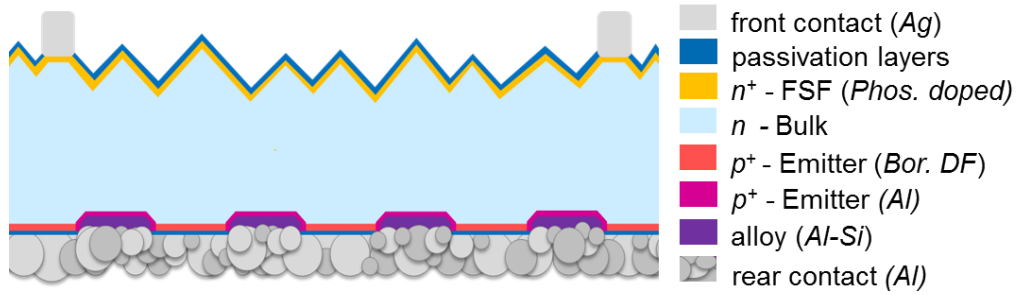
FIGURE 2.3. Schematic of an *n*-PERT-RJ solar cell.

2.2.4   Al mtallization induced recombination current density extraction

Symmetrically diffused and passivated *n*-type test structures were created in parallel to estimate the FSF quality and emitter recombination current densities ($J_{0, \text{FSF}}$ and $J_{0, \text{Emitter}}$) by Quasi-Steady-State Photoconductance (QSSPC) lifetime tester (Sinton Instruments WCT-120)[39]. The symmetric boron diffused test structures then underwent single side laser opening and contact alloying. After Al metal removal and QSSPC measurement, the dependence of the Al point contact recombination current density $J_{0, \text{Met (Al)}}$ on the Al contact fraction (f_{m}) was extracted by

$$J_{0, \text{Met (Al)}} = [J_{0, \text{Total}} - J_{0, \text{Emitter}} (2 - f_{\text{m}})] \,/\, f_{\text{m}} \qquad (2.1)$$

2.3   Results and discussion

2.3.1   Point contact formation

2.3.1.1   *Heating up procedure*

By raising the temperature to the Al melting point, T*melt* (660°C), the liquid state Al in the printed paste matrix is able to locally penetrate the native oxide shell of the Al metal particles[40] (Fig. 2.4) and to get in contact with the Si surface at the LCO. For the pastes with Si-add the above reaction happens earlier

because the decreasing melting point (T_{eut} (577°C)). Si dissolves into the molten Al and the alloying process starts to take shape. According to the Al-Si binary phase diagram[41], the alloy at T_{eut} and T_{melt} has the capacity to absorb the specific weight percent silicon (wt%-Si), f_{eut} (12.2 wt%-Si) and f_{melt} (17.5 wt%-Si), respectively, if the system is in equilibrium. As a result of the locally restricted feasibility of Si, a silicon concentration ([Si]) gradient exists and starts to balance during the alloying process. Si will start to migrate from the contact area into the above molten Al paste matrix. The bulk-Si will "diffuse" out via the alloy region into the Al paste matrix above the dot-shaped LCO. During the time period II (Fig. 2.5(a)), the temperature increases from T_{melt} to T_D and will raise the wt%-Si that can be absorbed in the alloy from f_{melt} to f_D (Fig. 2.5(b)). More Si from bulk will dissolve into the alloy to achieve the temperature specific composition. A higher [Si] gradient between the alloy region and paste matrix stimulates a stronger Si out-diffusion.
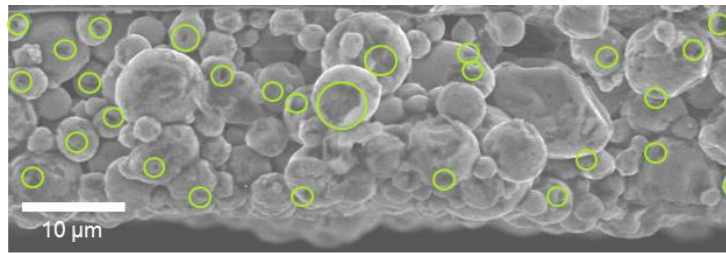
FIGURE 2.4 The scanning electron microscopy (SEM) images of the screen-printed Al paste matrix after the firing process, the green circles point out the local penetration on the native oxide shell of the Al metal particles.
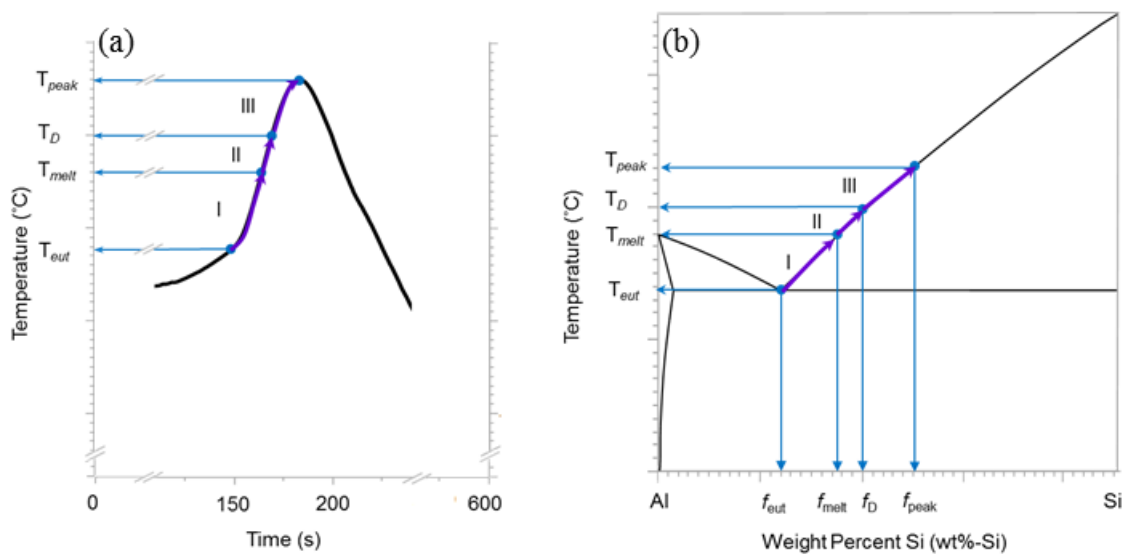
FIGURE 2.5. The heating up procedure: (a) The partial sintering profile of the fast-firing furnace: T_{melt} is the Al melting temperature, T_D is a specific temperature higher than T_{melt} and lower than T_{peak} (peak temperature of the sintering profile). (b) The partial Al-Si binary phase diagram: f_{melt} is a specific weight percent Si (wt%-Si) in alloy at T_{melt}, f_D and f_{peak} are the Si fraction at T_D and T_{peak} respectively.

For this reason, the Si transportation during heating up is consisting of two parts: (1) the bulk Si dissolution into molten Al (a temperature-dependent behavior); (2) the Si diffusion out of the alloy region into the paste matrix (a [Si] gradient dependent behavior). For an assumed thermodynamic equilibrium at a specific temperature, this means that a more intense Si diffusion out of the contact area into the paste matrix will amplify the liquidation of Si from bulk into the molten Al for attaining the specific alloy composition. Solar cells printed with the Al paste without any Si-add (paste A) have a stronger Si transportation than other groups with Si-add. The dissolution is getting lower for increased Si additives in the Al paste. Si additives effectively suppress the bulk Si transportation out of the LCO. Below T_D the temperature dependence wt%-Si in the alloy exceeds f_D. Solar cells fabricated with paste D will not see a boosting gradient between the alloy region and paste matrix. The maximum [Si] gradient effect is achieved for all groups when reaching the peak temperature (T_{peak}) of the process.

2.3.1.2 Cooling down procedure

After overcoming peak temperature (T_{peak}), the process turns into cooling down procedure (Fig. 2.6(a)). Si dissolution from the substrate, however, will continue during this period, if there is still a demand in the total paste volume to absorb Si in order to balance the system. The liquid phase will attract bulk Si as long as the temperature-dependent maximum solubility for Si is reached. Just after the temperature drops below the actual saturation point in Al/Si solution, the dissolution process stops and epitaxial growth of Al-doped Si at the interface between Si substrate and liquid phase can take place. The recrystallization of Si in the contact region continues until the eutectic temperature T_{eut} (Fig. 2.6(b)) is reached and the liquid phase solidifies completely. The higher the initial concentration of Si is in the paste, the earlier recrystallization will happen and the more time for epitaxial growth from the liquid phase is given before solidification of the system.
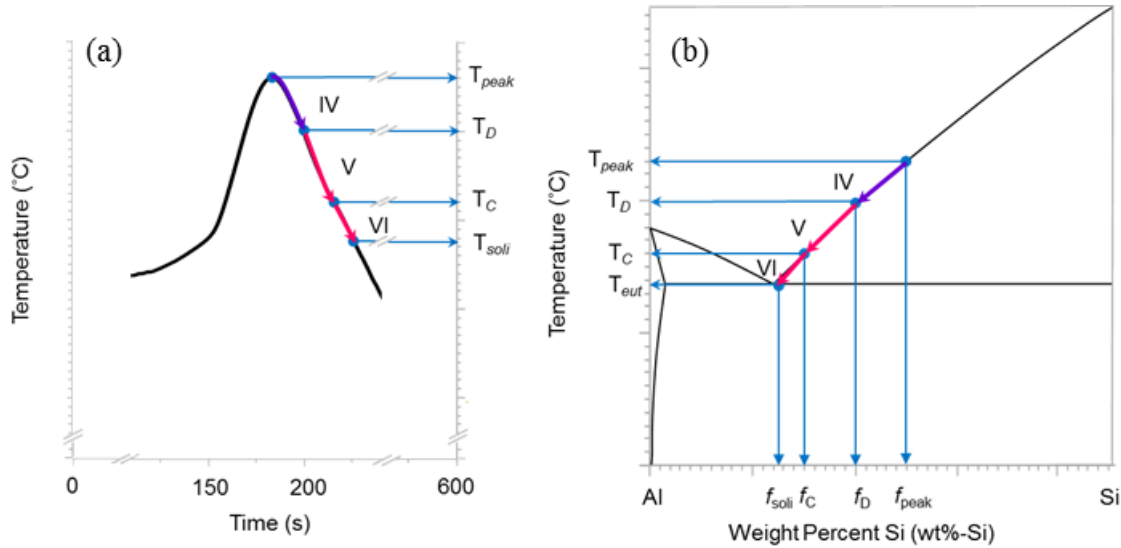
FIGURE 2.6. The cooling down procedure: (a) The partial sintering profile of the fast-firing furnace: T_{peak} and T_D are specific temperatures as the same mentioned in Fig. 1(a), T_C is a specific temperature lower than T_D and higher than T_{soli} (solidification temperature of Al-Si system,557°C) (b) The partial Al-Si binary phase diagram: f_{peak} and f_D are as the same wt%-Si mentioned in Fig. 2(b), f_C and f_{soli} are the wt%-Si in alloy at T_C and T_{soli} respectively.

Combining the sintering profile and the Al-Si binary phase diagram during the whole alloying process, the relevant effects of Si transportation that define the contact region can be divided into two categories: (1) bulk-Si out-diffusion via alloy and (2) excess alloy-Si repellence and recrystallization at Si/alloy interface before solidification of the whole paste system. The former will affect the Al contact size and the later will govern the thickness of the epitaxial grown Al-doped Si. Table 2.1 is the short summary of the behavior during the whole alloying process: it is shown that increasing the ratio of Si-additives in the Al paste, minimizes the [Si] gradient and therefore suppresses the bulk-Si dissolution effectively. From no to high wt% Si-add in the Al paste, the Si out-diffusion time ratio (%) is reduced by nearly half if an infinite metal matrix reservoir related to the alloying time is assumed. On the other hand, the increased addition of Si to the Al paste also helps to start the recrystallization process earlier. The time for epitaxial growth of Si for devices fabricated with paste D was the longest compared to all other groups.

TABLE 2.1. The dominated [Si] transportation during each period of the sintering process. The four groups' solar cells rear side are fully printed with different amounts of Si-add Al paste. *The time is calculated by each period time divided the total alloying time (The sum from I to VI is about 80 seconds).

Period	*Time (%)	Al paste A: no Si-add	Al paste B: low wt% Si-add	Al paste C: mid wt% Si-add	Al paste D: high wt% Si-add
I $(T_{eut} \rightarrow T_{melt})$	22	-	out-diffusion	- / out-diffusion	-
II $(T_{melt} \rightarrow T_D)$	6	out-diffusion	out-diffusion	out-diffusion	-
III $(T_D \rightarrow T_{peak})$	14	out-diffusion	out-diffusion	out-diffusion	out-diffusion
IV $(T_{peak} \rightarrow T_D)$	25	out-diffusion	out-diffusion	out-diffusion	out-diffusion / recrystallization
V $(T_D \rightarrow T_C)$	20	out-diffusion	out-diffusion	out-diffusion / recrystallization	recrystallization
VI $(T_C \rightarrow T_{soli})$	13	out-diffusion	out-diffusion / recrystallization	recrystallization	recrystallization

2.3.2 Analysis of microstructure and electrical properties

In this section, the analysis of microstructure and electrical properties supporting the above-proposed hypothesis of the thermodynamic interaction between bulk Si and Al paste will be demonstrated. Fig. 2.7 depicts microscopic images that were taken by laser scanning microscopy (LSM), which are shown the rear side top view of solar cells printed with different Al pastes. The images were taken after the alloying process and subsequent removal of the metal matrix and alloy by hydrochloric acid (HCl). Each black spot represents a point contact. It can be seen that the paste composition clearly defines the spot size of the contacts. After increasing the amount of Si-add in the Al paste, the contact shape changes from diamond to circle shape, the average contact width decreases from 125 μm to 55 μm (Table 2.2). As a consequence, the unpassivated area ratio decreases from 5.9 to 1.3%. This is done by the management of extent and the period length of the Si out-diffusion. The result matches the proposed hypothesis; as the solar cells printed with high wt% Si-add Al paste should have a shorter and less intense out-diffusion period. For the further in-depth investigation, the scanning electron microscopy (SEM) is applied to observe the

cross-sectional microstructure (Fig. 2.8). The side view of the contact reveals significant differences not only on the cross-sectional shape but also on the depth. The cross-sectional geometric shape turns from a triangle via a trapezoidal to a semicircular shape. In a three dimensional display, the surface is changed from a pyramid via frustum to hemisphere. The effect is accredited to the fact that bulk Si dissolves into the alloy preferentially along the Si (111) planes[42]. The more bulk Si is detached from the substrate to the alloy the more explicit the (111) planes are formed and finally a pyramid shape is visible.
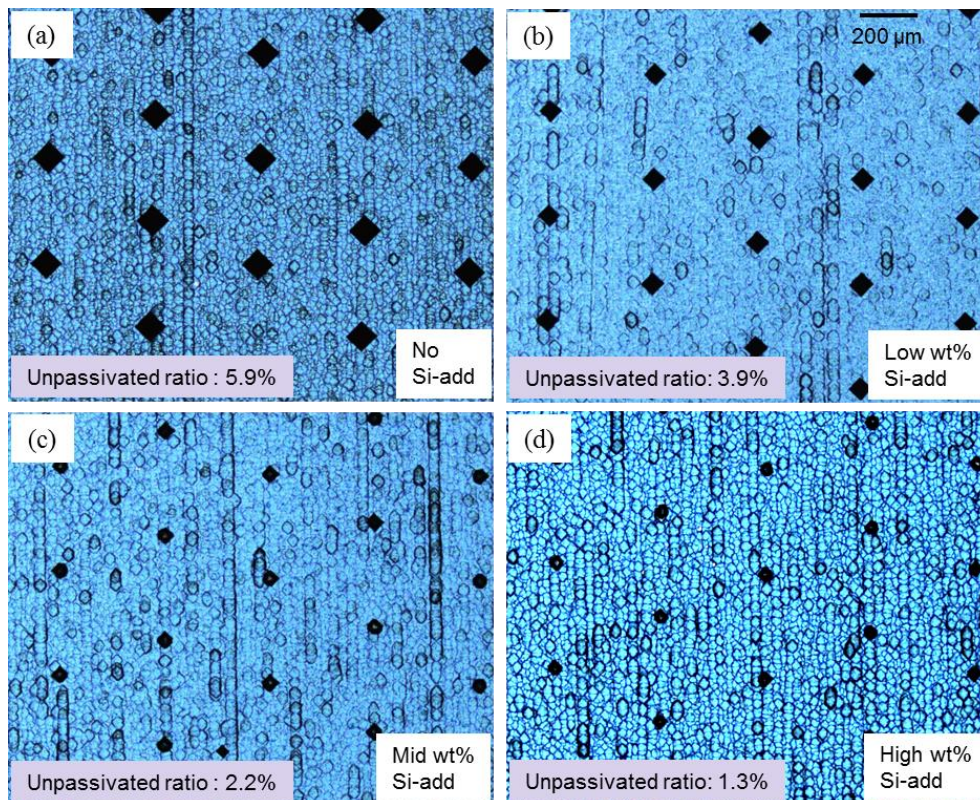
FIGURE 2.7. Top view images were taken by laser scanning microscopy (LSM): fully screen printed with (a) no, (b) low wt%, (c) mid wt% and (d) high wt% Si additives Al paste. The metal matrix and alloy part are removed by HCl.

TABLE 2.2 The Contact depth/width, unpassivated area and saturation current density for different amounts of Si additives Al paste.

Si-additives (wt%)	no	low	mid	high
Contact Width (µm)	125	98	81	55
Contact Depth (µm)	46	38	21	12
Unpassivated Area (%)	5.9	3.9	2.2	1.3
$J_{0, \text{Met (Al)}}$ (fA/cm^2)	2839	1100	773	635
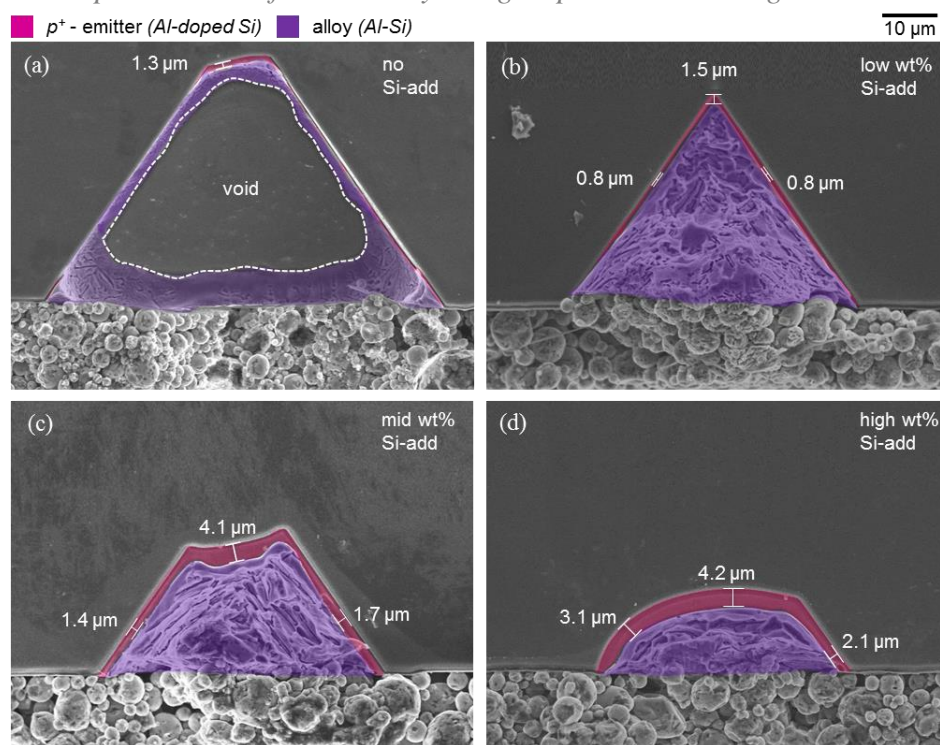
FIGURE 2.8. The cross-sectional microstructure images were taken by scanning electron microscopy (SEM): fully screen printed with (a) no, (b) low wt%, (c) mid wt% and (d) high wt% Si additives Al paste.

Apart from the appearance also the depth of the imprints changes and is decreased from 46 to 12 μm (Table 2.2). In addition to the above-described observations, the interface between the Al-doped p^+ region and the n-type bulk is clearly visible in SEM cross-sectional images. In Fig. 2.8, the pink color represents the Al-doped p^+ region. The elevation of Si-add in the Al paste stimulates the formation of a thicker and more uniform Al-doped p^+ region (Fig. 2.8(d)) is found. The thicker Al-doped p^+ region is in accordance with the hypothesis of longer recrystallization time for the groups printed with a higher amount of Si-add in the Al paste. A thicker Al-doped p^+ region below the contact results in better shielding[43] of the semiconductor from the recombination active metal contact. This can be translated to the value of contact saturation current, $J_{0, \text{Met (Al)}}$, which decreased from 2839 fA/cm^2 for samples fabricated with paste A to 635 fA/cm^2 for those who were manufactured with paste D (Table 2.2). Our microstructural observations support our proposed model for the Al-Si interaction for dot-shaped LCO during heating and cooling. The hypothesis offers an explanation of the role of Si-add in the Al paste, and why a proper amount of Si-add in the Al paste significantly improves the point contact quality.

2.3.3   Solar cell performance

Based on the analytic results, the *n*-PERT-RJ solar cells with rear dot-shaped LCO and fully covered rear metallization with the above introduced four Al pastes are fabricated. Table 2.3 shows the electrical performance, and illustrates two main results: (1) The V_{OC} shows a huge improvement (~120 mV higher) when adding Si-add to the paste. With increasing Si-add content in the paste, the parameter can be still improved up to the highest averaged V_{OC} of 682 mV. The effect is attributed to a reduced contact area (only 1.3%) and a proper formed Al-doped region. (2) The FF increases from around 64.5 to 80.6%. The reason for this observation as being due to an improved contact quality and the prevention of void formation (Fig. 2.8(a)) has been revealed. In an additional experiment, the doping profile of the front surface field (FSF) of our samples is modified to a shallower junction depth and lower surface concentration. This new group was metallized with the high Si-add Al paste D and the same rear LCO design. The current increased by 0.3 mA/cm² due to less free carrier absorption[44], and the V_{OC} improved by 4 mV due to the lower surface recombination. But in the end, these benefits are trading off with a lower FF caused by a But in the end, these benefits are trading off with a lower FF caused by a higher FSF sheet resistance. The champion efficiency in this chapter is at 21.78% (Table 2.4) which is certified by Fraunhofer ISE CalLab (Appendix I).

TABLE 2.3. Averaged I-V data of *n*-PERT-RJ solar cells. The rear sides are metallized with Al pastes containing varying amounts of Si-add.

Silicon additives (wt%)	J_{SC} (mA/cm²)	V_{OC} (mV)	FF (%)	Eta (%)	pFF (%)
no	39.0	560	64.5	14.08	80.3
low	39.3	675	80.4	21.36	84.2
mid	39.3	680	80.7	21.59	84.4
high	39.3	682	80.6	21.61	84.7

(5BB grid design, in-house measurement using an ISE CalLab calibrated reference cell)

TABLE 2.4. I-V data of screen-printed point contact *n*-PERT-RJ solar cells with different FSF doping profiles.

FSF doping profile		J_{SC} (mA/cm²)	V_{OC} (mV)	FF (%)	Eta (%)
BKM	*Averaged*	39.3	682	80.6	21.61
	Champion	39.3	682	80.8	21.66
Shallow	*Averaged*	39.6	686	79.8	21.64
	*Champion**	39.5	686	80.4	21.78

*Certified by Fraunhofer ISE CalLab (Appendix I).

2.4 Conclusion

In this chapter, the Si transportation phenomenon for a point contact architecture with fully covered Al paste metallization during the Al alloying process was investigated. It was found that the mechanism can be deeply affected by the addition of Si additives in the Al paste. Uniform distributed Si-add in the Al paste reduce the [Si] gradient between the contact region and the Al paste matrix was found, successfully suppressing the out-diffusion of bulk-Si. Cutting down the dissolution period in turn leads to a smaller contact area. In other words, keeping more PECVD passivated area with a low recombination current. A proper [Si] gradient management enables recrystallization at an earlier stage during the cooling procedure. Longer recrystallization time is helpful to increase the thickness of the eutectic grown Al-doped p^+ region. A thicker p^+ layer in the recombination active contact region causes a better electrical shielding[43] and lower $J_{0, \text{Met (Al)}}$. The proposed Si transportation model is supported by the analysis of cross-sectional microstructures and electrical properties measured on solar cell devices. With the help of high Si additives in the Al paste (a hypereutectic composition) and metallization on dot-shaped LCO, it is possible to reduce the rear side opening after annealing to only 1.3% of the total area and the recombination current to only 635 fA/cm^2 $J_{0, \text{met (Al)}}$, which is similar to the reported results given in the literature[45]. The Al paste with Si-add has been demonstrated, making screen printed point contacts feasible and opening up the easy transfer to industrial printing lines. The latest optimized fully screen printed 6-inch *n*-PERT-RJ solar cell featured a *V*oc up to 686 mV, efficiency up to 21.8% and opens the potential to devices with a level higher than 22%.

Chapter 3: Investigation on industrial screen-printed aluminum point contact and its application in *n*-PERT-RJ solar cells

3.1 Introduction

The rear-side point contact design was proposed over 30 years ago[46–48] with the aim of reducing the rear metal contact fraction because of the high carrier recombination within this region. Many techniques have been applied to pattern the dot-shaped point contact openings on the rear side dielectric films. For example, photolithography[49–51] was widely used in the earlier stage, which performed accurately for patterning, but was too expensive for an industrial process. As a result, it then was substituted by applying etching paste[52,53] and laser ablation[54–60]. Etching pastes are low cost and provide nearly no additional damage within the patterning regions. The printable feature makes it easy to implement the dot-shaped pattern, but additional post-printing curing and cleaning steps increase the complexity of the manufacturing process. The "contact-less" and "mask-less" laser ablation technique became increasingly attractive. As accuracy enhances, throughput improves, and costs reduce, thus, laser ablation is now the mainstream in the photovoltaics (PV) market for the structuring of dielectric films. Laser ablation can be performed before or after the rear-side metallization. The first option is called laser contact opening (LCO), where the rear dielectric films are ablated by laser, and in the past was mostly followed by the "soft" metallization techniques (i.e., PVD[61–63] or plating[64]). However, the contact resistance of these "soft" metallizations is subject to the presence of the oxide layer in between the Si and metal above it. This oxide layer is induced by the high thermal budget process[65], laser ablation[66] or is simply caused by the exposure of the LCO to the air before metallization. Therefore, additional cleaning between the two processing steps is required. The absence of a heavier doped region under the "soft" metalized point contact results in poor shielding[43] of the metal-silicon contact and as a consequence causes a higher recombination current density ($J_{0, \text{Met}}$)[67]. A second strategy for the dot-shaped openings is called the laser-fired contact (LFC)[68] which was developed by Fraunhofer Institute for Solar Energy Systems (FhG-ISE). Compared with the LCO solar cells, the metallization step of LFC solar cells is done prior to the

laser process. More specifically, the dot-shaped patterning and metal contact formation are achieved simultaneously by one laser step. The LFC once was considered as a promising way to form the local rear contact and successfully attracted industrial companies to build up pilot lines[69,70]. As in-situ Al-Si alloying and contact formation prevents the growth of the native oxide; the local Al-doped regions provide a better shielding[43], the compatible rear-side metallization techniques are various (e.g., PVD, screen printing and an approach based on aluminum foil[71]), and the LFC process is easier to be integrated with existing industrial screen-printing lines. However, the LFC concept is sensitive to several processing parameters such as laser power and pulse shots, rear contact pitch, and bulk carrier lifetime[71–73]; moreover, the laser-induced damaged area in the bulk[74] and the contact craters[75,76] make LFC more challenging for mass production. The insufficient Al-doped p^+ region formation of the ultra-short LFC process is another issue[77]. The thickness of the Al-doped p^+ region should be at least 3 µm to significantly reduce the contact recombination current density[78].

Due to detailed investigations by the academic researchers (e.g., Lauermann et al., who revealed the difficulties when applying screen-printed Al point contact[79], or Müller et al., who presented that the screen-printed Al contact recombination velocities of line contact are several orders of magnitude lower than the point contact[80] and published the first analytical model[81] for calculating the Al-doped p^+ Si thickness correlating to the LCO geometries and thus explained well the findings above) coupled with the optimization of the Al paste from the manufacturers (especially solving the problem of voids for LCO), as well as strong input from the industrial users, the line-shaped LCO with screen-printing Al paste[82,83] eventually dominated the PV market. As an alternative, Rauer *et al.*, investigated local aluminum-alloyed contacts printed with Al pastes containing different amounts of silicon[84,85]. This innovation opened the way for a new concept which combines dot-shaped LCO and screen-printing Al paste metallization. It was applied to the rear local Al-p^+ emitter cell concept with a front contact grid that was formed by Ag plating. The difficulties of forming point contacts by screen-printing metallization with common Al paste had been explained in Chapter 2 and other publications[84–86]. The dominant role

that Si-add of the Al paste played during the point contact formation had also been discussed in ref[86]. Although most industrial PV companies currently modify the LCO pattern design from line-shaped to dash-shaped, it is still not true "point" contacts. In this chapter, the screen-printed Al point contact is applied on the rear side of the *n*-PERT-RJ solar cells. These solar cells are embedded with rear Al point contacts. To further illustrate the impact of Si-add of the Al paste on the device level, varying amounts of Si-add are investigated. Then the detailed loss analysis on V_{OC}, J_{SC}, and FF of the devices are performed. In the last part, a "point-line" rear contact design is presented, demonstrating the flexible application of screen-printed Al point contacts and the additional bifacial gain of *n*-PERT-RJ solar cell efficiency.

3.2 Experimental

The experimental steps of manufacturing the *n*-PERT-RJ solar cells and the test samples for the $J_{0, \text{ Met (Al)}}$ extraction are identical to Section 2.2. The quantum efficiency (QE) and the reflectance data of the solar cells are determined between the wavelength of 300 and 1200 nm, using the solar cell analysis system LOANA[87] developed by pv-tools. The in-house cells' electrical performance measurements were obtained with a h.a.l.m. flasher system. Both sides of the measurement chuck had local contact pins in the five-busbars configuration, and the measurement chamber inside is fully was fully insulated against stray light. The calibration cell was processed in a similar sequence to the above-described process and was certified by Fraunhofer ISE CalLab.

3.3 Results and discussion

3.3.1 Open-circuit voltage loss

The well-known expression for the open-circuit voltage:

$$V_{OC} = V_T \times \ln (J_{SC} / J_0) \tag{3.1}$$

can be derived from the Shockley diode equation[88] under open-circuit condition. V_T is the thermal voltage (25.69 mV at 25°C), J_{SC} is the current density at short-circuit condition under illumination and J_0 is the saturation current density. In the above expression, the V_{OC} is inversely proportional to the natural logarithmic value of J_0. That means that the lower the values of J_0, the higher

the V_{OC}. In this section, the reduction of the saturation current density under the rear Al point contact ($J_{0, \text{Met (Al)}}$) by increasing the amount of Si-add in the Al pastes in exchange is investigated for a better V_{OC} performance. There are two strategies in order to reduce the $J_{0, \text{Met (Al)}}$ contribution (area-weighted $J_{0, \text{Met (Al)}}$) to the total recombination current density ($J_{0, \text{Total}}$). The first is to cut down the total rear contact area fraction. This can be achieved by applying point contacts instead of the linear structures (continuous or interrupted). Due to the poor passivation, the contact region becomes a severe recombination center which has high $J_{0, \text{Met (Al)}}$. A comprehensive mechanism for the formation of Al point contact has been discussed in the reference papers[84–86], and from those investigations, the role of Si-add in the Al pastes is to help form the point contact properly without any voids had been learned. Figure 3.1 shows scanning acoustic microscopy (SAM)[89–91] images of n-PERT-RJ solar cells whose rear sides are metallized with four different Al pastes described in the previous section. There is a high density of voids on the rear side of the solar cells that is induced by metallization with the Si-add free Al paste (Fig. 2.8(a)). The corresponding SAM image is shown in Fig. 3.1(a): black spots represent the existence of voids and reveal inferior point contact quality. The phenomenon (voids) will vanish when the devices are metallized with the Si-add Al pastes. There are no black spots anymore in Fig. 3.1(b)-(d).
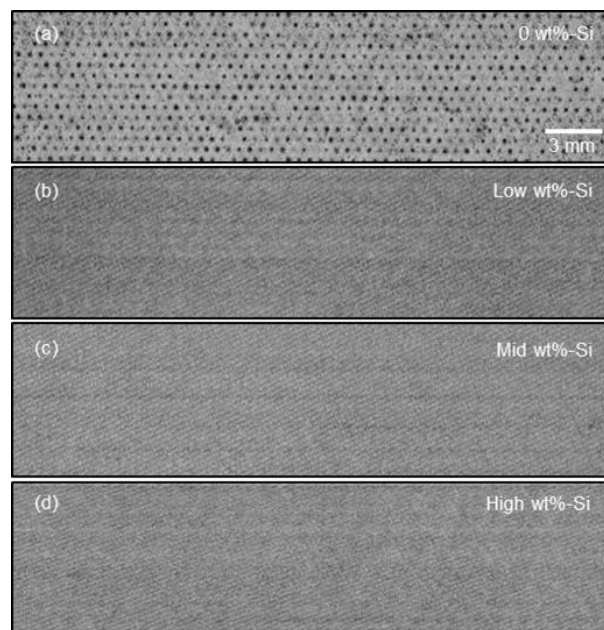
FIGURE 3.1 The scanning acoustic microscopy (SAM) images of the n-PERT-RJ solar cells, which rear sides are metallized respectively with (a) no, (b) low wt%, (c) mid wt%, and (d) high wt% Si-add Al paste.

It has also been found that increasing the amount of Si-add can reduce the point contact size. Fig. 3.2 illustrates the statistical results of the contact width (the diagonal in diamond shape or diameter in dot shape) measured by LSM. Obviously, when the amount of Si-add in the Al paste is increased, the average contact width is reduced from 125 µm to 60 µm, leading to a rear side contact area fraction that is in our case decreased from 5.9% to 1.3% of the wafer area. This is because the high wt% Si-add effectively reduces the silicon concentration ([Si]) gradient between bulk-Si and thick Al layer, successfully suppressing the silicon out-diffusion.
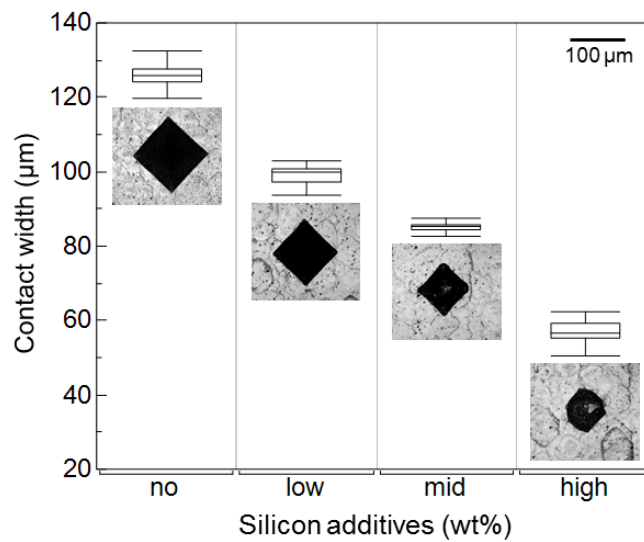
FIGURE 3.2. The contact width changes with different wt% Si-add in Al paste. (LSM images measured after firing and Al metal removal)

The second strategy to reduce the $J_{0, \text{Met (Al)}}$ is thickening of the Al-doped p^+ region: a thicker p^+ region underneath the point contact provides a better shielding of the contact area[43,92–95], reducing minority carrier recombination. The higher amount of Si-add in the Al paste, the longer silicon epitaxial growth time will be during the cooling down of the sintering process[86]. Hence, the thickness of the Al-doped p^+ region is increased when increasing the amount of Si-add in Al paste which effectively reduces the $J_{0, \text{Met (Al)}}$ from 2800 to 635 fA/cm^2, and improves the V_{OC} from 560 to 682 mV. Table 3.1 shows the measurement results regarding microstructures (the first two rows) and the electrical properties (the last two rows). Increasing the amount of Si-add in the Al paste simultaneously reduces both the rear contact fraction and the $J_{0, \text{Met (Al)}}$. As a

consequence, the V_{OC} obtains a great improvement and efficiency has been elevated to 21.61% (see Table 2.3).

TABLE 3.1. The Al point contact microstructures properties versus the Al pastes containing varying amount of Si additives.

	Silicon additives (wt%)			
	no	low	mid	high
Contact area fraction (%)	5.9	3.9	2.2	1.3
Al- p^+ thickness (μm)	0	0.6	2.4	3.2
$J_{0, \text{Met (Al)}}$ (fA/cm^2)	2839	1100	773	635
V_{OC} (mV)	560	675	680	682

3.3.2 Short-circuit current density loss

The microstructure and the $J_{0, \text{Met}}$ of Al point contacts were discussed in Section 2.3.2 and 3.3.1, and both can be improved by raising Si-add in the Al paste. Combining a smaller Al contact area fraction with lower $J_{0, \text{Met (Al)}}$, the V_{OC} can effectively increase, but are there any adverse impacts or sacrifices on J_{SC} and FF? In this section, the J_{SC} loss caused by the increasing amount of Si-add in Al pastes will be investigated. The solar cells whose rear sides are metallized with Si-add free Al paste will be excluded from the discussion here because of the inferior point contact characteristic properties; not only formed without Al-doped p^+ region but also accompanied by voids under the point contacts of this paste. Both measurement and fitting data of these solar cells are not suited anymore to act as control samples in the comparison with the solar cells whose rear sides are metallized with the Al paste containing varying amounts of Si-add. The rear side configuration of the solar cells strongly influences the reflectance of long wavelengths[84], especially in the wavelength range of 1100-1200 nm. The contributions are mainly the sum from rear side passivated and point contact (unpassivated) regions. When rear sides are metallized with identical Al paste, the long-wavelength reflectance is dominated by the pitch of dot-shaped LCO (see Fig. 3.3); the n-PERT-RJ solar cells whose rear sides are with an LCO pitch of 450 μm (blue lines) possess a higher reflectance at the wavelength range of 1100-1200 nm than those with LCO pitch of 350 μm (red lines) or 250 μm (black lines). Since the SiN$_x$ does not act merely as a passivation layer but also a better rear side reflector[96] than the bare silicon or Al-Si alloy, a higher LCO pitch (of identical spot diameter) leads to a higher percentage of rear-side area that is still covered (passivated) with SiN$_x$, thus having a higher

reflectance. In order to clarify how the long-wavelength reflectance is affected by the amount of Si-add in Al paste, a comparison has been made between solar cell devices with identical LCO pitch but metallized with Al pastes containing varying amounts of Si-add. The reflectance in a wavelength range of 1100-1200 nm is hardly affected by this variable (see Fig. 3.3), again explaining that the LCO pitch is the main influencing factor to the performance of the long-wavelength reflectance. The parasitic absorption of Si-add[84] within the rear Al metal layer is a minor effect.
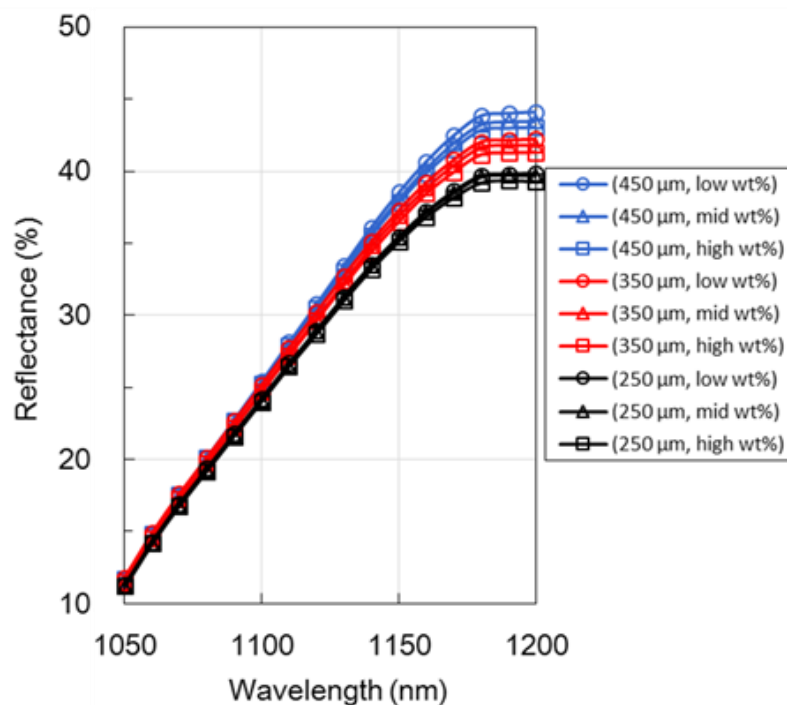
FIGURE 3.3. The reflectance of *n*-PERT-RJ solar cells at a wavelength range of 1100-1200 nm. The rear side of the cells are ablated with different LCO pitches and are metallized by using Al pastes containing varying amounts of Si additives. The text within the parentheses of the legend represents the LCO pitch and the amount of Si-add.

The external quantum efficiency (EQE) and the solar spectral irradiance[87] at air mass 1.5 segmentally between wavelength interval 1000-1200 nm are further integrated to get "partial" J_{SC} values, translating the reduction of reflectance to the J_{SC} loss. The results are shown in Table 3.2. The maximum J_{SC} loss induced by a lower reflectance is only 0.04 mA/cm², or even negligible. This explains why the J_{SC} values from I-V measurements in Table 2.3 are identical, although the rear sides of the solar cell devices are metallized with Al paste containing varying amounts (from low to high wt%) of Si-add. A short conclusion came out after analyzing the measurement data above: there's a

trivial drop on the reflectance at a wavelength range of 1100-1200 nm when the rear sides of solar cells are metalized with high wt% Si-add Al paste but the drop doesn't induce any obvious losses on J_{SC}.

TABLE 3.2 The "partial" J_{SC} of n-PERT-RJ solar cells contributed by a wavelength interval of 1000-1200 nm. The rear sides are ablated with different LCO pitches and metallized by using Al pastes containing varying amounts of Si additives.

	LCO pitch (μm)		
Si-add (wt%)	250	350	450
low	4.42 mA/cm²	4.46 mA/cm²	4.55 mA/cm²
mid	4.44 mA/cm²	4.49 mA/cm²	4.52 mA/cm²
high	4.42 mA/cm²	4.46 mA/cm²	4.51 mA/cm²

3.3.3 Fill factor loss

The primary concern of having Si-add in the Al paste is that the reduction of conductivity in the solar cell's rear electrode results in FF loss. In this section, we discuss how the series resistance (R_S) of the n-PERT-RJ solar cells is affected by the Si-add contents in the Al paste. From the solar cell's rear outside to inside, the components whose contributions to the R_S are directly affected by the Si-add contents in the Al paste are as follows (see Fig 3.4): (1) Al sheet resistance (R_{sh-Al}); (2) Al-Si alloy resistance (R_{alloy}); (3) contact resistance (R_{c-Al}) between Al-Si alloy and Al-doped p^+ region; (4) boron-doped p^+ rear emitter sheet resistance ($R_{sh-emitter}$).
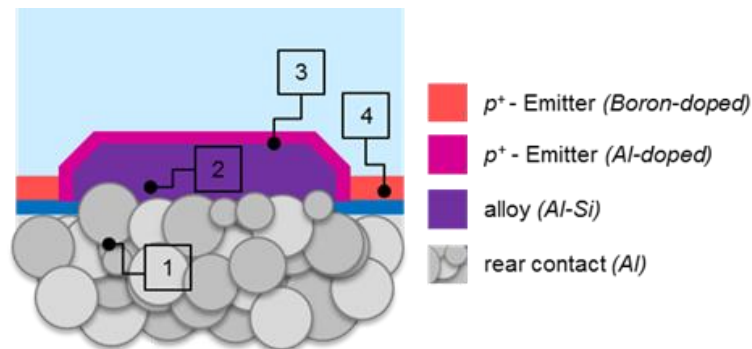
FIGURE 3.4 The components whose contributions to the R_S directly affected by the Si-add contents in the Al paste are: (1) rear Al sheet resistance (R_{sh-Al}); (2) rear Al-Si alloy resistance (R_{alloy}); (3) rear Al contact resistance (R_{c-Al}); (4) rear emitter sheet resistance ($R_{sh-emitter}$).

The contribution of the R_{sh-Al} to R_S is affected by two factors: (1) the R_{sh-Al} and (2) the carriers travelling distance ($d_{lateral}$) in the Al layer before reaching and being collected by the rear busbars. The R_{sh-Al} will be raised when increasing the Si-add contents in the Al paste, but the impact of raising the contribution of

$R_{\text{sh-Al}}$ to R_{S} is reduced by increasing the number of busbars (BB) to shorten the d_{lateral}. Four-point probe (4PP) measurements are performed for extracting the resistivity of the Al layers that are formed by the different Al pastes. Then the contributions to the R_{S} [97,98] based on the number of busbars are calculated, and the results are shown in Fig. 3.5. For the 5BB solar cells (the mainstream metal grid layout in today's PV market[16]), the increasing $R_{\text{sh-Al}}$ induced by the high wt% Si-add in the Al paste has much less contribution to the R_{S} than for the 3BB solar cells.
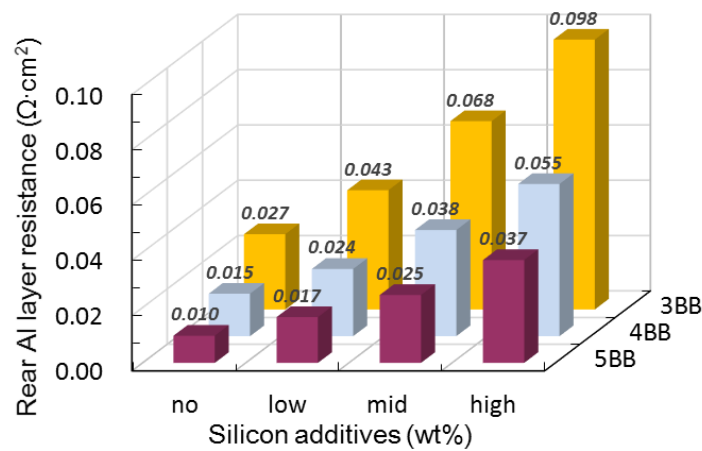
FIGURE 3.5 The rear Al layer sheet resistance ($R_{\text{sh-Al}}$) contributed to the series resistance (R_{S}) of *n*-PERT-RJ solar cells. The rear sides are metallized with Al pastes containing varying amounts of Si-add and busbar numbers.

We proceed to analyze the contributions from the other three components ($R_{\text{sh-emitter}}$, R_{alloy} and $R_{\text{c-Al}}$). They are of high relevance to the Al point contact formation. The R_{S} contributions from every $R_{\text{S-rear}}$ component of the 5BB *n*-PERT-RJ solar cells are depicted respectively in Fig. 3.6. The value of $R_{\text{sh-emitter}}$ is determined by the parameters of the diffusion process, but the contribution of $R_{\text{sh-emitter}}$ to R_{S} as calculated by the formula (6) in the reference[99] is affected by the amount of Si-add. When the amount of Si-add in the Al paste is increased, the decreasing contact width increases the shortest distance for carriers (holes) to transport in the collectors (emitter) before arriving at the point contacts. Even with the same $R_{\text{sh-emitter}}$, the smaller contact width will make a higher contribution to R_{S} (the orange blocks in Fig. 3.6).

There are three measurement difficulties in the detailed analysis of the R_{alloy} and $R_{\text{c-Al}}$: (1) the transfer length method (TLM) is used frequently to determine the contact resistance, but the general TLM setup can't be applied for
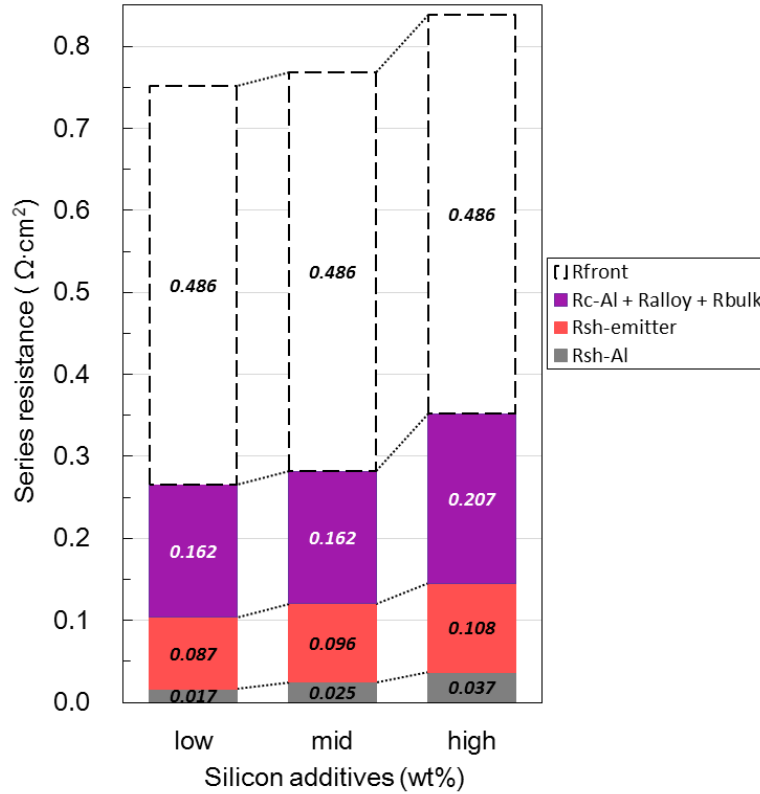
FIGURE 3.6 The series resistance (R_S) composition of the n-PERT-RJ solar cell with 5BB grid design. The rear sides are metallized with Al pastes containing varying amounts of Si-add.

measuring of point contacts; (2) even if it can be measured by using some approximations or based on certain assumptions[45], in our case, it is a challenge to separate the contribution of R_{alloy} and $R_{c\text{-}Al}$; (3) due to the high-level carrier injection and the lateral majority carriers (electrons) bulk transportation in the n-type and rear junction solar cells, the equivalent R_{bulk} extraction is much more complicated. Therefore, to simplify the comparison, the R_S contributions from R_{alloy}, $R_{c\text{-}Al}$ and R_{bulk} will be merged together and this sum can be extracted by subtracting other R_S contributions (i.e., R_{front}, $R_{sh\text{-}emitter}$ and $R_{sh\text{-}Al}$). The R_S is given by[100]:

$$R_S = V_{OC} / J_{SC} \times (1 - FF / pFF) \qquad (3.2)$$

and the pFF in (3) is acquired by using Suns-V_{OC} measurement[101]. The R_S contribution of the R_{front} is calculated using the formulas developed by Meier *et al.*[97] and the details are listed in Table 3.3. The R_S contribution of R_{alloy} and $R_{c\text{-}Al}$ extracted from the solar cells metallized with a high wt% Si-add Al paste is about 0.045 $\Omega \cdot cm^2$ higher than those metallized with a low wt% Si-add Al paste. We speculate that mainly due to the $R_{c\text{-}Al}$ is inversely proportional to the contact

area[99]. As shown in Fig. 3.2 and Table 3.1, when solar cells are metallized with higher Si-add content Al paste, the contact area becomes smaller.

TABLE 3.3 The R_S contribution of the R_{front}.

R_S Contribution	Extraction methods	Value	Unit
$R_{S\text{-}FSF}$	$(0.5 \times p_f)^2 \times$ effective $R_{sheet, FSF}$	0.299	$\Omega \cdot cm^2$
$R_{S\text{-}c\text{-}Ag}$	$\rho_{f\text{-}Ag}$ / front side f_m	0.067	$\Omega \cdot cm^2$
$R_{S\text{-}finger}$	Measured	0.097	$\Omega \cdot cm^2$
$R_{S\text{-}bb}$	Measured	0.023	$\Omega \cdot cm^2$
$R_{front} = R_{S\text{-}FSF} + R_{S\text{-}c\text{-}Ag} + R_{S\text{-}finger} + R_{S\text{-}bb}$		0.486	$\Omega \cdot cm^2$

Parameters	Extraction methods	Value	Unit
p_f (contact pitch)	Measured	2	mm
Effective $R_{sheet, FSF}$	$(1/R_{sheet, FSF} + 1/R_{sheet, bulk})^{-1}$	90	Ω/sq
$R_{sheet, FSF}$	Measured on p-type sample	150	Ω/sq
$R_{sheet, bulk}$	Bulk resistivity / Bulk thickness	222	Ω/sq
Bulk resistivity	Measured	4	$\Omega \cdot cm$
Bulk thickness	Measured	180	µm
$\rho_{f\text{-}Ag}$ (contact resistivity)	Measured on p-type sample	2	$m\Omega \cdot cm^2$
Front side f_m	Calculated	3	%

The R_S of the 5BB n-PERT-RJ solar cells which are metallized with the high wt% Si-add Al paste is 0.086 $\Omega \cdot cm^2$ higher than those metallized with the low wt% Si-add Al paste. More than 75% of this increment is highly correlated to the point contact formation. In order to clearly reveal the impact of the R_S increment (ΔR_S), an identical benchmark is needed. Therefore, we set the J_{SC} = 39.3 mA/cm², V_{OC} = 682 mV, and pFF = 84.7%. These electrical parameters are derived from the solar cells metallized with high wt% Si-add Al paste (see Table 2.3). We furthermore convert the determined ΔR_S to the solar cell's FF loss (ΔFF)[97] and efficiency drop (ΔEta):

$$\Delta FF = - \ (J_{SC} \ / \ V_{OC}) \ \times \ pFF \times \Delta R_S \qquad (3.3)$$

$$\Delta Eta = J_{SC} \ \times V_{OC} \ \times \ \Delta FF \qquad (3.4)$$

The 0.086 $\Omega \cdot cm^2$ R_S increment leads to a 0.4% loss in FF and translates to a 0.11% cell efficiency decrease (Fig. 3.7). The above FF loss analysis is only achieved under the assumption that when the solar cells are metallized with low wt% Si-add Al paste, it can still provide the same level of $J_{0, Met (Al)}$ and contact size as if metallized with high wt% Si-add Al paste. However, this has not actually occurred. On the contrary, the V_{OC} and pFF of the solar cells metallized

with the high wt% Si-add Al paste showed respectively 7 mV and 0.25% higher performance (see Table 2.3) than those metallized with low wt% Si-add Al paste. Summing up with all performance gains and losses, we finally acquire a benefit to the efficiency of our *n*-PERT-RJ solar cell. When further compared to the solar cells metallized with Si-add free Al paste, the performance improvement of the solar cell is even more pronounced.
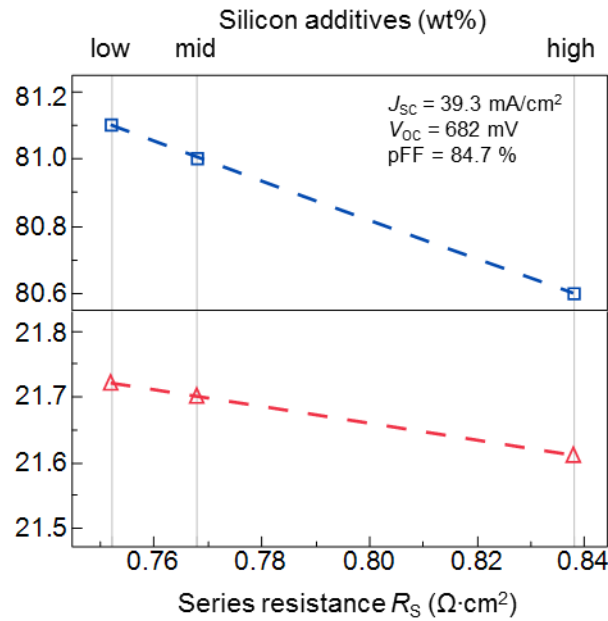
FIGURE 3.7 The FF loss and efficiency drop of the 5BB *n*-PERT-RJ solar cells are induced only by the increasing series resistance.

3.3.4 "Point-line" contact concept

After the loss analysis on the Al point rear contacts of the *n*-PERT-RJ solar cell, a "point-line" contact concept is demonstrated on the rear side, consisting of dot-shaped LCO and an Al finger grid design. The concept not only maintains the V_{OC} level but also provides an additional bifacial gain which further reduces the levelized cost of electricity (LCOE). The severe silicon out-diffusion via dot-shaped LCO is able to be constrained by managing the [Si] gradient. There are two strategies for the [Si] gradient management: (1) increasing the Si-add in Al paste or (2) decreasing the Al matrix above each LCO (decreasing the LCO pitch). Fig. 3.8(a) illustrates that when the amount of the Si-add in the Al paste is modified from no to high wt%, the contact width becomes gradually independent of the LCO pitch. In other words, Si-add dominates the effect of suppressing the out-diffusion of bulk-Si. Additionally, the $J_{0, \text{Met (Al)}}$ values are not affected by the LCO pitch when metallizing with a high wt% Si-add Al paste (Fig. 3.8(b)); they

all stay at about 650 fA/cm². The scanning electron microscopy (SEM) cross-sectional images in Fig. 3.9 show the thickness trend of the p^+ region that matches quite well the trend of $J_{0, \text{Met (Al)}}$ in Fig. 3.8(b). Fig. 3.10 shows the corresponding three-dimensional LSM images, and it is clear to see that the contact shape gradually changes from the inverted pyramid to hemisphere when increasing the amount of Si-add in the Al paste.
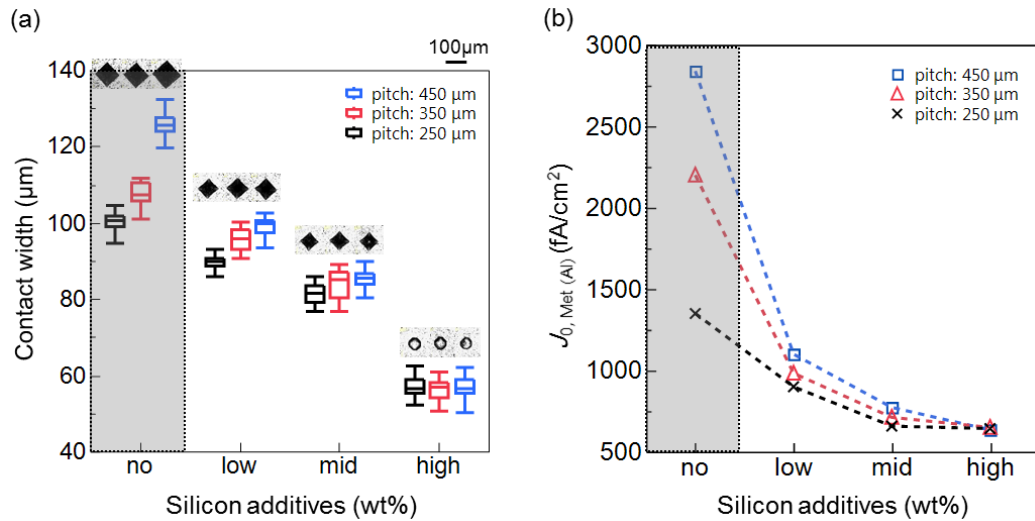
FIGURE 3.8. (a) Al point contact width measured by laser scanning microscopy (LSM). (b) $J_{0, \text{Met (Al)}}$ of samples metallized with different wt% Si-add contained Al pastes and different LCO pitches. Dashed lines serve as a guide to the eye. The grey background region illustrates the improper (high density of voids and $J_{0, \text{Met}}$) point contact formations.
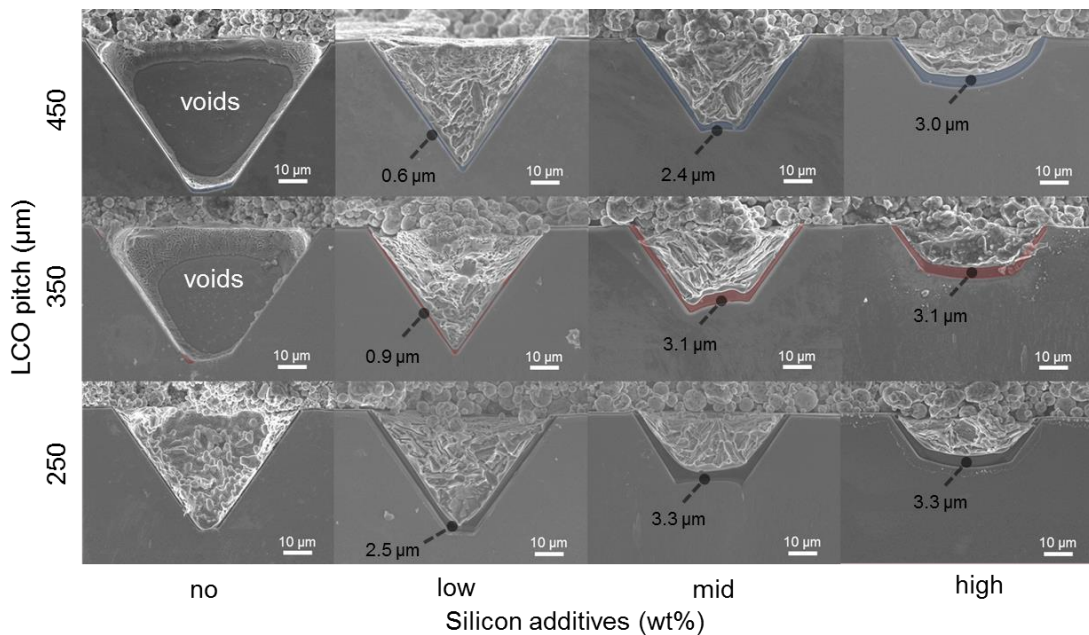
FIGURE 3.9. The cross-sectional microstructure images of Al point contacts were taken by scanning electron microscopy (SEM), color blocks represent Al-doped p^+ regions. The corresponding $J_{0, \text{Met (Al)}}$ are depicted in Fig. 3.8(b).
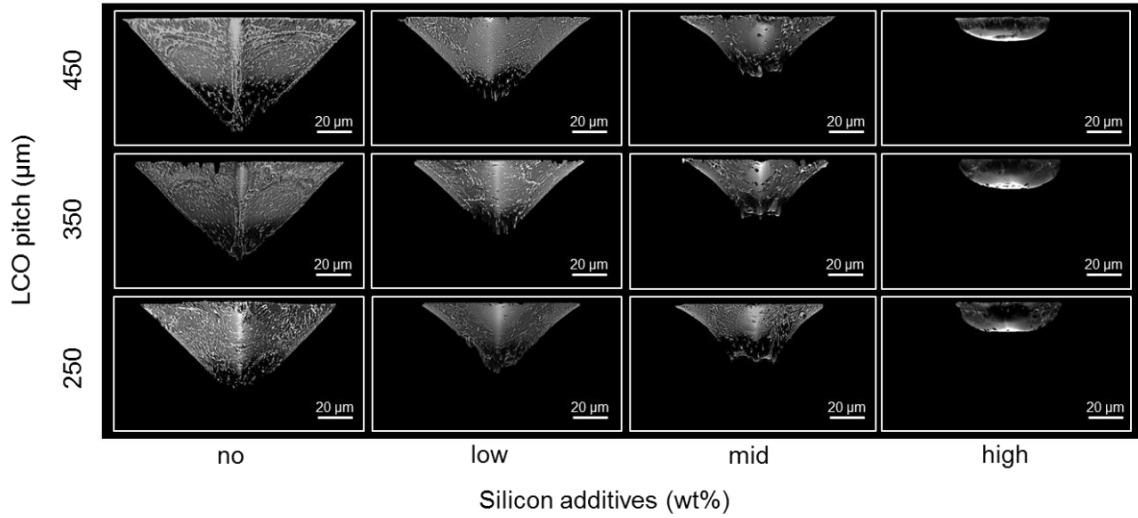
FIGURE 3.10. The laser scanning microscopy three-dimensional images of Al point contacts. The corresponding two-dimensional top view and cross-sectional SEM images are depicted in Fig. 3.8(a) and Fig. 3.9.

When the point contact formation is dominated by high wt% Si-add in the Al paste, the contact size and $J_{0, \text{Met (Al)}}$ will no longer be affected by the space of the Al matrix above each LCO point (refer to Fig. 3.8). Based on this finding, the Al paste matrix design above the LCO points is reduced from fully covered to a limited 180 µm wide finger grid forming "point-line" contacts and applied on the latest optimized n-PERT-RJ solar cell's rear side. In Table 3.4, the V_{OC} is identical between the point-line and full-area rear Al contact design, which confirms the hypothesis on the domination of the [Si] gradient management as proposed previously in Chapter 2. Due to higher Al line resistance (1.5 Ω/cm), the FF drops around 0.4%, but in exchange for possessing an additional 60% bifaciality and with a cell efficiency still approaching 22%. After optimization of the Al grid aspect ratio and LCO pitch design, the bifaciality can be further improved.

TABLE 3.4 Averaged and champion n-PERT-RJ cell performance with a "point-line" contact design on the rear.

	J_{SC} (mA/cm^2)	V_{OC} (mV)	FF (%)	Eta (%)	Bifaciality (%)
Averaged (10 cells)	40.0	692	79.3	21.95	60%
Champion (front)	40.0	692	79.4	21.98	59%
Champion (rear)	23.7	678	80.2	12.89	-
Fully Al metallized	40.0	692	79.7	22.06	0%

(5BB grid design, in-house measurement using an ISE CalLab calibrated reference cell)

3.4 Conclusion

Based on the knowledge from the previous investigation[86], the decisive role that the Si-add play during the Al point contact formation is known. In this study, the investigation was divided into four parts:

1) Combined with the microstructure and $J_{0, \text{Met (Al)}}$ analysis, we found that the best Al point contact characteristics (thicker Al-doped p^+ region and no voids) were reached for metallization of the high wt% Si-add Al paste. A V_{OC} gain of 7 mV can be obtained compared to the devices which were metallized with a low wt% Si-add Al paste.

2) From the perspective of the J_{SC} loss, we analyzed the rear side reflectance, which was not affected by any amounts of Si-add in Al paste. The Si-add in the Al paste didn't cause J_{SC} loss.

3) The R_S raised when the amount of Si-add in Al paste was increased. The major resistance increment didn't come from the decreasing conductivity of the Al metal layer. With the premise of identical contact characteristics, when the devices were metallized with a high wt% Si-add Al paste, the FF loss was 0.4%. However, a better pFF value was obtained, which compensated for the FF loss.

4) The "point-line" contact concept was implemented after investigating on how Al point contact formation was affected by different LCO pitches and the Si-add contents in the Al pastes. We retained the same point LCO design but printed an Al finger grid pattern instead of a fully covered rear side. This contact concept helps maintain the same V_{OC} while acquiring an additional bifacial gain.

Based on the analysis results of microstructure, V_{OC}, J_{SC} and FF, we can conclude that having the Si-add in the Al pastes not only makes screen printed point contact feasible and provides a better cell performance but also opens high flexibility on the rear metallization design. Last but not least, integrating dot-shaped LCO with screen-printing Al paste then co-firing with front side Ag thick film metallization makes the point contact concept adaptable to mass production.

Chapter 4: Industrial Screen-Printed *n*-PERT-RJ Solar Cells: Efficiencies Beyond 22% and Open-Circuit Voltages Approaching 700 mV

4.1 Introduction

Solar cell concepts based on *n*-type monocrystalline Czochralski-Si (*Cz*-Si) wafers offer several advantages: because of phosphorus-doped Si as the base, they are free of light-induced degradation (LID)[18,102] almost free of light and elevated temperature induced degradation (LeTID)[103] and less sensitive to metal impurities[37]. They are mostly sorted into two classifications by the metallized contact sides: backside contacted (i.e., interdigitated back contact (IBC)[104] solar cells), or both sides contacted (i.e., passivated emitter rear totally (PERT) or locally diffused (PERL)[38] solar cells). Depending on the emitter junction location, the PERT cell concept can be further subdivided into the front[105] or the rear junction type[106] (the front junction indicates the emitter side facing the sun directly). In this chapter, the study still focuses on the <u>n</u>-type <u>p</u>assivated <u>e</u>mitter and <u>r</u>ear <u>t</u>otally diffused <u>r</u>ear junction (*n*-PERT-RJ) solar cell concept. It was introduced as a laboratory-type solar cell by Dai *et al.*[38] in 1993. Since there was a lack of tube furnace boron diffusion suited for PV demands on large-area devices, Kopecek *et al.*[107] and Schmiga *et al.*[108] applied screen printed Al paste to form a rear junction (Al-doped p^+ region) on large wafer area leading to a cell efficiency of 16.4% and 18.2% respectively. However, these early rear junction cell concepts were without any additional rear side passivation and were therefore not a true "PERT" solar cell concept. A few years later, Bock *et al.*[109] passivated a fully Al paste generated p^+ rear junction by a-Si/SiO$_x$ stack after removal of the covering Al metal layer. PVD-Al on the entire rear surface was deposited in order to form contacts on the local photolithographic opening sites and the solar cell efficiency reached 20.0%. Bordihn *et al.*[110] replaced the rear junction formation by boron diffusion and reached to 20.2% cell efficiency. Improved processing of tube furnace boron diffusion, the availability of industrial-type laser equipment for local contact openings (LCO) and the launch of screen-printing Al pastes for LCO opened up solutions for *n*-PERT-RJ solar cell concepts with a "hybrid" rear junction. It is composed by boron doping -using a tube furnace- and Al-doping -using screen-printed Al paste-. The non-

contacted p^+ region can be well passivated and the contacted p^+ region possesses low recombination. Moreover, the entire process is much simpler than in the past. Fig. 2.3 shows a schematic cross-section of our latest n-PERT-RJ solar cell concept.

As a consequence of an increasing number of research institutes and industrial companies invested in research and development in this field[111–114], the cell efficiency improved to 21.9% in 2017[103] and 23% (busbar-less cell measured by Grid[TOUCH] system[115]) in 2018[116]. In addition to the n-type relevant advantages mentioned at the beginning, the n-PERT-RJ cell concept has more advantages:

1) Due to the presence of a phosphorus-doped n^+ front surface field (FSF) in a parallel circuit with the n-bulk, the effective sheet resistance (R_{sheet}), combining both n-type layers, is lower. The resulting higher lateral conductivity of this double layer has the potential for around 20% lower Ag consumption compared to the p-type passivated emitter and rear cell (p-PERC) concept[49,117] having the same phosphorus doping profile on the front side. This opens the way for ultra-lowly doped profiles aim for acquiring lower recombination, which is no longer suited for p-PERC's emitter application.

2) The highly doped p^+ boron emitter region on the rear side reduces the spreading resistance loss[118,119]. This opens up the possibility to further decrease the rear contact area fraction because of the higher lateral conductivity. In our case, the rear side LCO (the same unit spot size) ratio is reduced from 8% (traditional line-shape) to 1% (advanced dot-shaped)[120,119].

3) The processes can be upgraded from an existing p-PERC industrial production line, just by appending a boron diffusion tube furnace for forming the rear emitter and replacing AlO$_x$ passivation.

Currently, the p-PERC solar cell's capacity is predicted to have_around 35% market share until 2019 and the PERX (PERC/PERT/PERL) solar cell concepts are expected to gain significant market share and will enter the mainstream market after 2021[121]. Most of the manufacturers and researchers have declared

that the LID and LeTID on *p*-PERC solar cells can be addressed by appropriate treatments[122–124] or different wafer materials[125]. However, the additional steps increase the costs and no one can guarantee that the effect is still working after years of field operation. This reveals the benefits of the *n*-PERT-RJ solar cell concept to provide long term stability, cost-effective structure and high-efficiency conversion potential with the option for an easy feasible industrial solar cell process. The cost of ownership (COO) for our *n*-PERT process is calculated to be in some cases lower than for standard *p*-PERC process; the difference is even larger when calculating the levelized cost of electricity (LCOE)[29].

In this chapter, the development work is presented in a large area, fully screen-printed, homogeneous FSF *n*-PERT-RJ solar cells, based on already well-established processes and technologies in the industry. High open-circuit voltage (V_{OC}) is not only beneficial for the cell efficiency measured under standard test condition (STC) but also contribute to better module-level performance, especially in the desert regions[126], as the corresponding solar cells have a lower temperature coefficient. Lowering the $J_{0, \text{Total}}$ is the key to achieve high V_{OC}. To minimize the $J_{0, \text{Total}}$ for our cell device structure, the FSF doping profiles optimization will be focused on, front side Ag grid designs and recombination current density under rear Al contacts. The champion cell efficiency beyond 22% is demonstrated with a V_{oc} up to 693 mV. Through detailed loss analysis, the roadmap with precise improvement steps is provided for achieving cell performance beyond 700 mV V_{OC} and 23% cell efficiency.

4.2 Experimental

The experimental steps of manufacturing the *n*-PERT-RJ solar cells and the test samples for the $J_{0, \text{Met (Al)}}$ extraction are identical to Section 2.2. The extraction of recombination current density for the front side Ag fingers, $J_{0, \text{met (Ag)}}$ followed the procedures described in the reference paper[127]. The surface doping concentration profiles were measured by electrochemical capacitance-voltage (ECV) method[128]. The contact resistivity of the Ag contact (ρ_f) printed on the FSF was evaluated using the transfer length method (TLM)[129]. The internal quantum efficiency (IQE) data is determined between the wavelength of 300 and

1200 nm, using the solar cell analysis system LOANA[87] developed by PV-tools. The in house cell's electrical performance measurements were performed with an h.a.l.m. flasher system. The measurement method was based on a "hysteresis measurement" in which the IV-curve is measured from I_{SC} to V_{OC} and from V_{OC} to I_{SC} within a single light pulse[130]. The calibration cell was processed in a similar process sequence and was certified by Fraunhofer ISE CalLab.

4.3   Results and discussion

4.3.1   Front surface field optimization

With drive-in duration optimization of phosphorus diffusion, a shallow FSF is generated which has a higher sheet resistance (R_{sheet}) and shallower junction depth than our baseline. Fig. 4.1(a) depicts the two FSF doping profiles determined by ECV, the doping profile of the shallow FSF has a slightly higher surface doping concentration (N_{surf} = 2.0×10^{19} cm^{-3}) than the baseline (N_{surf} = 1.7×10^{19} cm^{-3}). Hence in Fig. 4.1(b), the ρ_f printed on the shallow FSF is not obviously different but just 0.3 m$\Omega \cdot$cm^2 lower than printed on the baseline doping profile.
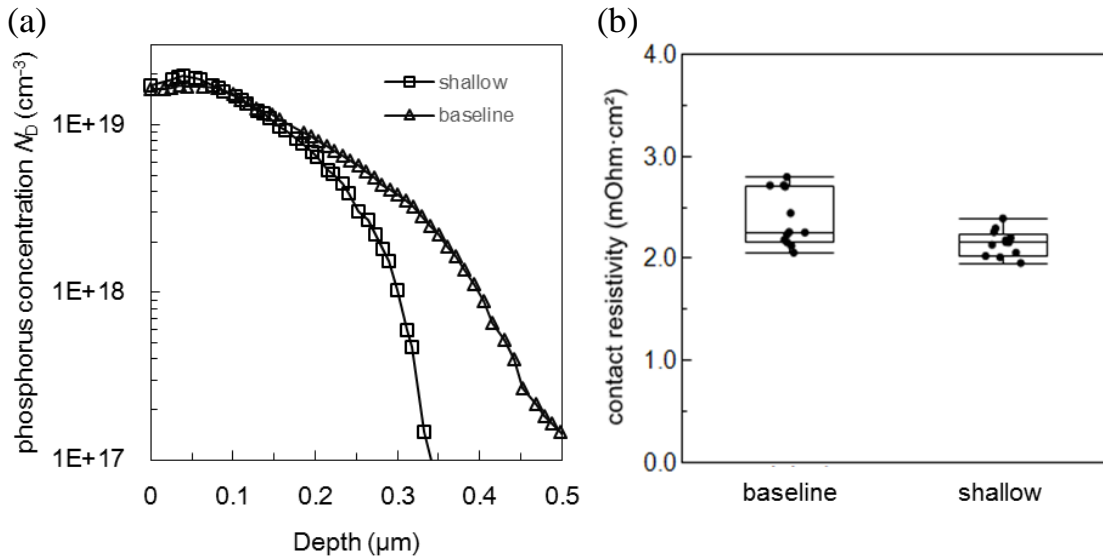
FIGURE 4.1. (a) The phosphorus doping profiles of FSF. (b) The contact resistivity of Ag contact (ρ_{fc}) printed on the baseline and shallow FSF.

The recombination current density of the shallow FSF ($J_{0,\ FSF}$) is 25 fA/cm^2 which is 5 fA/cm^2 lower than the $J_{0,\ FSF}$ of baseline FSF. This is at-tributed to the shallower doping profile reduces the total amount of phosphorus dopant within the FSF bulk region, leading to less Auger recombination and therefore

longer charge carrier lifetime and diffusion length which is confirmed by EDNA 2 simulations[131]. Another indicator used to characterize the FSF quality is the IQE measured on a finished solar cell. It describes the probability of light generated carriers being collected and contributing to the current as a function of wavelength. Due to the high absorption coefficient for short wavelength light in the upper part of our device, the IQE in this wavelength range can be used to quantify the electronic quality of the FSF doping region[132]. Table 4.1 shows the characterization of the two FSF phosphorus doping profiles_discussed above. Decreasing the junction depth from 0.5 µm to 0.35 µm elevates the R_{sheet} from 150 Ω/sq to 180 Ω/sq while reducing $J_{0, FSF}$. The IQE at a wavelength of 350 nm reveals a clear increment on the shallow FSF doping profile which allows a higher carrier collection probability. It confirms once again on the better performance of the shallow FSF. The decrease in area-weighted $J_{0, FSF}$ increases the cell's V_{OC} by approximately 2 mV.

TABLE 4.1. Characterization of the FSF doping profile.

FSF	Junction depth (µm)	R_{sheet} (Ω/sq)	$J_{0,FSF}$ (fA/cm^2)	IQE @ 350nm (%)
baseline	0.50	150	30	95.8
shallow	0.35	180	25	97.3

4.3.2 Metallization induced recombination under front Ag contacts

The performance of front-side metallization (Ag finger) is not only determined by line conductivity, contact resistivity and light shading. The metal-silicon interface of a phosphorus-doped FSF provides a severely recombination active surface for holes. The undesirable impact of this loss mechanism needs to be minimized, hence various selective doping methods have been proposed. Different ways for performing selective doping have been studied such as laser doping from PSG[133,134], etching back with mask[135,136], printing with doping pastes[137] and using ion implantation[138,139]. These selective doping technologies are designed for making heavier doping under metal contacts and shallower doping elsewhere. It provides the benefits of having both, a low specific contact resistivity and better shielding under metal contacts. With rapid developments in laser technology, laser doping now is the mainstream process for forming a selective doping structure. However, there are two major

undesirable side effects induced by applying the laser doping process. First, owing to the alignment margins for finger printing and the native laser spot size, the laser doping area is around three to four times wider than the finger width. After deducting the Ag contact regions, the residual regions are passivated but possess a higher $J_{0, FSF}$ than the other passivated regions without laser doping. Second, an additional FSF passivation step after PSG removal is needed for lower $J_{0, FSF}$ which will increase the manufacturing costs. In our cell optimization, the recombination current density under Ag contact ($J_{0, Met (Ag)}$) is minimized by decreasing the metal fraction of the Ag contacts. There are two strategies presented on how to avoid the implementation of selective FSF structures: changing to fine-line printing and applying the dash contact concept. A commercial firing through Ag paste was printed on the textured FSF surface, which has the phosphorus doping profile shown in the previous section, and results in a $J_{0, Met (Ag)}$ of around 1200 fA/cm². A narrower finger width (40 µm) is applied, reducing the metal fraction to 2% of the wafer area. Then the design of the metal grid was changed. First, dashes (300 µm length) are printed with the firing through Ag paste to form the "effective" contact and afterwards printed the second layer for connecting these dash contacts with non-firing through Ag paste. A top view image of the metal grid design taken by the LSM is shown in Fig. 4.2.
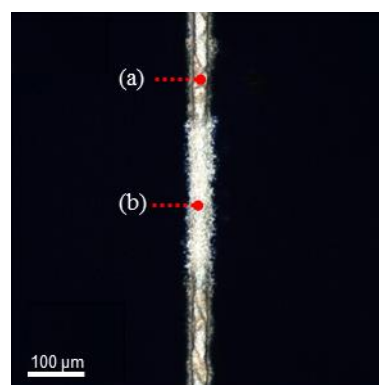
FIGURE 4.2. The top view of the screen-printed Ag finger which is composed of (a) firing through paste and (b) non-firing through paste.

For solar cells, there is always a trade-off between effective contact area and fill factor (FF). To illustrate the situation for our *n*-PERT-RJ cells, the electrical properties of the solar cells are simulated by Quokka3[140]. The results are shown in Fig. 4.3. When varying the proportion of the finger area printed with firing

through Ag paste from 100% to 50%, there is a 4 mV gain in V_{OC} and it comes with almost no efficiency drop. For a further reduction of this proportion, the V_{OC} gain is overcompensated by the corresponding FF loss and hence brings in no benefit to the cell efficiency. Using two sintering steps (fingers only and then busbars) which are described as the previous studies[141], the ρ_f in this chapter can still be kept at around 2 m$\Omega \cdot$cm^2 (refer Fig. 4.1(b)) even for N_{surf} = 2×10^{19} cm^{-3}. By applying the concept of fine-line printing and dash contacts in the design of front metal grids, the firing through Ag contact fraction is reduced to 1% of the wafer area, resulting in the area-weighted $J_{0, \text{Met (Ag)}}$ decreasing by 67% from 37.2 fA/cm^2 to 12 fA/cm^2. This brings a 6 mV V_{OC} gain on the cell devices. Cutting down the firing through Ag contact area is a striking strategy for minimizing the area weighted $J_{0, \text{Met (Ag)}}$, and moreover, without additional costs, it makes the n-PERT-RJ solar cell concept more cost-effective.
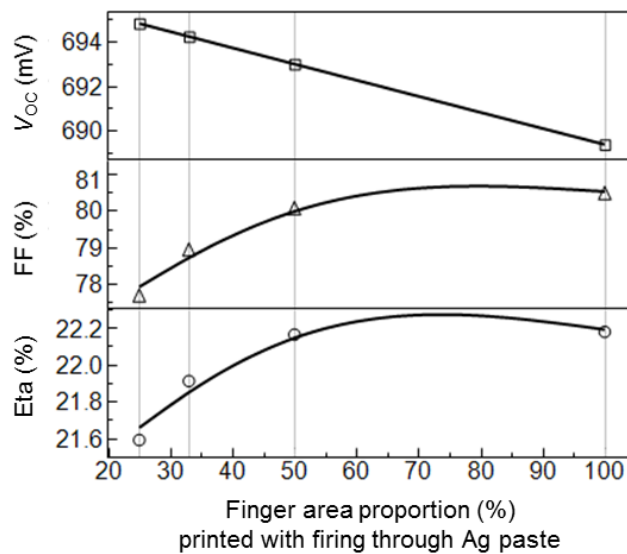
FIGURE 4.3 Simulated electrical parameters by Quokka3 with varying the proportion of the finger area printed with the firing through Ag paste.

4.3.3   Metallization induced recombination under rear Al contacts

The n-PERT-RJ solar cell concept has a full passivated rear side, which induces much lower rear side recombination losses compared to the traditional BSF solar cell concept. In this chapter, the rear side boron doping diffusion profile with borosilicate glass (BSG)/ SiN$_x$ passivation stack[142] has been optimized to 200 Ω/sq R_{sheet} and 17 fA/cm^2 $J_{0, \text{Emitter}}$. In addition to the passivated region on the rear side, the high recombination active region under the Al

contact is the most influential part of the rear side that plays a key role in solar cell performance. There are two optimization directions: first, reducing the contact area fraction and second, reducing the value of the recombination current density under the Al contact ($J_{0, \text{Met (Al)}}$). In this section, the screen-printed Al point contact is introduced. Controlling the reaction between Al and Si during the contact formation is the key to make point contact feasible[81,84–86]. Increasing the Si additives in Al paste can effectively mitigate the out-diffusion of bulk-Si during heating up of the firing process and prolong the growth time of the Al-p^+ region during cooling down of the firing process[86]. A thicker Al-p^+ region is formed by [Si] gradient management which supplies a better shielding[43] preventing minority carrier recombination under the contact region, hence lowering the $J_{0, \text{Met (Al)}}$ from 1100 fA/cm² to 635 fA/cm². The results are depicted in Fig. 4.4.
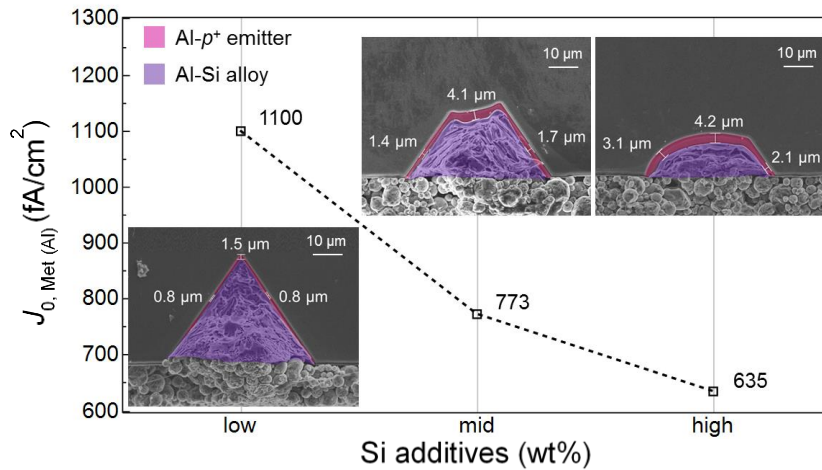
FIGURE 4.4 The $J_{0, \text{Met (Al)}}$ values extracted from (1) by QSSPC measurement of the symmetric test structures which are printed with different amounts of Si additives in the Al pastes. Appended with the cross-sectional images of point contact spots taken by scanning electron microscopy (SEM), red color blocks indicate the Al-doped p^+ regions.

Furthermore, in Table 4.2, the contact area is also varied with the amount of Si additives in the Al paste. The Al contact area fraction is further reduced from 4% to 1.3% of the wafer area when the amount of Si additives in the Al paste is increased. The area-weighted $J_{0, \text{Met (Al)}}$ drops from 44 to 8.2 fA/cm² resulting in about 7 mV increment of V_{OC}.

TABLE 4.2. Characterization of the Al point contacts.

Description	Symbol	Unit	Si additives		
			low	mid	high
Recombination current density	$J_{0,\,Met\,(Al)}$	fA/cm^2	1100	773	635
Contact area fraction	f_m	%	4	2.3	1.3
V_{OC} gain	ΔV_{OC}	mV	0	5	7

4.3.4 Summary of the V_{OC} optimizations

In the previous sections, the methods to minimize the recombination current density has been discussed. Fig. 4.5 summarizes on the step by step gains in V_{OC} of the *n*-PERT-RJ solar cells, from 676 mV to 693 mV. The V_{OC} gains can be mainly attributed to the three actions (ordered by the chronology of the 6 experiments):
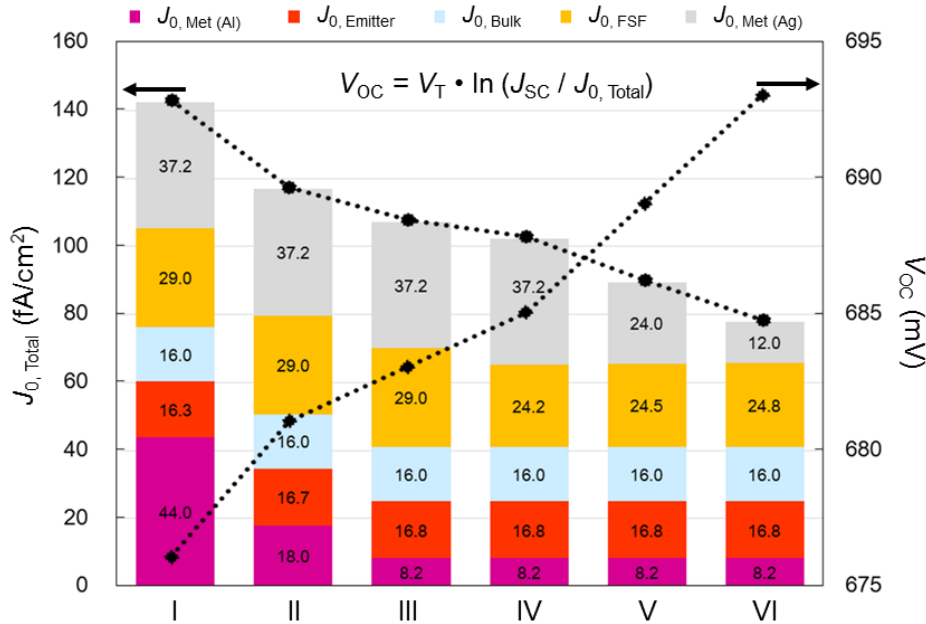
FIGURE 4.5. Roadmap from 676 mV to 693 mV V_{OC} of the *n*-PERT-RJ solar cell. The $J_{0,\,Total}$ is the sum of each part area-weighted J_0; the area-weighted J_0 is calculated by the measuring area and J_0. The calculated V_{OC} by the $J_{0,\,Total}$ is matched to the measured V_{OC} of the *n*-PERT-RJ solar cell devices.

1) The first gain in V_{OC} is from the application of screen-printed Al point contact on the rear side, which reduced the total contact area. The Si additives in the Al paste make point contacts feasible. From the stage I to III, the amount of Si additives is increased from low to high. At the same time, $J_{0,\,Met\,(Al)}$ and the total Al contact areafraction are further reduced to 635 fA/cm^2 and 1.3% respectively and the V_{OC} is improved by 7 mV to 683 mV.

2) The shallower phosphorus doping profile of FSF gives less Auger recombination, which reduced the $J_{0,\,FSF}$ of the texturized surface to 25 fA/cm² and provides a 2 mV at stage IV to the V_{OC} level of 685 mV.

3) Without any additional selective FSF process steps, merely reduced the front side firing through Ag contact area fraction by (a) decreasing the screen-printed finger width from 60 µm to 40 µm (stage IV to V); (b) printing of dash contacts with firing through Ag paste (stage V to VI). Under the premise not to decrease the cell efficiency, the firing through Ag contact area is reduced to half of the fine-line grid design in (a). After optimization, the firing through Ag contact area fraction of the front side is reduced to only 1% of the wafer area, resulting in a V_{OC} of 693 mV.

It's worth noting that after applying front side dash contact and rear side point contact patterns for our screen-printing metallization, the metal-induced recombination $J_{0,\,Met}$ (sum of $J_{0,\,Met\,(Ag)}$ and $J_{0,\,Met\,(Al)}$) is reduced from near 60 % to near 25 % of the $J_{0,\,total}$ (Fig. 4.6). The $J_{0,\,Met}$ is no longer the bottleneck of the $J_{0,\,total}$ as it was before. Without any advanced process tools, the champion cell was processed with 693mV in V_{OC} and 22.16% in efficiency (refer to Table 4.3).
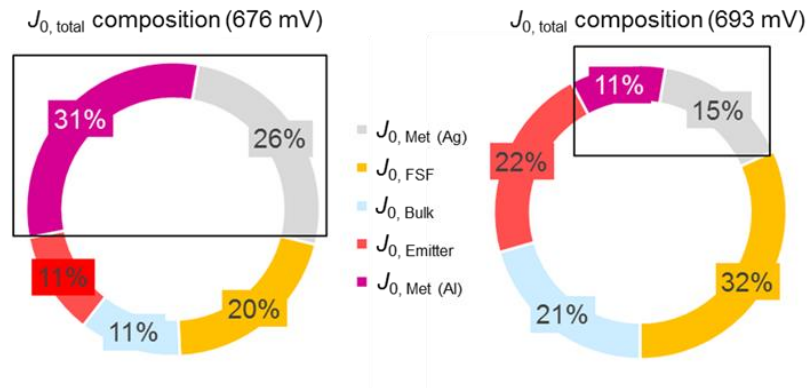
FIGURE4.6. Saturation current density, J_0 distribution of a 676 mV cell (left) and 693mV (right) cell V_{OC} n-PERT-RJ solar cell.

TABLE 4.3. Average and champion *n*-PERT-RJ cell performance.

	J_{SC} (mA/cm²)	V_{OC} (mV)	**FF** (%)	**Eta** (%)
Averaged (7)	40.0	692	79.74	22.05
Champion	40.0	693	80.06	22.16

(5BB grid design, in-house measurement using an ISE CalLab calibrated reference cell)

4.3.5 Loss analysis for a 22.2% *n*-PERT-RJ solar cell

Detailed loss analysis of the *n*-PERT-RJ solar cell can help us to comprehend the various loss mechanisms which limit the solar cell performance. It further indicates which part of the cell should be improved with a higher priority. In this section, the loss analysis is performed by Quokka3, a three-dimensional device simulation tool which uses the conductive boundary (CoBo) approach to define each "skin" in terms of the measurable quantities (sheet resistances R_{sheet} and saturation current densities J_0), and calculating the silicon bulk as a quasi-neutral region. The geometry of the unit cell model is depicted in Fig. 4.7. The front and rear side of the solar cell are defined as skins. A skin layer is a homogeneous area covering between the Si-bulk and the metal. It can be defined as a contacted or non-contacted area. The front n^+ skin of the unit cell is contacted locally by an Ag finger and busbar, the rear p^+ skin is contacted locally with a fully covered Al layer.
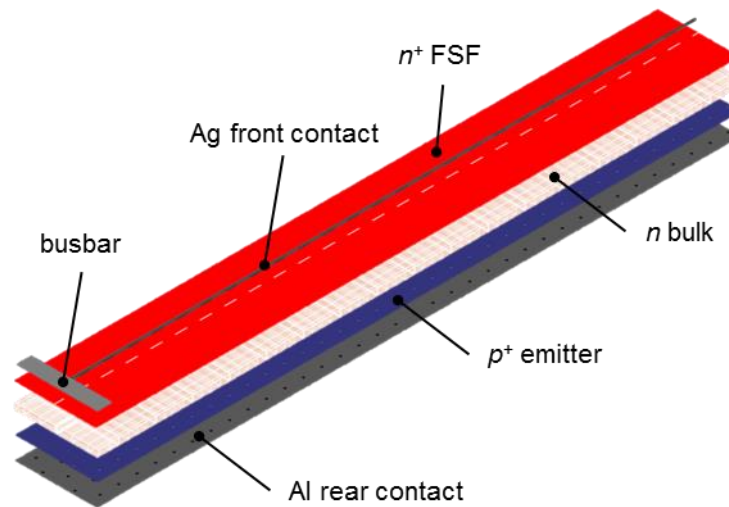
FIGURE 4.7. Three-dimensional geometry of the *n*-PERT-RJ unit cell for Quokka3 simulation, the front refers to the illuminated side.

The input parameters for the simulations are extracted from a measured 22.16% efficient *n*-PERT-RJ solar cell. After a series of detailed cell characterizations, the input parameters are listed in Table 4.4. In combination with an accurate photo-generation profile, the simulated electrical properties match very well with the measured cell data, as summarized in Table 4.5. A "free energy loss analysis" (FELA) is performed which quantifies efficiency losses in the modelled *n*-PERT-RJ unit cell device at the maximum power point

(MPP) for standard testing condition (STC) to different cell regions. The FELA within the unit cell can be categorized into two loss mechanisms (Fig. 4.8): the recombination losses representing a 1.47% loss and the resistive losses that are totally about 1.21%. Each mechanism is further resolved into their individual loss items. The largest single loss (0.54%) is observed for the recombination at the FSF. However, the $J_{0, \text{FSF}}$ value of 25 fA/cm^2 is already low for a textured surface with 180 Ω/sq sheet resistance and passivated with thermal silicon dioxide[143]. The second and the third biggest loss contributions are the recombination (0.39%) and resistive (0.34%) losses in the bulk. These can be improved by implementing a higher bulk carrier lifetime and changing to a lower bulk resistivity material. Shortening the transport distance for the holes to the rear emitter by applying a thinner wafer can further reduce the resistive losses. However, with reducing wafer thickness, irradiation absorption decreases[144] and leads to higher current loss. After the top three, the efficiency loss order then is followed by: FSF lateral resistive loss (0.27%) which is already optimized by trading off with the front finger pitch (shading); front contact resistive loss (0.26%) which can be optimized further with a selective doping process; emitter recombination loss (0.26%) which could be tackled with optimized doping profile and surface passivation. The major efficiency losses discussed above can be addressed in exchange for an obvious performance gain.

TABLE 4.4. Input parameters used in Quokka3 device modelling for detailed loss analysis.

Parameter	Symbol	Value	Unit
Bulk resistivity	ρ_b	2.8	Ω·cm
Bulk minority-carrier lifetime	τ	3.5	ms
Contact pitch on front side	p_f	2	mm
Contact width on front side	w	40	μm
Contact resistivity on front side	ρ_f	2	mΩ·cm^2
Line resistance of Ag finger	R_L	0.4	Ohm/cm
Recombination of front contact	$J_{0, \text{Met (Ag)}}$	1200	fA/cm^2
Sheet resistance of phos.-n^+ FSF	$R_{\text{sheet, FSF}}$	180	Ω/sq
Recombination of pass. phos.-n^+ FSF	$J_{0, \text{FSF}}$	25	fA/cm^2
Contact pitch on rear side	p_r	0.45	mm
Contact radius on rear side	r	30	μm
Contact resistivity on rear side	ρ_r	1.2	mΩ·cm^2
Sheet resistance of Al contact	$R_{\text{sheet, Al}}$	0.04	Ω/sq
Recombination of rear contact	$J_{0, \text{Met (Al)}}$	635	fA/cm^2
Sheet resistance of boron-p^+ emitter	$R_{\text{sheet, Emitter}}$	200	Ω/sq
Recombination of pass. boron-p^+ emitter	$J_{0, \text{Emitter}}$	17	fA/cm^2
Shunt resistance	R_{shunt}	12000	Ω

TABLE 4.5. Simulated and experimental *n*-PERT-RJ cell performance.

	J_{SC} (mA/cm^2)	V_{OC} (mV)	FF (%)	Eta (%)
Simulated	39.95	692.7	80.11	22.18
Measured*	39.98	692.9	80.06	22.16

(5BB grid design, in-house measurement using an ISE CalLab calibrated reference cell)
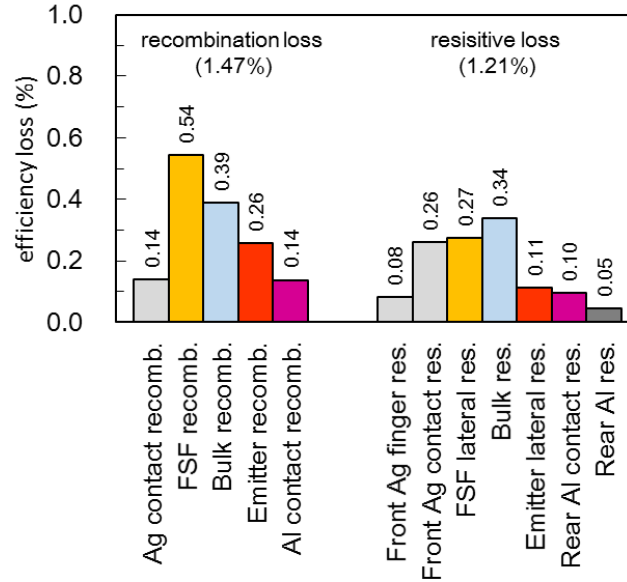
FIGURE 4.8. Recombination and resistive losses extracted from free energy loss analysis (FELA). Results of the *n*-PERT-RJ cells carried out at the maximum power point (MPP).

4.3.6 Roadmap toward 700 mV open-circuit voltage

The highest V_{OC} value of the *n*-PERT-RJ solar cell presented in this chapter is 693 mV. With modifications in the cell process, to achieve a 700 mV V_{OC} value is our next target. Utilizing the Quokka3 simulation model which was built up in the previous section, the simulations with different recombination related parameters are performed to predict the potential gain on the V_{OC}. Improving the passivation quality of the front textured (rear flat) surface or optimizing the doping profile is the definite solution for higher V_{OC}. Regarding the surface recombination, the bulk lifetime (τ_{bulk}) also affects the cell's V_{OC}. Figure 4.9(a), summarizes on the simulated V_{OC} as a function of the lifetime. When improving the bulk lifetime from 2.5 ms to 9.5 ms, the only meagre benefit on V_{OC} and with saturation at about 694 mV is shown, because the limiting factor is dominated by the surface recombination loss. The selective FSF doping underneath the Ag contacts would reduce $J_{0, met (Ag)}$. Increasing the thickness and reducing the defect (SRH recombination) of the Al-p^+ region minimises $J_{0, met (Al)}$, the former can be achieved by increasing the amount of Si additives in the Al paste and the

latter can be reached by an elevated content of boron additives in the Al paste[45]. Figure 4.9(b), summarises the roadmap for reaching 700 mV V_{OC}. The most reasonable V_{OC} increments are from optimizing the recombination of each part and that could be reached in the short term.
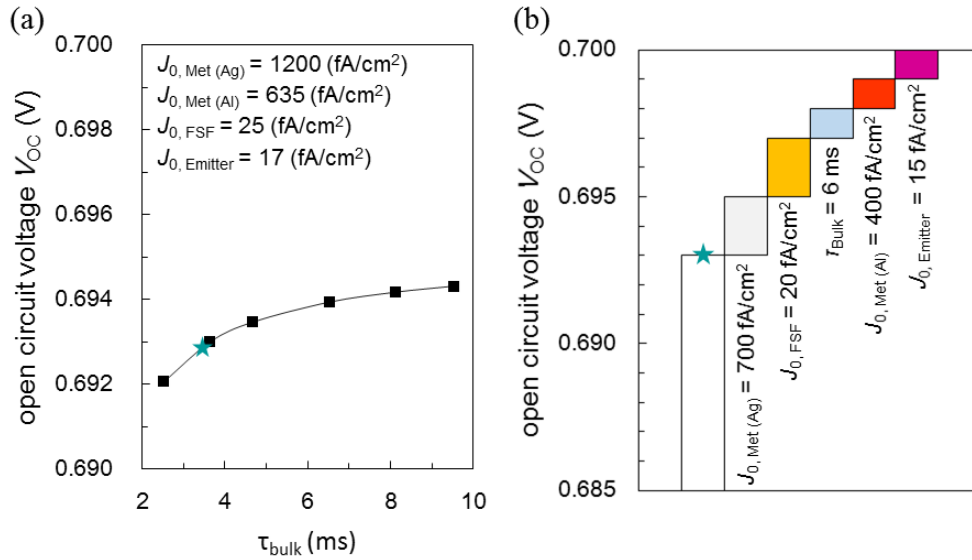
FIGURE 4.9. (a) Open-circuit voltage potential of *n*-PERT-RJ solar cells as a function of recombination parameters at the bulk region (τ_{bulk}). (b) Roadmap for reaching 700 mV V_{OC}.

4.3.7 Roadmap toward 23% cell efficiency

Through this simulation model, not only the V_{OC} can be estimated but also the efficiency potential of our *n*-PERT-RJ solar cells. Fig. 4.10 simulates the roadmap for reaching 23% cell efficiency. When combining this roadmap with the FELA results in the previous section (Fig. 4.8), the conclusions are as follows:
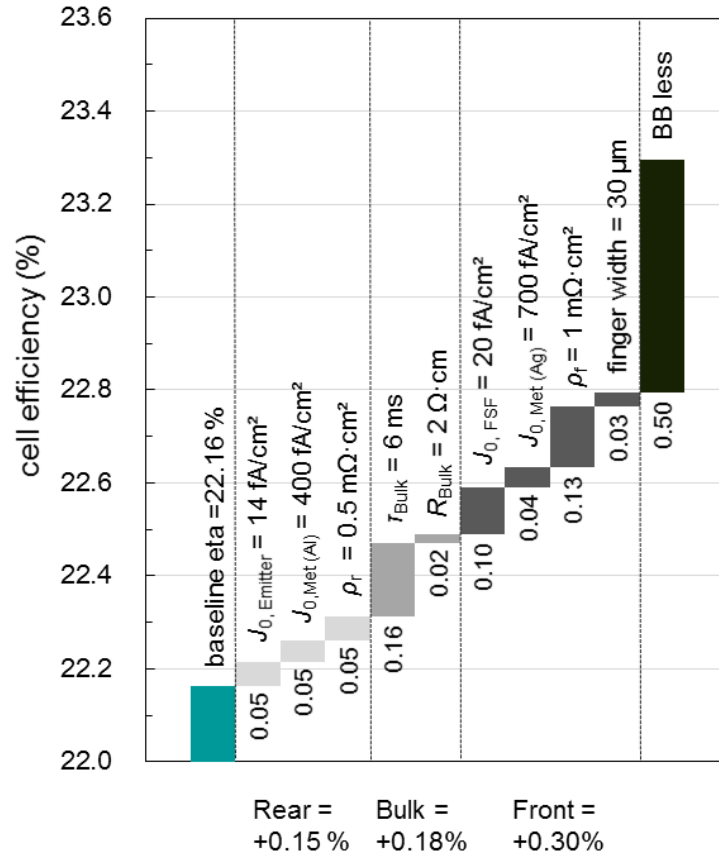
FIGURE 4.10. The *n*-PERT-RJ cell efficiency roadmap for reaching 23%.

1) For the front side of the *n*-PERT-RJ solar cells in this chapter, the bottleneck that limits the efficiency now is the relative high recombination at the FSF surface. If the $J_{0,\,FSF} \leq 20$ fA/cm², either by adjusting the phosphorus doping profile or by improving the passivation quality, the cell efficiency is directly improved by 0.1%. On the other hand, if the $J_{0,\,Met\,(Ag)} \leq 700$ fA/cm², meanwhile the ρ_f can be as low as 1 mΩ·cm², then this will be translated to a 0.17% cell efficiency gain.

2) Using *n*-type wafers with a reduced bulk resistivity will help minimize the resistive losses and with a higher bulk lifetime will help increase the collection efficiency, and improve the pseudo FF (due to less SRH recombination). As per Fig. 4.8, the bulk related losses are the dominant losses. When the bulk resistivity (ρ_b) can be reduced to 2 Ω·cm together with a bulk lifetime (τ_{bulk}) improved to 6 ms, then roughly a 0.2% cell efficiency gain is feasible.

3) For the rear side, the application of the Al point contacts which effectively minimizes the recombination by reducing the total rear contact area proportion to only 1% of the wafer area. The rear contact pattern design had already been optimized. The next possible improvement possible is towards the reduction of the $J_{0, \text{Met (Al)}}$ by increasing the thickness or reducing the defect density in the Al-p^+ region. The in-situ grown BSG excellently passivates the rear emitter surface. Continuous improvements on the rear side -no matter at contact or passivated surface- are always positive to cell performance but is not the primary concern. Even with a reduction to 400 fA/cm² $J_{0, \text{Met (Al)}}$ and 14 fA/cm² $J_{0, \text{Emitter}}$, the cell efficiency increases only 0.1%.

Summing up all the improvements discussed above, the potential n-PERT-RJ cell efficiency can be enhanced towards 22.79% and beyond 700 mV V_{OC} (details are shown Table 4.6) with a five-busbar (5BB) metal pattern design.

TABLE 4.6. Potential 5BB n-PERT-RJ simulated cell performance by Quokka3.

	J_{SC} (mA/cm²)	V_{OC} (mV)	FF (%)	Eta (%)
Simulated	40.18	700.9	80.95	22.79

With advanced measurement system, Grid$^{\text{TOUCH}}$ [115]- developed by PASAN to characterize busbar-less cells, higher efficiency gains from the reduced shadowing by the non-printed busbars can be demonstrated. Several measurements are performed with a decreasing number of wires and then Jsc is extrapolated to 0 wires (no wire shading). Additionally, the 35 conducting wires highly reduces the carrier transportation distance in the front finger. This drastically minimizes the resistive loss, and therefore a higher FF will be measured. Benefiting from these two points, the n-PERT-RJ solar cells with busbar-less design can have at least 0.5% cell efficiency gain and make the potential cell efficiency beyond 23% (see Fig. 4.10). Using the same solar cell precursors shown in Table 4.3, and with only modification from five to zero busbar and measured with the Grid$^{\text{TOUCH}}$ system, peak cell efficiency of 22.98% is achieved.

4.4   Conclusion

In this chapter, large area screen-printed n-PERT-RJ solar cells were investigated. The first part of this chapter demonstrates the V_{OC} optimization to reach 693 mV with industrial mass production tools. The improvement of V_{OC} mainly comes from:

1) A shallower FSF doping profile, which makes a better blue response and lower Auger recombination.

2) The narrower and Ag dash contacts on the front side. The firing through Ag contact area fraction reduced from 3% to 1% of the wafer area, resulting in an area-weighted $J_{0, \text{Met (Ag)}}$ reduction of more than 65% to 12 fA/cm².

3) Screen-printed Al point contacts applied on the rear side. After optimizing the amount of Si additives in the Al paste, the $J_{0, \text{Met (Al)}}$ can be reduced to 635 mA/cm² and the effective Al contact area fraction is reduced to around 1% of the wafer area. This makes the area-weighted $J_{0, \text{Met (Al)}}$ reduce more than 80% to 8.3 fA/cm².

Summing up with area-weighted $J_{0, \text{bulk}}$ and $J_{0, \text{Emitter}}$, the $J_{0, \text{Total}}$ equals to 77.8 fA/cm² which translates to a V_{OC} of 693 mV.

The second part of this chapter describes the detailed loss analysis and predicts the potential performance yield for the n-PERT-RJ solar cells based on Quokka3 simulation. A solar cell model is established first for the simulation with the input parameters from the detailed characterization of the experimental champion cell. The simulated electrical properties match well the measurements. The efficiency losses from different mechanisms are shown in the FELA, the recombination loss in the FSF and resistive loss in the bulk are the largest two of all loss mechanisms which should be optimized in a higher priority for the most significant gains. The possibility to reach 700 mV V_{OC} with diffused surfaces and all screen-printed metallization is also demonstrated. In the completion of this forecast simulation, the optimized cell efficiency can reach values beyond 23% is shown.

Chapter 5: Industrial Screen-Printed *n*-PERT-RJ Solar Cells: High Performance, Low Cost, Simple Process and Long-Term Stability

5.1   Introduction

The studies on a large-area *n*-type passivated emitter and rear totally diffused rear junction (*n*-PERT-RJ) solar cell structure are continue. The over 690 mV stable open-circuit voltage (V_{OC}) is worth to be highlighted. Stable high voltages in solar cells can be transferred directly to modules without any losses and are becoming increasingly important. In recent research and develop filed of photovoltaics (PV)[145–148], researchers consider the passivating contact technology as a promising way to achieve high V_{OC}. In this chapter, how to achieve high V_{OC} and stable high efficiency near 23% by merely using approved industrial mass production tools and without laser doping process will be demonstrated. Also how the solar cell performance affected by different *n*-type wafer properties are also shown. The cost of ownership (COO) of our *n*-PERT-RJ solar cells is in the range of the *p*-PERC solar cells. The light and elevated temperature induced degradation (LeTID) test will also be performed for showing the long-term stability of the *n*-PERT-RJ solar cell.

5.2   Experimental

The experimental steps of manufacturing the *n*-PERT-RJ solar cells are identical to Section 2.2.

5.3   Results and discussion

5.3.1   Low area-weighted $J_{o, \text{Met (Ag)}}$ with homogeneous FSF

Metal-induced recombination under the Ag contact region is considered as the major efficiency loss mechanism in most silicon solar cells today. In order to minimize this recombination loss, the selective doping structure performed by the laser is now a common process in the industry. These selective doping technologies are designed for making heavier doping underneath the metallized region and lightly doping elsewhere. It provides the benefits of having both, a low specific front contact resistivity (ρ_f) and better shielding of the Ag contacts. In this section, more detailed investigations on the two major undesirable side

effects induced by the laser doping process mentioned previously in Section 4.3.2 will be discussed:

1) Owing to the alignment margins for Ag finger printing and the native laser spot size, the laser doping area is around 150 µm wide which is three to four times wider than the finger width. After deducting the Ag contact regions, the residual regions are passivated but possess a higher recombination current density ($J_{0,\text{ s-FSF}}$) than the other passivated regions without laser doping (Fig. 5.1(a)). Take our FSF as an example, the surface concentration is around 1.7×10^{19} cm^{-3}, the $J_{0,\text{ Met}}$ of the commercial firing through Ag paste printed on this texturized FSF surface is around 1200 fA/cm^2 [127]. By applying the laser doping process, if the $J_{0,\text{ Met (Ag)}}$ can be reduced to 800 fA/cm^2 [116], the area-weighted $J_{0,\text{ Met (Ag)}}$ can be reduced to 8 fA/cm^2, but in accompany with the generation of 3.6 fA/cm^2 $J_{0,\text{ s-FSF}}$ only 2 mV gain on the V_{OC} will be realized for the solar cell device. Even for a more ambitious scenario where $J_{0,\text{ Met}}$ and $J_{0,\text{ s-FSF}}$ can be more progressively reduced to 500 fA/cm^2 and to 70 fA/cm^2 [134] respectively, there would be just a gain of 5 mV on the V_{OC} (see Table 5.1) with our *n*-PERT-RJ solar cell structure.

TABLE 5.1. Scenarios for reaching high V_{OC} and low front contact resistivity of *n*-PERT-RJ solar cells.

	lines (BKM)	lines + s-FSF		dashes	dashes + s-FSF
$J_{0,\text{ Met (Ag)}}$ / $J_{0,\text{ FSF}}$ / $J_{0,\text{ s-FSF}}$ (fA/cm^2)	1200/25/-	800[116]/25/60[116]	500[134]/25/70[134]	1200/25/-	500[134]/25/70[134]
Area-weighted $J_{0,\text{ Met (Ag)}}$ (fA/cm^2)	24.0	16.0	10.0	12.0	5.0
Area-weighted $J_{0,\text{ FSF}}$ (fA/cm^2)	24.5	23.0	23.0	24.8	24.0
Area-weighted $J_{0,\text{ s-FSF}}$ (fA/cm^2)	-	3.6	4.2	-	3.0
$J_{0,\text{ Total}}$ (fA/cm^2)	89.4	83.5	78.1	77.8	72.9
V_{OC} (mV)	688	690	693	693	694
ρ_{f} (mΩ·cm^2)	2	2[116]	2[134]	2	2

FIGURE 5.1. (a) Schematic of n-PERT-RJ solar cell's front side and the location where every kind of recombination current occur. (b) The process steps comparison between the homogeneous and the selective FSF, the red boxes are the additional steps.

2) For the 5 mV V_{OC} gain, the laser doping process causes additional laser doping and thermal oxide passivation steps (the red boxes in Fig. 5.1(b)) after PSG removal for lowering the $J_{0, \text{Met}}$, $J_{0, \text{FSF}}$ and $J_{0, \text{s-FSF}}$, increasing not only the costs but also the complexity of the process.

The strategy in this section to improve the impact of $J_{0, \text{Met (Ag)}}$ is to minimize the metallized area reaction by changing to fine-line printing and applying the dash contact concept. The finger width was reduced from 60 to 40 µm, which reduces the metallized fraction to 2% of the wafer area. The design of the metal grid consists of first printed dashes (300 µm length) with the firing through Ag paste to form the contact and afterwards the metallization with a second layer for connecting these dash contacts by a non-firing through Ag paste. A top view image of the modification of the metal grid design taken by LSM is shown in Fig. 5.2. In this way, not only the area-weighted $J_{0, \text{Met (Ag)}}$ is successfully reduced but also the cost can be benefited from the 30% decreasing laydown of the silver paste.
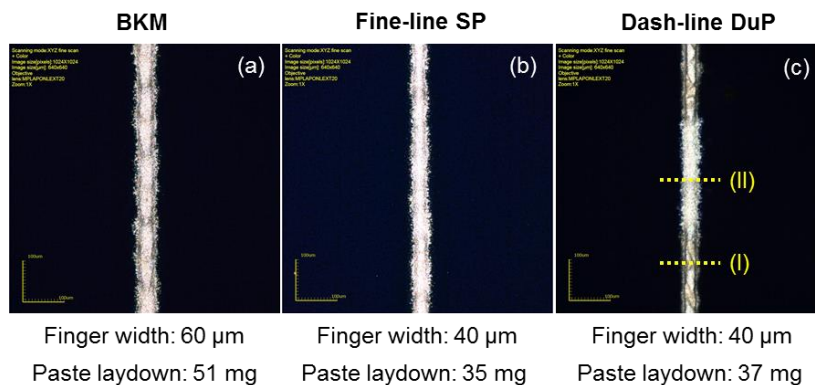
FIGURE 5.2. LSM top view image of the screen printed Ag finger: (a) finger width of 60 µm; (b) fine-line finger width of 40 µm; (c) the width of firing through finger (I) is 40 µm and the width of non-firing through finger (II) is 42 µm. SP: single printing; DuP: dual printing.

Because the FSF is in a parallel circuit with the n-bulk, take our cell devices as an example: the sheet resistance (R_{sh}) of the phosphorous doped n^+ layer is 180 Ω/sq on a p-type wafer, but when it's processing on an n-type wafer with a bulk resistivity 3-4 $\Omega \cdot$cm, the effective R_{sh} will become only 100 Ω/sq. As a consequence, the optimized finger number (or pitch) is less (or larger) than e.g. for a p-PERC whose emitter would have the same doping profile as our FSF. For this reason, n-PERT-RJ solar cells manage on less front Ag consumption, and a reduced front side metallized fraction (down to 1% in our case). The benefits of a selective doping structure are then insignificant and result in only 1 mV gain (the comparison between the last two columns of Table 5.1). The only potential benefit can be acquired from the application of selective doping is that the Ag contacts can have a lower ρ_f. If the ρ_f can be reduced from 2 to 1 m$\Omega \cdot$cm^2, there will be an improvement of 0.4% in FF and 0.1% in efficiency respectively (see Fig. 5.3).
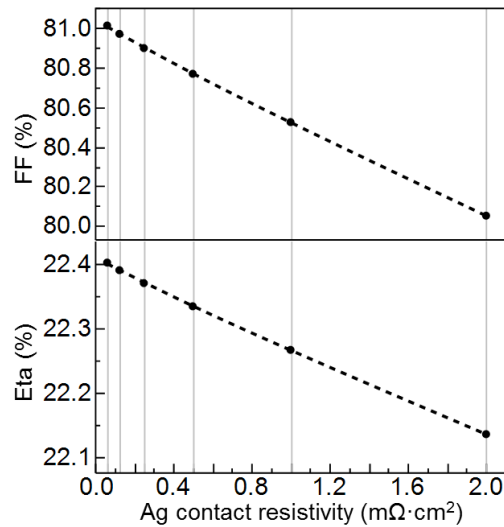
FIGURE 5.3. FF and efficiency loss of the n-PERT-RJ solar cells with varying the front side Ag contact resistivity values. The results are simulated by Quokka3.

5.3.2 The n-bulk properties

In this section, the dependence of the n-PERT-RJ solar cell's performance on the n-bulk characteristics will be discussed. The simulation results are generated by Quokka3. First, a 3.5 ms lifetime n-type wafer with varying bulk resistivities (R_{bulk}) ranging from 0.5 to 13 $\Omega \cdot$cm (see Fig. 5.4) is considered. When the R_{bulk} is higher than 3 $\Omega \cdot$cm, the solar cell performance will be stable, and because of the trade-off between J_{SC} and FF, the solar cell efficiency can

even keep on the same level for R_{bulk} down to 1 $\Omega\cdot$cm. By matching the whole resistive range of a commercial n-type ingot[149], the supply of appropriate material is no longer a critical issue for bringing n-PERT-RJ solar cells towards mass production. Second, the bulk lifetime (τ_{bulk}) is of course still rather important for the rear junction solar cells. The 2.8 $\Omega\cdot$cm R_{bulk} is set for the wafers with different τ_{bulk} ranging from 250 µs to 6 ms. In Fig. 5.5, 2 ms is the lowest τ_{bulk} can be applied without huge degradation on solar cell performance. In today's PV wafer market, the price of the n-type wafer (0.44 USD/wafer @ Apr. 2019[150]) is close to p-type (0.41 USD/wafer @ Apr. 2019[150]). Based on the claim of the wafer manufacture[149], the wafer price could be reduced by 0.015 USD for every 10 µm wafer thickness reduction. If the n-type wafer with a thickness reduction of 20 µm can be applied, then the cost of the n- and p-type wafer will be identical. Our wafer after the complete solar cell process the thickness is around 165 µm, the solar cell performance with different thicknesses are simulated, and the results are shown in Fig. 5.6. When the thickness is decreased by 20 µm to 145 µm, the efficiency drop is less than 0.05%. Beyond this wafer thinning, the J_{SC} starts to drop more strongly because of the reduction in irradiation absorption. In this case, the J_{SC} loss is higher than the V_{OC} and FF gain, so the efficiency starts to drop.
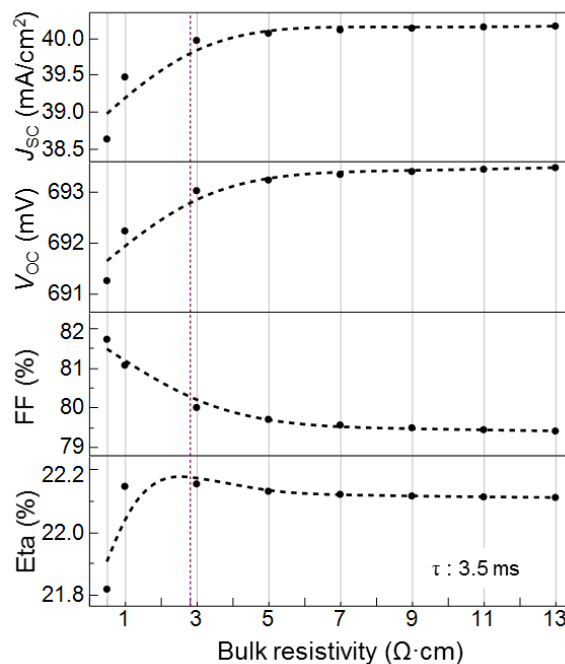
FIGURE 5.4. The n-PERT-RJ solar cells with different bulk resistivities. Black dashed lines serve as a guide to the eye, purple one indicates the experimental data.
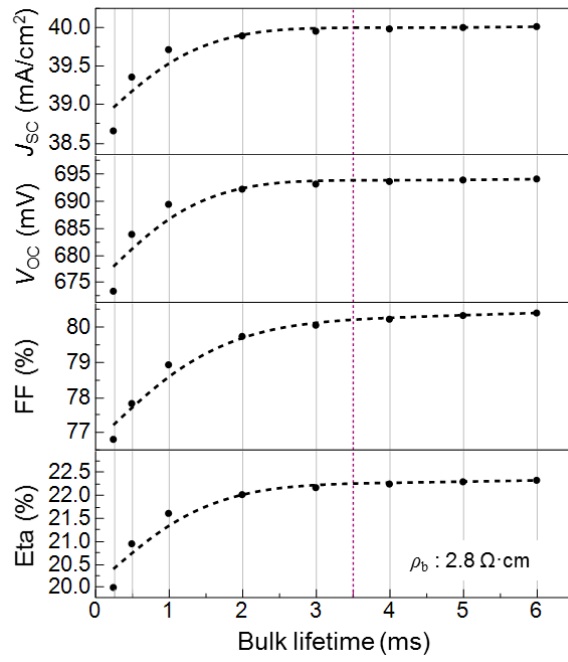
FIGURE 5.5. The *n*-PERT-RJ solar cells with different bulk lifetimes. Black dashed lines serve as a guide to the eye, purple one indicates the experimental data.
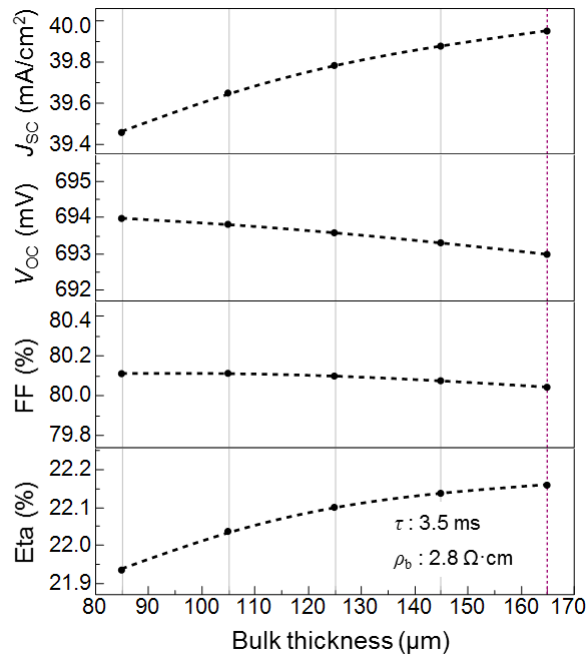
FIGURE 5.6. The *n*-PERT-RJ solar cells with different bulk thicknesses. Black dashed lines serve as a guide to the eye, purple one indicates the experimental data.

5.3.3 Approaching 695 mV V_{OC} without passivating contacts

High V_{OC} is not only beneficial for the cell efficiency measured under standard test condition (STC) but also contribute to better module-level performance, especially for a PV plant in desert regions, where the modules are exposed to higher temperatures. High-voltage solar cells have a lower temperature coefficient and thus produce a higher energy yield for such PV systems. In addition, V_{OC} is inversely proportional to the natural logarithmic value of $J_{0, \text{Total}}$; hence, lowering the $J_{0, \text{Total}}$, is the key to obtain high V_{OC}. Figure 5.7(a) depicts the $J_{0, \text{Total}}$ components of the *n*-PERT-RJ solar cell and its corresponding engender position. The $J_{0, \text{Total}}$ is built up of $J_{0, \text{Met (Ag)}}$, $J_{0, \text{FSF}}$, $J_{0, \text{Bulk}}$, $J_{0, \text{Emitter}}$ and $J_{0, \text{Met (Al)}}$. The commercial Ag paste is printed on textured FSF having a surface concentration of 1×10^{19} cm^{-3} and its corresponding $J_{0 \text{ Met (Ag)}}$ is 1200 fA/cm^2 [127]. As described in the previous section, after applying a narrower front side finger width and modifying the grid pattern, the "effective" (which means: metallized with firing through Ag paste) contact fraction is decreased to 1% of the wafer area. The area-weighted $J_{0, \text{Met (Ag)}}$ was then reduced to 14 fA/cm^2. The amount of Si-add is gradually increased in the Al paste for the purpose of not only well forming the point contact but also thickening the underlying Al-doped p^+ region. Thicker Al-doped p^+ Si layer provides a better shielding effect, hence metallization with the high wt% Si-add Al paste decreases the $J_{0, \text{Met (Al)}}$ to 635 fA/cm^2.

Furthermore, the effective suppression of out-diffusion of bulk-Si reduces the total contact area fraction to only 1%, resulting in 8 fA/cm^2 area-weighted $J_{0, \text{Met (Al)}}$. Combining the optimized $J_{0, \text{Met (Ag and Al)}}$ with the state-of-art $J_{0, \text{Emitter}}$ (20 fA/cm^2 at flat surface with $R_{sh} \approx 200$ Ω/sq), $J_{0, \text{Bulk}}$ (16 fA/cm^2 at commercial *n*-type Cz wafers with 4 Ω·cm), and $J_{0, \text{FSF}}$ (25 fA/cm^2 on textured surface with $R_{sh} \approx 180$ Ω/sq) the area-weighted $J_{0, \text{Total}}$ is reduced to 78 fA/cm^2 and the V_{OC} can be boosted up to 693 mV . It's worth to mention that the recombination under metal contact (sum of $J_{0, \text{Met (Ag)}}$ and $J_{0, \text{Met (Al)}}$) is reduced to less than a third of the $J_{0, \text{Total}}$ (Fig. 5.7(b)), which means that metallization induced recombination isn't the bottleneck.

(a)

(b)
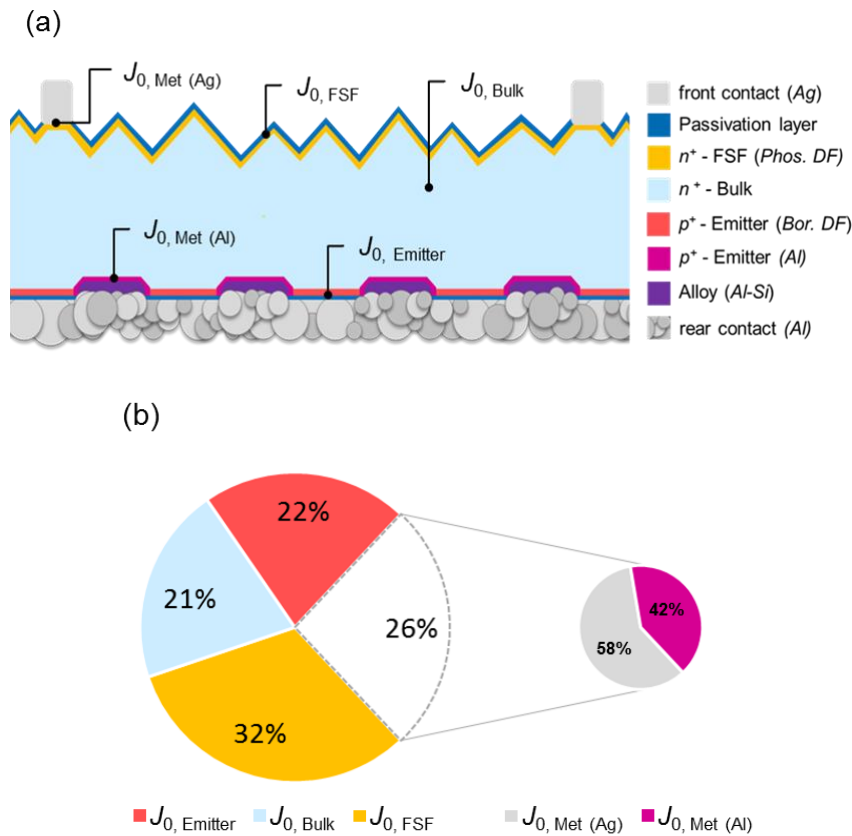
FIGURE 5.7. (a) The schematic cross-sectional structure of *n*-PERT-RJ solar cells and the location where every kind of recombination current occur. (b) Total recombination current density ($J_{0, \text{Total}}$) composition of a 693mV V_{OC} *n*-PERT-RJ solar cell.

Passivating contact technology is a recent solution to achieve higher V_{OC} and is also considered an upgrade to *n*-PERT solar cells. Based on this technology, lots of cell concepts are launched (see Table 5.4.), e.g., Tunnel Oxide Passivated Contact (TOPCon)[145] cells from Fraunhofer ISE, Passivated Emitter and Rear Polysilicon (PERPoly)[146] cells from ECN, Poly-Si on Oxide (POLO)[147] cell from ISFH and monofacial deposition of poly-Si layer (monoPoly™) from SERIS. In this thesis, with the 5 busbar front grid pattern design, the champion *n*-PERT-RJ solar cell has 22.2% in cell efficiency with 693 mV in V_{OC} (see Table 4.3 in Chapter 4). Just like many researchers did for the purpose of showing the potential solar cell performance, the grid pattern design is also changed to a busbar-less layout and measured with a GridTOUCH[115] system. Efficiency gains from the reduced shadowing and line resistive loss, push the solar cell performance to 22.9%. With the use of established mass production process tools, our *n*-PERT-RJ solar cells show the same (or even higher) level of V_{OC} compared to the mentioned advanced passivating contact technology (see Table 5.2).

TABLE 5.2. The latest champion *n*-PERT solar cell performance.

1st author affiliation	V_{OC} (mV)	J_{SC} (mA/cm²)	FF (%)	Eta (%)	Junction position	Front/Rear contact	h^+ collector	e^- collector
ISFH[151]	714	38.5	81.1	22.3	rear	0BB TCO+SP-Ag	p^+ poly	n^+ poly
ISC-Konstanz*	693	40.7	81.0	22.9	rear	0BB SP-Ag/SP-Al	BBr$_3$ DF	POCl$_3$ DF
imec[116]	683	41.1	82.0	23.0	rear	0BB SP-Ag/SP-Al	BBr$_3$ DF	s-POCl$_3$ DF
Georgia Tech[139]	672	38.9	79.9	20.9	rear	5BB Both sides SP-Ag	p^+ poly	s-Phos-IMP
SERIS[148]	696	40.5	80.9	22.8	front	0BB SP-AgAl/SP-Ag	BBr$_3$ DF	n^+ poly
Jolywood[152]	688	39.9	81.4	22.4	front	12BB Both sides SP-Ag	s-BBr$_3$ DF	n^+ poly
ECN[153]	676	39.7	80.0	21.5	front	5BB SP-AgAl/SP-Ag	BBr$_3$ DF	n^+ poly

*in-house measurement with GridTOUCH system

5.3.4 Cost of Ownership (COO) and Stability

In this chapter, the *n*-PERT-RJ solar cells with high V_{OC} and cell efficiency are introduced, which manufactured by very simple "close to standard" processes of *p*-PERC. The calculated total cost of ownership (COO) (under a consumption of the wafer price mentioned in the previous section) for a 22.2% efficient monofacial *n*-PERT-RJ cell is 13.1 US¢/Wp (5.0 US¢/Wp w/o wafer) and for a 22.0% efficient monofacial *p*-PERC cell is 13.4 US¢/Wp (5.4 US¢/Wp w/o wafer), respectively (see Fig. 5.8). Most of the cost difference is because the wafer price of the *n*-type is still higher than the *p*-type wafer, but as mentioned in the previous section, this can be compensated by reducing the wafer thickness. The difference in the process tools compared to the *p*-PERC process is only an additional BBr$_3$ diffusion (with in-situ BSG passivation), which replaces the PECVD-AlO$_x$ or ALD-Al$_2$O$_3$ rear side passivation of the *p*-PERC technology. The shallow boron doping rear emitter reduced the spread resistance in the bulk, highly reducing the rear contact ratio to around 1% of the wafer area, thus getting a higher V_{OC}.
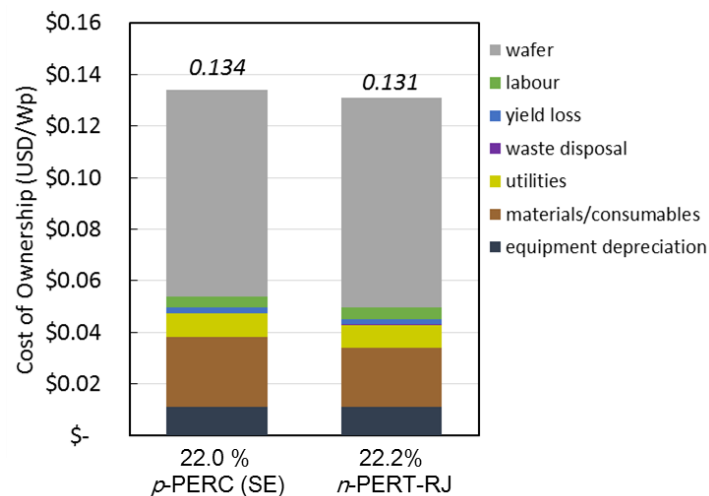
FIGURE 5.8. Cost of ownership (COO) comparison between the 22.0% efficient *p*-PERC and 22.2% efficient *n*-PERT-RJ solar cells.

The Light and elevated Temperature Induced Degradation (LeTID) was first found in *p*-type *mc*-Si PERC solar cells and also happened in *mono*-Si PERC. This degradation is due to too much hydrogen content in the cell devices. The fresh SiN$_x$ on the rear side of the *p*-PERC solar cells is considered as an additional hydrogen supplier, and when the hydrogen drive-in to the bulk Si during the firing process the degradation will occur. The LeTID test is also performed on our cells and observed no obvious degradation. These results are shown in Fig. 5.9.
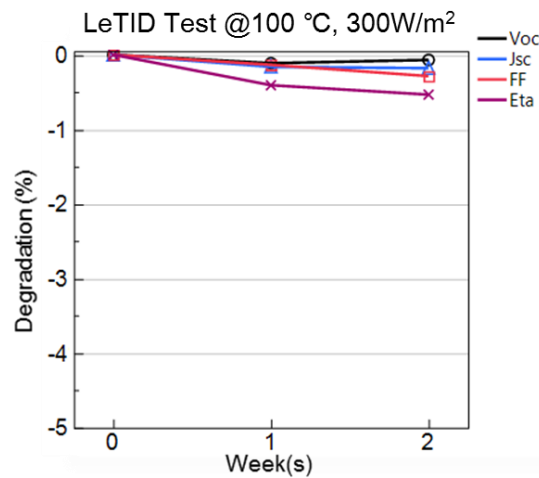
FIGURE 5.9. The LeTID test of *n*-PERT-RJ solar cells. The test condition is under an open-circuit condition with a temperature of 100 °C and illuminations at 300 W/m².

5.4 Conclusion

In this chapter, both sides screen-printed *n*-PERT-RJ solar cells with 693 mV and an averaged solar cell efficiency beyond 22% is introduced. First, why the selective doping FSF structure has no benefit on our solar cells is explained, only increasing the complexity and the cost of the process. Second, the impact of different *n*-bulk parameters on *n*-PERT-RJ solar cell performance is simulated. It was found that for R_{bulk} between 1-13 $\Omega \cdot$cm can keep a stable solar cell efficiency with our process. Material quality for our rear junction solar cells, regarding τ_{bulk}, should be higher than 2 ms preventing severe performance drops. Reducing the bulk thickness to around 145 µm not only maintain the cell performance but can also compensate for the higher cost of the *n*-type wafers. The last parts reveal *n*-PERT-RJ solar cells have the same performance level as the advanced passivating contact solar cells today. But only standard mass-production tools are used and the COO is comparable to *p*-PERC solar cells with

the selective emitter (SE). There is nearly no LeTID degradation, which makes these n-PERT-RJ solar cells have high performance, low cost, simple process, and long-term stability.

Chapter 6: Comparison of PVD and Screen-Printed Al Point Contact on the Rear Side of *n*-PERT-RJ Solar Cells

6.1 Introduction

Until now, the point contact concept was mostly metallized by physical vapor deposition (PVD). For the solar cell performance, the major benefits of applying PVD-Al point contact are on open-circuit voltage (V_{OC}) and fill factor (FF). Higher V_{OC} comes from the low contact area fraction and effectively reduces the area-weighted metal-induced recombination current density ($J_{0, Met}$). A better FF is due to less series resistance (R_S) contribution from the Al layer sheet resistance (R_{sheet}) and the specific contact resistivity (ρ_c). That's why most of the advanced or high-performance cell concepts of laboratory-scale choose PVD-Al as the rear side metallization[47,62]. In addition to the benefits on the solar cell performance, the thinner PVD-Al layer (thickness of few microns) reduces the stress induced by the fully covered rear Al electrode, thus extenuating the bowing phenomena[40] of the solar cells. Less bowing can reduce breakage that occurs during module interconnection. PVD-Al theoretically forms an Ohmic contact on the Si surface. When the doping concentration of the contact surface is $N_D = 1\times10^{-19}$ cm^{-3}, the ρ_c is about 10^{-1} mΩ·cm^2 [154,155]. In this chapter, the discussion is divided into three parts: (1) mechanism of dot-shaped LCO by applying the indirect type laser; (2) microstructure and electrical properties compared for PVD-Al and screen printed (SP)-Al point contact; (3) characterization and simulation of the *n*-PERT-RJ solar cell with PVD-Al and SP-Al rear point contact.

6.2 Experimental

Fig. 6.1 shows the flow of the *n*-PERT-RJ solar cell process with PVD-Al and SP-Al rear point contact. The upper portion of the figure surrounded by the dashed line shows the route for fabricating the solar cell precursors, the steps and sequence being the same as shown in Section 2.2. The only difference is on sheet resistance (R_{sheet}) of the front surface field (FSF) and the rear emitter of the devices reported in this chapter is 150 Ω/sq and 200 Ω/sq, respectively. After the precursors are formed, the sequence of the following processes (the

metallization and the LCO will be divided into two different scenarios. For the PVD-Al layer, which melting point is 660 °C, the thermal budget of the front side screen-printed Ag contact formation (> 700 °C) is too high. Another thing that had to be noted is the fact that if the dot-shaped LCOs are performed prior to the high-temperature sintering step, there will grow an oxide layer on the LCOs-Si surface which will lead to a high contact resistance (ρ_c). So the process sequence of the metallization is fixed and the LCO for the PVD-Al group which are shown in the left part of Fig. 6.1(after the purple arrow). Both groups are ablated with the same laser, the laser is with 523 nm wavelength and 250 femtoseconds (fs) pulse duration. The LCO pitch between the dots is 450 µm. For the SP-Al group, the contact is printed with high wt% Si-add Al paste.
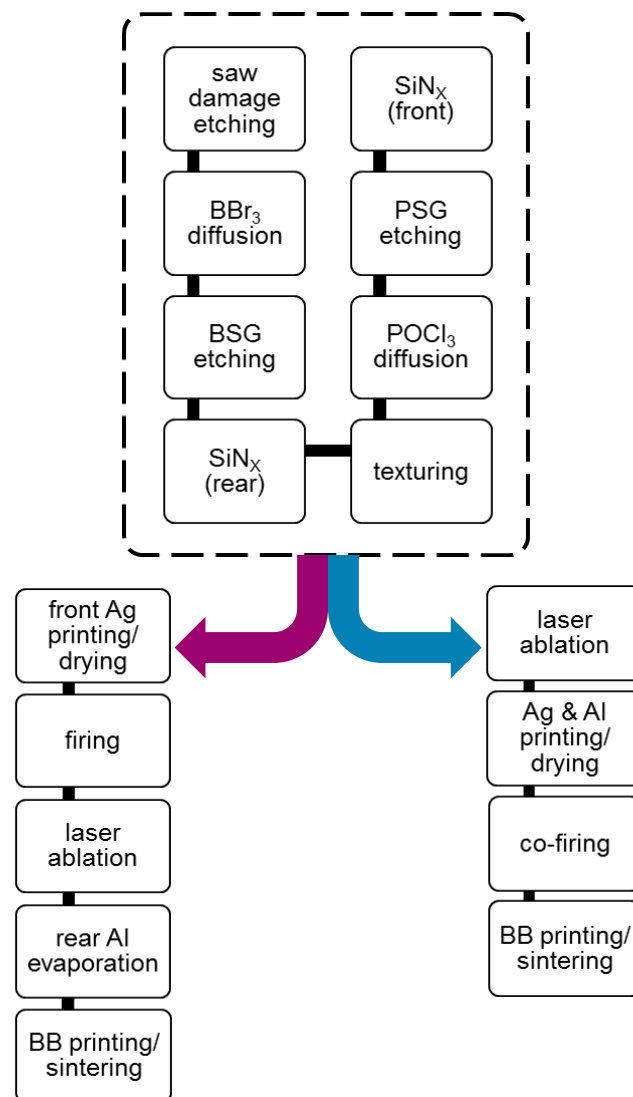
Figure 6.1. The process flow of the *n*-PERT-RJ solar cells with PVD-Al (left side after the purple arrow) and SP-Al (right side after the blue arrow) rear point contact.

The machine used to process the PVD-Al layer is a thermal evaporation system developed by SINGULUS[156]. The construction has specific characteristics compared to the reference system[71,157]: the deposition is made in a diffused way and the vacuum chamber wall has a specific chemical coating to prevent the Al vapor condensation on it. The setup is well suited to deposit metal layers of uniform thickness. Fig. 6.2(a) is a cross-sectional image of the chamber. In the top-down deposition geometry which is shown in Fig. 6.2(b), the wafer is placed at the bottom transport table. The ceramic made evaporation boat will be heated up over 1200 °C to emit the Al vapor with approximately 10^{-2} mbar towards the top cover of the chamber. The particles are reflected by the pre-coated anti-condense agent and are then uniformly distributed to the target wafer substrate. When the gas state Al particles contact the surface of the wafer, thermal equilibrium begins and the particles will cool down, return to solid-state and precipitate at the wafer. The substrate is preheated to about 400 °C compared to an in-line high-speed thermal evaporation system[71], which can provide Al particles with more energy to form a denser arrangement.
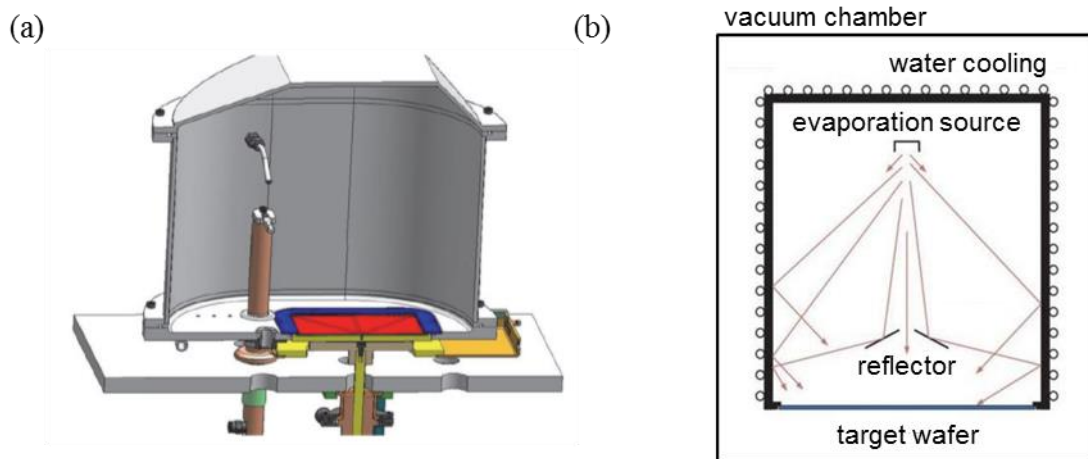
Figure 6.2. The thermal evaporation type PVD system: (a) cross-sectional image of the top-down deposition system; (b) schematic of the thermal evaporation cell.

Symmetric boron-doped (the diffusion profile is the same as used for the emitter of the solar cell device) and passivated test structures were prepared. After the point contact was formed, the Al will be removed by high concentration hydrochloric acid (HCl), the test structures were then subjected to QSSPC[39] measurement for the $J_{0, Met}$ extraction. The surface doping concentration profiles were measured by electrochemical capacitance-voltage[128] (ECV) method. The

spectral response (the reflectance and internal quantum efficiency (IQE)) data was determined between the wavelength of 300 and 1200 nm, using the solar cell analysis system LOANA[87] by PV-tools. The in house cell's performance measurements were performed with an h.a.l.m. flasher system. The calibration cell was processed in a similar process sequence and was certified by Fraunhofer ISE CalLab. The Quokka3[140] simulation is performed to demonstrate the FF loss and efficiency potential of the *n*-PERT-RJ solar cells with PVD-Al rear point contact.

6.3 Results and discussion

6.3.1 The dot-shaped LCO formation

PVD-Al is a "soft" metallization with no severe reactions (e.g., Al-Si interdiffusion or recrystallization) during contact formation. The damage induced by laser ablation has no option of being eliminated totally. Conventional diode-pumped solid-state lasers (pulse duration at ns level) severely damage and change the structure of the crystalline silicon (*c*-Si) underneath[158,159]. In this thesis, an "indirect" type laser is applied to perform the dot-shaped LCO to reduce the laser ablation induced damage. Fig. 6.3 shows the mechanism of the indirect laser ablation[59].
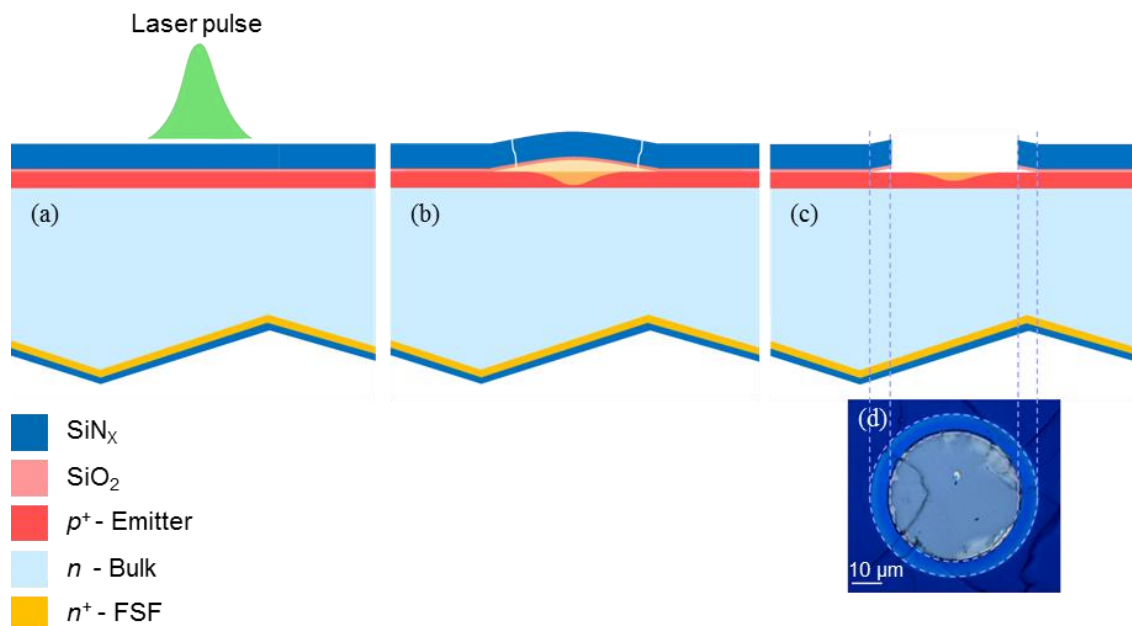
Figure 6.3. The mechanism of the "indirect" laser ablation: (a) the laser impulse with Gaussian profile is given; (b) the pulse energy is absorbed by the silicon surface and the state transfer from solid to gas. (c) The dielectric stack finally lifted up by the increasing Si vapor pressure. (d) Top view image is taken by laser scanning microscopy (LSM).

The laser radiation passes through the dielectric stack and is absorbed by the underlying Si. The laser pulse melts a thin layer of silicon which evaporates and builds up the pressure. The increased pressure eventually strips off the dielectric stack and forms a dot-shaped LCO. The dielectric layer is typically about 100 nm thick and it can be structured selectively with the help of local silicon substrate absorption of the laser energy. By applying a femtosecond (fs) laser pulse at photon energies above the Si bandgap [160,161], detachment can take place without noticeable collateral thermal damage at the ablated surface which is suitable to combine with the soft metallization.

The rear side dielectric stack[28] of our *n*-PERT-RJ solar cells is composed of 10 nm SiO_2 (n = 1.46) and 70 nm SiN_x (n = 2.03). Each spot has been irradiated by a single pulse, after irradiation, the ablated area was characterized with a LSM. In Fig. 6.3(d) the dot-shaped LCO is surrounded by a light blue region which is called "corona ring[162]". This is induced by the Gaussian laser beam profile. Only the middle part of the beam fluence is higher than the threshold energy of breakage ($\Phi_{th.\ b}$) and thus can evaporate Si adequate to cause an expansion of the dielectric film (Fig. 6.3(b)), and then the dielectric film is stripped to form a the dot-shaped LCO (Fig. 6.3(c)). If the fluence is lower than the $\Phi_{th.\ b}$, it is also absorbed by the Si but only changes the state from solid to liquid. During cooling, the liquid state Si will solidify to amorphous silicon (*a*-Si), this can be verified first by the optical properties. The diverse reflectances of *a*-Si and *c*-Si[163,164] give the corona ring region a different color and separates it from the other SiN_x capping regions (Fig. 6.3(d)). The solid-state transformation is reversible: the *a*-Si will crystallize with the thermal budget of heating up to 700 °C for 1 minute[165]. The corona ring disappears (Fig. 6.4) optically after the annealing step. In this work the annealing step is done by rapid thermal processing (RTP) furnace.
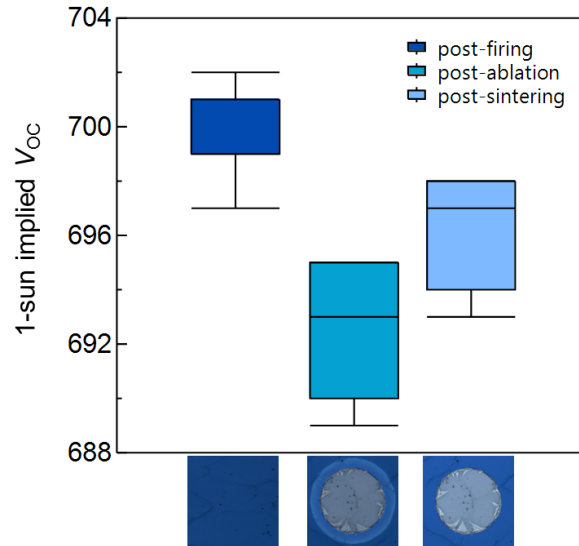
Figure 6.4. The one sun implied *Voc* values of the symmetric test structure which are measured: after firing (left); after firing and laser ablation (mid); after firing, laser ablation and sintering (right).

Other than the appearance, the implied V_{OC} had a gain of 3-5 mV on the symmetrical test structure after annealing which is also shown in Fig. 6.4. We assume that the recrystallization of the thermal induced molten *a*-Si reduces the trap density (fewer thermal defects and dangling bonds) and thus improves the passivation quality. This evaluation of the electrical properties is another sign that the corona ring is mainly caused by the appearance of *a*-Si. Although the additional annealing step helps our device quality it is difficult to merge into the process sequence of our *n*-PERT-RJ solar cells with PVD-Al rear point contacts. As a side effect the thermal treatment will result in the growth of an oxide layer on top of the LCO´s-Si surface, increasing the contact resistance. On the other hand, the annealing has no benefit for the *n*-PERT-RJ solar cells processed with SP-Al rear point contacts, because the corona ring region will be involved in formation of the contact spot (Al-Si interdiffusion reaction). After point contact is formed, the corona ring has vanished. Fig. 6.5(d) is the LSM image of SP-Al point contact top views after removal of Al, compared to Fig. 6.5(c), there is no corona ring anymore.
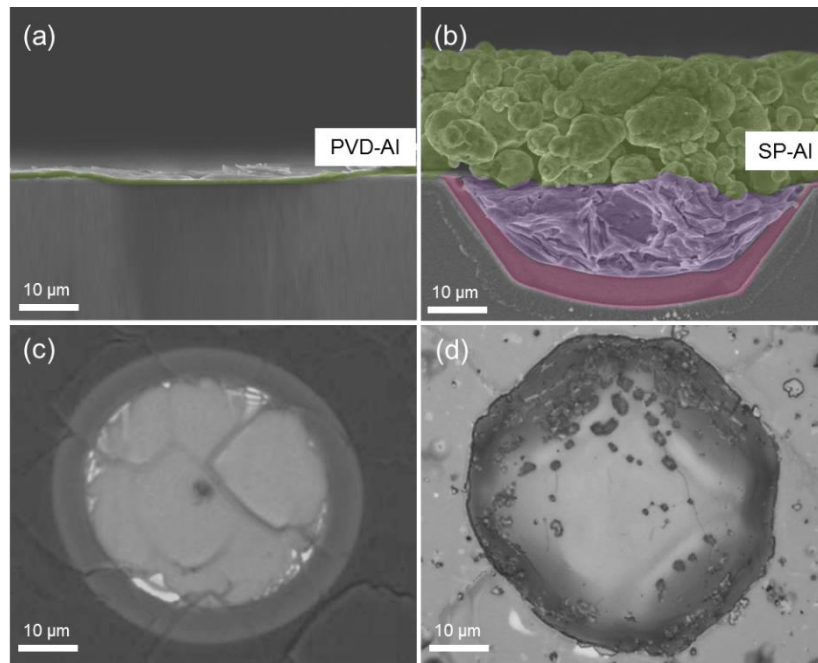
Figure 6.5. The point contacts cross-sectional SEM images: (a) PVD-Al; (b) SP-Al. The point contact top-view LSM images: (c) PVD-Al; (d) SP-Al. The green colored regions are the Al layer.

6.3.2 The Al point contact

The SP-Al point contact formation had been discussed in the previous chapters. The Al-Si alloy in the purple colored region of Fig. 6.5(b) is formed during heating up of the sintering process; the Al-doped p^+ the pink colored region of Fig. 6.5(b) is formed during the cooling down of the sintering process. Unlike the SP-Al point contact formed by a chemical reaction, the thermal evaporation type PVD-Al uses only a "soft" physical way to grow only a pure Al layer for rear contact, as shown in the green region of Fig. 6.5(a). There is no further interaction between the LCO-Si and the PVD-Al after deposition. The LSM image of the PVD-Al point contact after Al removal in Fig. 6.5(c) is identical to the post-ablation image shown in Fig. 6.3(d). Namely, the same thick Al-doped p^+ region as that after the SP-Al metallization was not formed resulting in a poor shielding under the point contact, the ablation induced or unpassivated recombination could not be "healed" by this kind of contact formation. Fig. 6.6 shows the change of the recombination current density from the passivated ($J_{0,\,\text{Pass}}$) to the metallized surface ($J_{0,\,\text{Met}}$), the difference in shielding effect between different types of Al point contact is obvious. Therefore, as shown in Table 6.1, the 1450 fA/cm^2 $J_{0,\,\text{Met}}$ (note that it includes the corona ring region) of the PVD-Al point contact is more than two times higher than the $J_{0,\,\text{Met}}$ of the SP-Al point

contact. As the total PVD-Al point contact area fraction is only 0.75% of the wafer area compared to 1.3% for the SP-Al point contact, the area-weighted $J_{0,}$ $_{Met}$ is around 3 fA/cm² higher making nearly no difference on the device level $V_{OC.}$ That is the benefit of applying PVD-Al with dot-shaped LCOs: even though the shielding under the metal contact is worse and causes high $J_{0, Met}$, this can be compensated by the very small contact area fraction. It's worth noting that, since the SP-Al point contact is feasible, the formation of low contact area fraction is no longer an exclusive feature of PVD-Al.
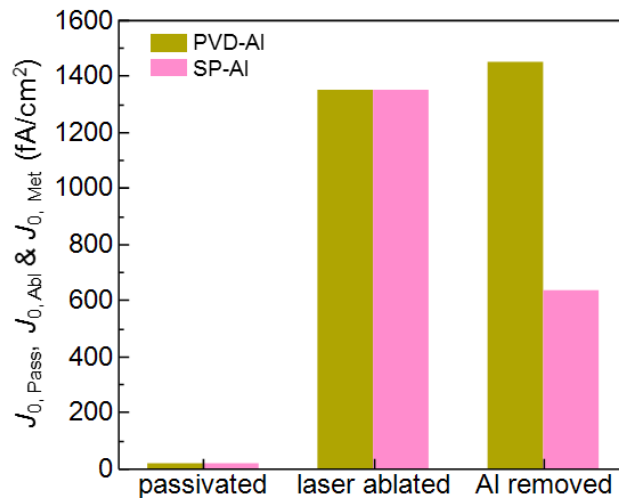
Figure 6.6. The recombination current density of passivated surface ($J_{0, Pass}$), ablated surface ($J_{0, Abl}$) and PVD-Al/SP-Al metallized surface ($J_{0, Met}$).

TABLE 6.1. The characteristic of Al point contacts and the impact on the V_{OC} of the *n*-PERT-RJ solar cells

	$J_{0, Met}$ (fA/cm²)	Contact area fraction (%)	Area-weighted $J_{0, Met}$ (fA/cm²)	V_{OC} (mV)
PVD-Al	1450	0.75	10.9	683
SP-Al	635	1.3	8.3	684

6.3.3 Characterization and simulation of the *n*-PERT-RJ solar cells with Al rear point contact

After analyzing the microstructure and the electrical properties of the PVD-Al and SP-Al point contact, for further understanding, the impact of these Al point contacts on the device level, the performance between the *n*-PERT-RJ solar cells that the rear sides metallized by PVD-Al or SP-Al will be compared. The cross-sectional structures of these solar cells are illustrated in Fig. 6.7.
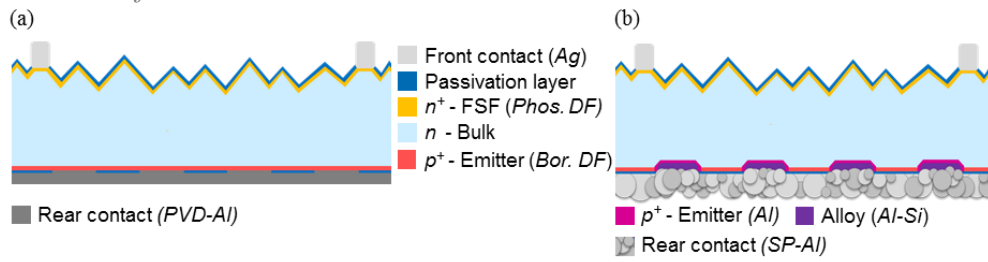
Figure 6.7. Schematic of *n*-type Passivated Emitter and Rear Totally diffused Rear Junction (*n*-PERT-RJ) solar cell the rear contact are metallized by using (a) PVD-Al; (b) SP-Al.

In this section, the comparison will mainly focus on the J_{SC} and FF. For the J_{SC} comparison, the spectral response measurement (reflectance and IQE) is performed. Actually, the PVD-Al layer doesn't bring significant benefit on the rear side reflectance. For our *n*-PERT-RJ solar cells, the role of the rear side reflector is dominated by the rear SiN_x layer as discussed in Section 3.3.2. The reflectance starts to become different from wavelength 1150 nm. In Fig. 6.8, the *n*-PERT-RJ solar cells with PVD-Al rear point contact shows a higher reflectance than those with SP-Al rear point contact, the maximum divergence appears at 1200 nm. The major reason for the difference in reflectance is the SiN_x covered ratio of the rear side. Fig. 6.9 shows the high relevance of the rear side reflectance at wavelength 1200 nm and SiN_x covered area fraction. Due to the alloying reaction during the SP-Al contact formation, the point contact diameter increases from around 35 (what is the case for the PVD-Al) to 62 μm, hence, the rear side SiN_x coverage area fraction is reduced from around 99.6% to 98.5% which induced a 4 % drop of the reflectance at 1200 nm.
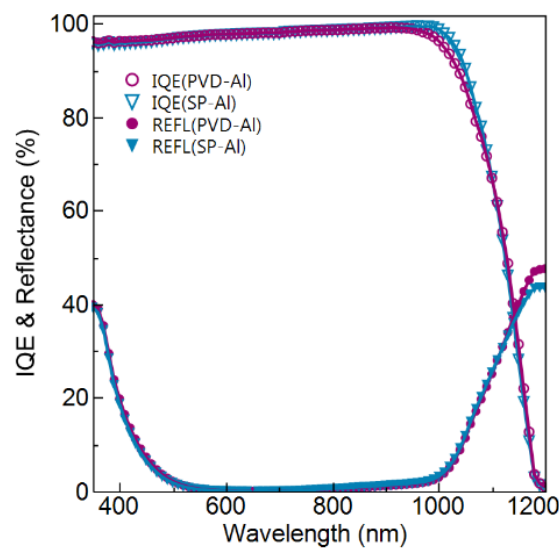
Figure 6.8. The IQE and reflectance of *n*-PERT-RJ solar cell with PVD-Al and SP-Al rear point contacts.
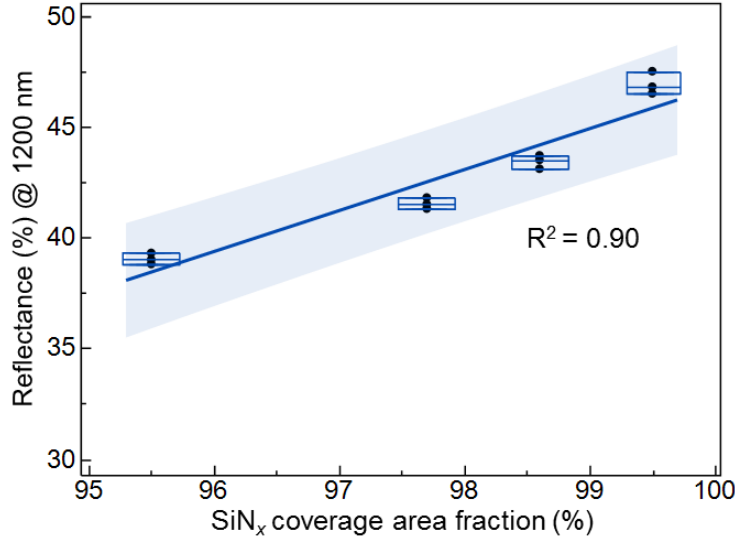
Figure 6.9. The reflectance at 1200 nm wavelength for *n*-PERT-RJ solar cells with different SiN$_x$ coverage area fraction of the rear wafer surface.

The IQE curves provide the information of emitter quality, diffusion length and rear surface recombination velocity (RSVR)[87]. In Fig. 6.7, the IQE of the *n*-PERT-RJ solar cell with PVD-Al rear point contact in the 950-1050 nm wavelength range was reduced up to 4% compared to the cell with SP-Al point contact. This effect is mainly due to the higher surface recombination under the PVD-Al point contact. In addition, the transformation to *a*-Si under the corona ring region which surrounds the PVD-Al point contact reduces the quality of this emitter region and thus is worse than the *c*-Si emitter elsewhere (because of more thermal defects and dangling bonds). In contrast, the SP-Al point contact has a thicker Al-doped *p*$^+$ region generating a better shielding, hence the emitter quality under these metal contacts is better. Although the differences are visible in the comparison of the reflectance and IQE of PVD-Al and SP-Al rear point contact of our *n*-PERT-RJ solar cells, the contribution of these specific wavelength ranges is too small to make an impact on the J_{SC} values (Table 6.2).

TABLE 6.2. Average *n*-PERT-RJ cell performance with Al point contact on the rear.

	J_{SC} (mA/cm^2)	V_{OC} (mV)	**FF** (%)	**Eta** (%)
PVD-Al	39.2	683	79.5	21.3
SP-Al	39.2	684	80.5	21.6

As discussed so far, the two rear side Al metallization methods for forming rear Al point contact make no difference on the V_{OC} and J_{SC} performance of the *n*-PERT-RJ solar cells. In Table 6.2, the FF is the only electrical parameter

makes the solar cell efficiency different. The FF of the *n*-PERT-RJ solar cell with PVD-Al rear point contact is 1% lower than the solar cell with SP-Al point contact. The series resistance (R_S) is inversely related to the FF; when changing the rear side metallization method for forming Al point contact there are two R_S components that will be directly affected: (1) lateral sheet resistance of the Al layer ($R_{sheet, Al}$); (2) specific contact resistivity of the Al rear point contact (ρ_r). The $R_{sheet, Al}$ and the thickness of the PVD-Al layer is 15 mΩ/sq and 2 µm, respectively. In this chapter, this rear Al metal layer is combined with a 5 busbars grid design, the contribution of $R_{sheet, Al}$ to R_S is 0.014 Ω·cm². This value is 0.023 Ω·cm² lower than the R_{sheet} contribution to R_S generated by the Al layer printed with the high wt% Si-add Al paste by. By using the equation (3.3) and (3.4) in Section 3.3.3, the FF has a gain of 0.11% due to the reduction in R_S, and translates to a benefit of 0.03 % in terms of solar cell efficiency. Therefore, the FF-loss of the *n*-PERT-RJ solar cell with PVD-Al rear point contacts is only induced by the higher ρ_r. The standard TLM tool is not possible to measure the ρ_r of the point contacts, here we use the already built up Quokka3 simulation model and feed-in the measurement data (in Table 6.3) to fit the solar cell efficiency for varying ρ_r values.

TABLE 6.3. Input parameters used in Quokka3 device modelling for the fitting of PVD-Al specific contact resistivity

Parameter	Symbol	Value	Unit
Bulk resistivity	ρ_b	2.8	Ω·cm
Bulk minority-carrier lifetime	τ	3.5	ms
Contact pitch on front side	p_f	2	mm
Contact width on front side	w	60	µm
Contact resistivity on front side	ρ_f	2	mΩ·cm²
Line resistance of Ag finger	R_L	0.4	Ohm/cm
Recombination of front contact	$J_{0, Met (Ag)}$	1100	fA/cm²
Sheet resistance of phos.-n^+ FSF	$R_{sheet, FSF}$	150	Ω/sq
Recombination of pass. phos.-n^+ FSF	$J_{0, FSF}$	30	fA/cm²
Contact pitch on rear side	p_r	0.45	mm
Contact radius on rear side	r	30	µm
Contact resistivity on rear side	ρ_r	0.01~8	mΩ·cm²
Sheet resistance of Al contact	$R_{sheet, Al}$	0.015	Ω/sq
Recombination of rear contact	$J_{0, Met (Al)}$	1450	fA/cm²
Sheet resistance of boron-p^+ emitter	$R_{sheet, Emitter}$	200	Ω/sq
Recombination of pass. boron-p^+ emitter	$J_{0, Emitter}$	20	fA/cm²
Shunt resistance	R_{shunt}	12000	Ω

The results are shown in Fig. 6.10, the Al contact resistivity (ρ_r) is set as a variable value and ranging from 0.01 to 8 $m\Omega \cdot cm^2$. When the ρ_r is around 3-4 $\Omega \cdot cm^2$, the measured and simulated efficiency match well. However, for the ρ_r of PVD-Al contacts, this value is too high, especially for contacting such high dopant concentration surface. The doping profile before and after laser ablation is measured to confirm that the surface doping concentration did not change by laser ablation. The ECV profiles are shown in Fig. 6.11, the junction depth after laser ablation becomes 0.1 µm shallower. During laser ablation, the surface silicon will be evaporated to expand and break the dielectric films, then escape from the LCO site. As a consequence, there will be a loss of Si. The surface doping concentration is still at 1.5×10^{19} cm^{-3}. The ρ_r for the PVD-Al contacting the surface of 10^{19} cm^{-3} dopant concentration should be at about 10^{-3} $m\Omega \cdot cm^2$ [154]. The oxide layer grown between the LCO-Si surface and the PVD-Al is the root cause that makes the ρ_r higher than theoretically expected. The literature[154,155] result is assumed that the Al/Si contact area equal to the LCO area. This oxide layer is supposed to be induced by the laser ablation or a native growth, makes an only partial Si area really contact with the Al particle, and carry most of the current. On the contrary, for the SP-Al point contact, there is no oxide layer that will form between the Al-Si alloy and Al-doped p^+ region. The doping concentration of the Al-doped p^+ surface is larger than 10^{17} cm^{-3} [166], so the ρ_c of the SP-Al point contact is at around 1-2 $m\Omega \cdot cm^2$ [167]. The higher ρ_c of PVD-Al point contact makes the n-PERT-RJ solar cells have a lower efficiency. In order to prevent the growth of the oxide layer during the firing process, the LCO process had already been moved to the final step before PVD-Al metallization, but in the end, the same crucial issue still needs to be faced. Moreover, when the front Ag contact has been formed, removal of rear LCO oxides with hydrofluoric acid (HF) is not easy to be introduced in a processing sequence.
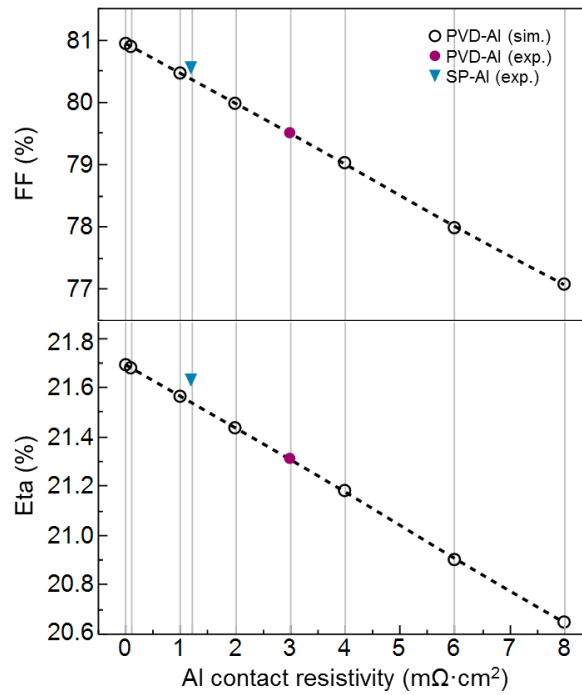
Figure 6.10. FF and efficiency loss of the *n*-PERT-RJ solar cells with varying rear side Al point contact resistivity values. The results are simulated by Quokka3, the color mark efficiency values are from the experimental data.
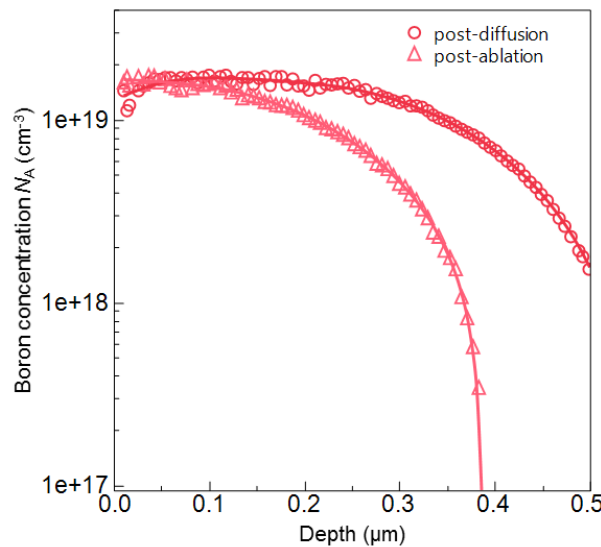
Figure 6.11. The ECV doping profiles of rear boron emitter: post-diffusion and post-ablation.

6.4 Conclusion

In this chapter, we make detailed comparisons between PVD-Al and SP-Al rear point contact of the *n*-PERT-RJ solar cell, on the microstructures, electrical properties of the point contact and also the solar cell's performance. Low contact area fraction and specific contact resistivity were the distinct benefits of applying PVD-Al metallization. However, when SP-Al metallization can also

form an appropriate point contact and there is no oxide layer formed between the LCO and Al layer, as observed for the PVD approach, to affect the contact resistivity, it gradually loses these benefits. The corresponding results of the three discussion parts are as follows:

1) The recombination current under the Al point contact ($J_{0, \text{Met (Al)}}$): for the SP-Al point contacts, a thick (about 2 µm) Al-doped p^+ region is formed after interaction of the Al paste and the bulk Si. This layer highly reduced the $J_{0, \text{Met (Al)}}$ from 1450 fA/cm² (as observed for the PVD-Al) to 635 fA/cm². The higher $J_{0, \text{Met (Al)}}$ of the PVD-Al point contact comes from the poor shielding (only about 0.4 µm thickness of boron doped p^+ after laser ablation) and the thermally induced corona ring region caused during the laser ablation (generating an a-Si layer with a higher trap density). Although the $J_{0, \text{Met (Al)}}$ of the PVD-Al point contact is higher for the n-PERT-RJ solar cells, the minor contact area fraction for this technique (about 0.75% of the wafer area), leads in total to a V_{OC} that is the same as for the device with a SP-Al metallized rear side.

2) The spectral response (reflectance and IQE): for an identical LCOs pitch, the lower PVD-Al point contact area fraction leads to a higher area fraction, that is still covered with SiN$_x$. This fact causes a higher reflectance at the wavelengths between 1150-1200 nm. On the other hand the higher recombination at the contact region, reduces the IQE of the n-PERT-RJ solar cells manufactured with PVD-Al rear contact in the wavelength interval between 950-1150 nm compared to those produced with SP-Al rear contacts. Overall, when considering both, reflectance and IQE, there is no difference in the J_{SC} values visible for the two different Al metallization methods.

3) The Al point contact resistivity (ρ_c): there is a higher ρ_c for the PVD-Al than the SP-Al which induces 1 % FF-loss and hence lowers 0.3 % the n-PERT-RJ solar cell performance. Whether the oxide layer between the Si surface and the Al layer is formed by thermal induction, ablation induction or even native growth, it eventually induces a higher ρ_c and

generates no benefit when applying PVD-Al on the *n*-PERT-RJ solar cells.

As a whole, the SP-Al point contact which is formed by using a Si-add Al paste, brings better performance than the PVD-Al point contact, not merely shown on the electrical properties of the contact, but also on the solar cell efficiency. How to integrate low (e.g. PVD-Al) and high (e.g. SP-Ag) thermal budget metallization is a challenge. In contrast, the rear SP-Al contacts can be co-fired with the front SP-Ag, which is easy to be realized using the existing solar cell production sequence. When discussing "bifacial" application on the *n*-PERT-RJ solar cells and the interconnection in solar modules, the PVD-Al metallization technique will face also more challenges.

Chapter 7: Thesis Summary and Outlook

7.1 Summary

This work is mainly focused on the development of industrial n-PERT-RJ solar cells with screen-printed Al point contact. In **Chapter 1**, the global market of photovoltaics and the cell technology of the crystalline silicon photovoltaics were introduced.

Silicon transportation during the alloying process of the screen-printed Al point contact formation was investigated in **Chapter 2** revealing that is severely affected by the amount of Si-add in the Al paste. The **uniform distribution of the Si-add** in the Al paste effectively **suppressed the out-diffusion of bulk-Si during heating up** of the firing process, resulting in a **higher passivated area ratio** (from 94.1 to 98.7%) of the solar cell's rear side. The **longer recrystallization period** during the cooling down procedure of firing process, **increased the thickness of the Al-doped p^+ region** (from 0 to a maximum of 4 µm) underneath the point contact, and **supplied a better electrical shielding and a lower $J_{0, \text{Met (Al)}}$** (decreasing from 2800 to 635 fA/cm^2). The proposed Si transportation model can be supported by the analysis of contact microstructures and V_{OC} of solar cell devices (increasing from 560 to 682 mV).

The SAM results were shown in **Chapter 3** to reveal that **no voids were formed under the Al point contacts** and that the **quality of the Al point contacts was highly improved** when having Si-add in the Al paste. **The feasibility of screen-printed Al point contact was proven.** The discussions of the adverse impacts or sacrifices on J_{SC} and FF of the n-PERT-RJ solar cells caused by the Si-add in the Al paste were followed up. The rear side reflectance has a direct impact on J_{SC}, but it was not affected by any amounts of Si-add in the Al paste, merely directly related to the rear-side reflector covered area ratio, so there was **no J_{SC} loss caused by the Si-add**. The R_S increases when the amount of Si-add in the Al paste is increased, but the major increment **didn't come from the decreasing conductivity of the Al metal layer.** Rather, **most of the increase is caused by the formation of smaller Al point contacts.** With the premise of identical contact characteristics, there was a 0.4% FF loss for the n-PERT-RJ solar cells processed with high wt% Si-add Al

paste, compared to those that were metallized with low wt% Si-add Al paste. Because of better contact shielding, **a better pFF value was acquired**, compensating the higher FF loss.

There were two strategies for the [Si] gradient management: (1) increasing the Si-add in Al paste or (2) decreasing the Al matrix above each LCO (decreasing the LCO pitch). **The second part of Chapter 3** showed that the contact width and $J_{0, \text{Met (Al)}}$ became gradually independent of the LCO pitch when the amount of the Si-add in the Al paste was modified from none to high wt%. In other words, **Si-add dominated the effect of suppressing the out-diffusion of bulk-Si**. Hence, a **"point-line" contact concept was proposed** for the rear side, consisting of a dot-shaped LCO and Al finger grid design metallized with high wt% Si-add Al paste. The concept not only maintained the V_{OC} **(693 mV)** but had **60% bifaciality,** providing an additional bifacial gain which further reduces the levelized cost of electricity **(LCOE)**.

The *n*-PERT-RJ solar cell concept plays a bridging role not only on the material switching from *p*-type to *n*-type, but also assists migrating from the traditional *mc*-BSF to the future advanced solar cell concepts (e.g., IBC or tandem). Many optimizations were shown in **Chapter 4** for improving solar cell efficiency: (1) a shallower FSF doping profile, which made a better blue response, yielding a **0.3 mA/cm² J_{SC} gain** and a $J_{0, \text{FSF}}$ **decrease from 30 to 25 fA/cm²**; (2) **changing to fine-line printing** (finger width reducing from 60 to 40 µm) and **applying the dash contact concept** reduced the **effective metal fraction from 3% to 1%** resulting in the **area-weighted $J_{0, \text{Met (Ag)}}$ decreasing from 37.2 to 12 fA/cm²**, which brought a **6 mV V_{OC} gain**; (3) screen-printed Al point contacts applied on the rear side with 635 mA/cm² $J_{0, \text{Met (Al)}}$ and **1% effective Al contact area fraction** made **area-weighted $J_{0, \text{Met (Al)}}$ reduce more than 80% to 8.3 fA/cm²**. The $J_{0, \text{Total}}$ **was 77.8 fA/cm²** which translated to a V_{OC} **of 693 mV** and **22.2% cell efficiency**.

In addition to the device performance improvements, the detailed loss analysis and the potential performance for the *n*-PERT-RJ solar cells were performed by Quokka3 simulation in the second part of **Chapter 4**. The efficiency losses from different mechanisms are shown in the free energy loss analysis (FELA); **the recombination loss in the FSF** and **resistive loss in**

the bulk were the largest two of all loss mechanisms which should be optimized as a higher priority. The roadmap for reaching 700 mV V_{OC} and beyond 23% cell efficiency with diffused surfaces and all screen-printed metallization was also shown.

In **Chapter 5**, a more detailed discussion on the device level was proved. First, it was explained why the selective doping FSF structure had less benefit on our solar cells, only increasing the complexity and cost of the process. Then, the impact of different n-bulk parameters on n-PERT-RJ solar cell performance was revealed. The R_{bulk} **between 1-13 Ω·cm** can keep a **stable solar cell efficiency.** τ_{bulk} **should be higher than 2 ms** preventing severe performance decreases. Reducing the bulk **thickness to 145 μm** can compensate for the higher cost of the n-type wafers. The n-PERT-RJ solar cells in this thesis perform as well as the advanced passivating contact solar cells today. Only standard mass-production tools were used and **the COO is comparable to the p-PERC solar cells** with the selective emitter (SE). There was **nearly no LeTID degradation**, which makes these n-PERT-RJ solar cells have **high performance, low cost, simple process, and long-term stability.**

The result of detailed comparisons of the microstructures, the contact electrical properties and the device performance between PVD-Al and SP-Al rear point contact n-PERT-RJ solar cells were shown in **Chapter 6**. **The SP-Al point contact brought better performance than the PVD-Al point contact,** not merely in regards to the electrical properties **($J_{0, \text{Met (Al)}}$ of 635 fA/cm² comparing to 1450 fA/cm²)** of the contact, but also to the solar cell efficiency **(0.3 % higher)**. Integrating low (e.g. PVD-Al) and high (e.g. SP-Ag) thermal budget metallization is a challenge. In contrast, the rear SP-Al contacts can co-fire with the front SP-Ag, which is easier to realize using existing solar cell production lines. When discussing the further "bifacial" application on the n-PERT-RJ solar cells and the interconnections on the solar modules, the PVD-Al metallization will face more challenges.

Future work may involve investigations into applying multi-layer front-side anti-reflection coating (ARC) and the optimization of the pyramid size of the front side texture in order to improve the J_{SC}. In addition, further works on the module level such as studying the interconnecting Ag pads design, and

investigation of the reaction between the Ag pads and rear Al contact at the overlapping sites should be carried out. The use of electrically conductive adhesive (ECA) interconnection could be another topic, committing to the complete removal of lead from PV manufacturing and helping to produce more eco-friendly energy.

7.2 Outlook

The global PV market, dominated by Europe over the last decade, has rapidly changed to an Asia dominated market. The solar photovoltaic industry is transforming into a large-scale production industry. Especially in China, there are many multi-GW production bases that have been built up. This development is linked to state subsidies which helps Chinese industry achieve global leadership in solar photovoltaics, but also brings both risks and opportunities at the same time. If these new large-scale manufacturing companies use their cost advantages to offer over 30 years quality guarantee for the PV products, and at reasonable prices (without any virulent price competitions or government subsidizing dumping prices), then PV markets will continue their accelerated growth. On the other hand, because the large scale companies are mostly concentrated in China, lowering the manufacturing costs by increasing to large production volumes, this makes high price competitive pressure on the small and medium-scale companies in the rest of the world. Focusing on niche markets (the high efficiency n-type solar cells e.g., n-PERT, n-IBC solar cell concepts), offering high-end and high value-added products, or special solutions tailor-made for customers in different PV demands (e.g., desert, snow, pave, noise barrier) are the lower risk strategies for these companies to survive. The other, higher risk, strategy is to develop technologically more advanced and cheaper solar cell concepts. So, in this thesis, the n-PERT-RJ solar cell technology with advanced Al metallization was developed and the high performance, simple process steps, low cost, and long-term stability have been demonstrated. In addition, it was argued that the flexible rear-side design can satisfy bifacial-PV demands.

The major measures for reducing the LCOE and thus ensuring the long-term competitiveness of solar PV power generation are: (a) making cost improvements in mono wafering /crystallization technology; (b) using larger size

wafers; (c) improvement of the cell performance; (d) the introduction of bifacial cell concepts; (e) improving module technologies and; (f) using the sun tracking system. The LCOE decreased by around 14% year-on-year in 2018[9], now enabling power prices in the 2 US cents/kWh range in many high radiation level places around the world. Low generation cost alone is not enough to facilitate growth; it also needs the right policy frameworks and energy market designs. The LCOE of solar PV energy has space for further reduction, and renewable energies are still the only ones to offer the prospect of a reduction rather than an increase in prices in the future. The solar module and its process materials are no longer the biggest contributor to system cost. The increased cell and module performance will support the reduction of PV system costs and spread the grid parity to all over the world, and this was the reason for this thesis focussing on the performance improvements of the *n*-PERT-RJ solar cells. Fig. 7.1 shows the onset of grid parity across Europe, and it is worth noting that grid parity is predicted to spread through Konstanz by 2019, and then continue on into northern Europe before 2030.

Figure 7.1. The grid parity spread in Europe. (*Data source*: ref.[168])

Combining solar radiation and silicon (27.7% of Earth's crust; it is the second most abundant element in the crust, being surpassed only by oxygen) as the source of green energy have been established. In the early stages, solar PV energy was only applied to the aerospace satellite which is less connection with our living electricity. But now we are entering a new era, in which renewable energy plants can generate electricity at the same or even lower prices than traditional power plants, with even lower carbon emissions. The government involvement through FiTs and subsidy schemes will soon be totally withdrawn, and the free market demand will be the driving force of the future. The solar PV technology continues to develop and improve to an even higher level of performance and lower level of cost. Solar PV panels are easy to install, scale and maintain. They are well-suited to the decentralised energy grids; drawing power from multiple and localized energy network can drive competition up and power prices down as the number of energy providers increases. This will all lead finally to a situation in which grid parity spreads across the world, making the solar PV energy transition a worldwide reality.

7.3 Zusammenfassung

Diese Arbeit konzentriert sich hauptsächlich auf die Entwicklung industrieller n-PERT Solarzellen mit rückseitigem Emitter und siebgedruckten Aluminium-Punktkontakten. In **Kapitel 1** wurden der Weltmarkt der Photovoltaik und die Zelltechnologie der kristallinen Silizium-Photovoltaik vorgestellt.

In **Kapitel 2** wurde die Ausbildung von Aluminium-Punktkontakten in siebgedruckten Silizium-Solarzellen untersucht. Es zeigte sich, dass der Transport von Silizium während des Legierungsprozesses sehr stark vom Anteil an beigemengtem Si in der Al-Paste beeinflusst wird. Dabei unterdrückt das gleichförmig in der Paste verteilte Si-Additiv wirksam das Ausdiffundieren von Si aus dem Wafer-Substrat **während der Aufheizphase im Feuerungsprozess**, **wodurch sich der passivierte Flächenanteil auf der Solarzellenrückseite von 94,1 auf 98,7% erhöhte**. Durch die Si-Beimengung verlängert sich die Rekristallisationsphase während des Abkühlvorgangs des Feuerungsprozesses. Dies trägt dazu bei, **die Dicke des Al-dotierten p^+-Bereiches unterhalb des Punktkontaktes von 0 bis auf einen Höchstwert von 4 µm** zu erhöhen. Damit verbessert sich **die elektrische Abschirmung und $J_{0, \text{Met (Al)}}$ sinkt von 2800 auf 635 fA/cm².** Das vorgeschlagene Modell zur Siliziummigration stützt sich zusätzlich auf die Analyse von Kontakt-Mikrostrukturen und auf die V_{OC}-Werte vollständig prozessierter Solarzellen, deren Spannung sich **von 560 auf 682 mV erhöhte.**

SAM-Ergebnisse in **Kapitel 3** machen deutlich, dass keine Hohlräume unter den Al-Punktkontakten gebildet werden und dass die Qualität der Kontakte durch die Si-Beimengung in der Paste stark erhöht wird. **Die grundsätzliche Machbarkeit von Punktkontakten mit siebgedruckter Al-Paste wird damit aufgezeigt.** Nachteilige Auswirkungen der Si-Beimengung zur Al-Paste und Verluste in J_{SC} und FF bei n-PERT Solarzellen mit rückseitigem Emitter wurden im Anschluss diskutiert. Das Reflexionsvermögen der Rückseite hat direkten Einfluss auf die Kurzschlussstromdichte J_{SC}, es wird aber nicht von der verwendeten Menge an Si-Additiv in der Al-Paste negativ beeinflusst. Es ergibt sich lediglich ein direkter Zusammenhang zur eingenommenen Fläche der Metallkontakte auf

der Rückseite, da sich dadurch der Flächenanteil für den rückseitigen Reflektor reduziert. **Die Si-Beimengungen verursachten demnach keine J_{SC} Verluste**.

Der Serienwiderstand Rs der Solarzelle erhöht sich, wenn der Si-Anteil in der Paste ansteigt. **Die Zunahme ergibt sich für unsere Solarzellen jedoch nicht in erster Linie aufgrund der sinkenden Leitfähigkeit der Al-Metallschicht. Der größte Teil des Anstiegs wird durch die Bildung kleinerer Al-Punkt-Kontakte verursacht.** Unter der Prämisse identischer Eigenschaften der Kontakte ergibt sich ein FF-Verlust bei n-PERT Solarzellen mit rückseitigem Emitter von 0,4 %, wenn die Solarzellen mit Al-Paste mit hohem statt niedrigem Si-Anteil prozessiert wurden. Aufgrund einer besseren Abschirmung der Kontakte verbessert sich jedoch **der pFF-Wert**, der den erhöhten FF-Verlust wieder kompensiert.

Zwei Strategien wurden verfolgt, um den Si-Gradienten bei der Kontaktbildung zu steuern: (1) Erhöhung des Si-Anteils in der Paste oder (2) Reduktion der verfügbaren Al-Matrix oberhalb jeder Laser-Kontaktöffnung. (durch Verringerung der Abstände der einzelnen Kontakte voneinander). **Im zweiten Teil von Kapitel 3** wurde gezeigt, dass sich mit zunehmendem Anteil von Si-Additiven in der Al-Paste der Einfluss des Abstands der Kontaktpunkte auf die Größe der Kontaktfläche als auch auf $J_{0, \text{Met (Al)}}$ entkoppelte. Anders gesagt, **die Si-Additive waren der dominierende Baustein, um die Diffusion von Si aus dem Wafer heraus zu unterdrücken.** Es wurde infolgedessen für die Metallisierung der Rückseite der Solarzellen ein **Punkt-Linien-Konzept** vorgeschlagen, welches sich aus Punktöffnungen unter einem Liniendruck mit Al-Paste-zusammensetzt und eine Al-Paste mit hohem Si-Anteil verwendet. Dieses Konzept kann nicht nur das V_{OC}-Niveau von **693 mV** halten, sondern ermöglicht aufgrund einer **60-prozentigen Bifazialität** auch eine Steigerung des Ertrags der Solarzelle, wodurch sich die genormten Kosten für die gewonnene Elektrizität (**LCOE**) weiter reduzieren.

Das n-PERT Solarzellen-Konzept mit rückseitigem Emitter kann sowohl eine Brücke beim technologischen Wechsel von p-Typ zu n-Typ-Silizium darstellen, als auch dabei helfen, den Übergang von traditionellen mc-Solarzellen mit Al-BSF-Passivierung hin zu fortschrittlichen Solarzellen-

Konzepten der Zukunft (wie z.B. IBC- oder Tandemstrukturen) umzusetzen. In **Kapitel 4** wurden viele punktuelle Verbesserungen gezeigt, die dabei halfen, den Wirkungsgrad der Solarzelle zu erhöhen: (1) Durch die geringere Dotierung des „Front Surface Field" (FSF), verbesserte sich die Ausbeute des kurzwelligen Lichts, *J*$_{SC}$ **stieg um 0,3 mA/cm² an** und *J*$_{0, FSF}$ **verringerte sich von 30 auf 25 fA/cm²**. (2) Der Übergang zu Feinliniendruck **reduzierte die Fingerbreite von 60 auf 40 µm**. Die Verwendung von unterbrochenen Kontaktlinien verringerte die **effektive Metall-Kontaktfläche von 3% auf 1%**, wodurch sich der auf die Gesamtfläche normierte *J*$_{0, Met (Ag)}$ **Wert von 37,2 auf 12 fA/cm² reduzierte** und **Voc-Gewinn von 6 mV ermöglichten.** (3) Siebgedruckte Al-Punktkontakte auf der Rückseite mit einem *J*$_{0, Met (Al)}$ von 635 mA/cm² **reduzierten bei einer effektiven Kontaktfläche von 1% den flächengewichteten Anteil von *J*$_{0, Met (Al)}$ um mehr als 80 % auf 8,3 fA/cm².** Dadurch ergab sich ein *J*$_{0, Total}$ **von 77,8 fA/cm²,** wodurch ein *V*$_{OC}$ **von 693 mV** und ein **Wirkungsgrad mit 22,2%** ermöglicht wurden.

Zusätzlich zu oben erwähnten Verbesserungen der Leistungsfähigkeit der *n*-PERT Solarzellen mit rückseitigem Emitter wurden im zweiten Teil von **Kapitel 4** mittels Quokka3-Simulation detaillierte Verlust- und Potential-Analysen durchgeführt. In einer Energieverlustanalyse (free energy loss analysis, FELA) wurden die verschiedenen Verlustmechanismen dargestellt, wobei die **Rekombinationsverluste im FSF** und die **Widerstandsverluste in der Basis** die größten Beiträge darstellen und mit Vorrang verbessert werden sollten. Darüber hinaus wurde ein Weg aufgezeigt, wie mit diffundierten Oberflächen und Siebdrucktechnologie ein *V*$_{OC}$ über 700 mV und Wirkungsgrade über 23% erreicht werden können.

In **Kapitel 5** findet eine ausführlichere Diskussion des Solarzellen-Konzepts statt. Darin wird zunächst erläutert, weshalb in unserem Fall eine selektiv dotierte FSF Struktur für unsere Solarzellen keinen Vorteil erbringt und lediglich die Komplexität und die Kosten des Prozesses erhöht. Al nächstes wurde der Einfluss unterschiedlicher Basisdotierung des Substrates auf die Leistung von *n*-PERT Solarzellen mit rückseitigem Emitter aufgezeigt. Für einen **Widerstandsbereich von 1-13 Ω·cm** kann ein stabiles Wirkungsgradniveau gehalten werden. Die Lebensdauer des Materials τ_{bulk}

sollte über 2 ms liegen, um deutliche Einbrüche der Leistung zu vermeiden. Durch die Reduzierung der Waferdicke auf 145 µm können die höheren Kosten des *n*-Typ Wafer-Materials aufgefangen werden. Die *n*-PERT Solarzellen mit rückseitigem Emitter, die in dieser Arbeit besprochen werden, haben dasselbe Wirkungsgradniveau wie Solarzellen, die auf der Basis von passivierten Kontakten vorgestellt wurden. Es werden für die Herstellung lediglich Geräte genutzt, die auch in der Massenproduktion zum Einsatz kommen. **Die Produktionskosten (COO) sind vergleichbar mit jenen, die zur Herstellung von *p*-PERC Solarzellen mit selektivem Emitter anfallen**. Es wurde nur minimale LeTID-Degradation beobachtet, womit *n*-PERT Solarzellen mit rückseitigem Emitter sich in Summe durch **einen hohen Wirkungsgrad, geringe Herstellungskosten, einen einfachen Herstellungsprozess und stabile, langfristige Haltbarkeit auszeichnen.**

Ein ausführlicher Vergleich zur Mikrostruktur, den Kontakt- und den elektrischen Eigenschaften sowie der Leistung von *n*-PERT Solarzellen, die mit aufgedampftem PVD-Al bzw. siebgedruckter Al Metallpaste hergestellt wurden, ist Gegenstand von **Kapitel 6**. Dabei erwiesen sich die siebgedruckten Punktkontakte im Vergleich zu den aufgedampften Kontakten als leistungsfähiger, sowohl was die elektrischen Eigenschaften **(mit einem $J_{0, \text{Met (Al)}}$ von 635 fA/cm² im Unterschied zu 1450 fA/cm² für die aufgedampften Kontakte)** als auch den Wirkungsgrad der Solarzellen **(0,3 % höher)** betraf. Die Verbindung eines Metallisierungsschritts bei niedrigen Temperaturen (aufgedampftes Al), mit Hochtemperaturprozessen (z.B. das Feuern von siebgedruckten Silberfingern auf der Vorderseite) ist eine Herausforderung. Im Gegensatz dazu können siebgedruckte Al-Kontakte gleichzeitig mit den ebenfalls siebgedruckten Silber-Frontkontakten gefeuert werden, was sich mühelos in den Prozess einer bestehenden Produktionslinie einbinden lässt. Wenn darüber hinaus die bifaziale Anwendung der *n*-PERT-Solarzellen mit rückseitigem Emitter sowie deren Verschaltung im Modul betrachtet werden, ergeben sich für den PVD Ansatz noch größere Herausforderungen.

Zukünftige Arbeiten könnten sich mit der Erforschung von mehrschichtigen Antireflexschichten und einer Optimierung der Pyramidengröße der Textur auf der Vorderseite beschäftigen, um dadurch den

Kurzschluss-Strom J_{SC} zu erhöhen. Zusätzlich könnten Arbeiten auf Modulebene, wie z. B. eine Untersuchung zum Layout der Silberpads auf der Zellrückseite sowie den Reaktionen zwischen Silberpad und dem überlappenden Al-Kontakt durchgeführt werden. Der Übergang zu Verbindungen mit elektrisch leitenden Klebern könnte ein weiteres Themengebiet sein, das dabei hilft, zukünftig Blei aus der Photovoltaik Produktion zu entfernen und somit noch umweltfreundlichere Energie zu produzieren.

7.4   Ausblick

Der globale Photovoltaikmarkt, der im letzten Jahrzehnt von Europa dominiert wurde, hat sich schnell zu einem von Asien geprägten Markt verändert. Die Photovoltaikbranche wandelt sich zu einer Industrie der Massenproduktion. Insbesondere in China sind etliche Multi-GW-Fabriken aufgebaut worden. Diese Entwicklung ist eng verknüpft mit staatlichen Unterstützungen, die es der chinesischen Industrie erlauben, die globale Führerschaft im Photovoltaikmarkt einzunehmen. Diese Entwicklung ist zugleich Chance und Risiko: Wenn diese neuen, im großen Maßstab produzierenden Firmen ihre Kostenvorteile dazu nutzen, um zu vernünftigen Preisen PV-Produkte anzubieten, deren Qualität und Haltbarkeit mehr als 30 Jahre garantiert werden kann, ohne auf schädliche Preiskämpfe oder staatlich gefördertes Dumping zurückzugreifen, werden die PV Märkte ihr beschleunigtes Wachstum weiter fortsetzen. Da sich andererseits beinahe alle Fabriken, die im großen Maßstab produzieren, in China konzentrieren und diese die Herstellungskosten durch die Erhöhung ihres Produktionsvolumens reduzieren, entsteht für alle kleineren- oder mittelgroßen Betriebe in der restlichen Welt ein enormer Preisdruck. Eine Konzentration auf Nischenmärkte (z. B. hocheffiziente n-Typ-Solarzellen wie n-PERT oder n-IBC Solarzellenkonzepte), in denen höchste Qualität oder besonders angepasste oder maßgeschneiderte Produkte mit einem speziellen Mehrwert für den Kunden bedient werden (wie Wüstenbedingungen, Schnee oder Lärmschutz), stellen für diese Firmen eine Strategie dar, um im Markt zu überleben. Eine andere Möglichkeit ist es, technologisch fortschrittlichere und kostengünstigere Solarzellenkonzepte zu verfolgen. In dieser Arbeit wurde die n-PERT Solarzellen-technologie mit rückseitigem Emitter und fortschrittlicher Al-

Metallisierung weiterentwickelt und dabei deren hohe Leistungsfähigkeit, einfache Herstellung sowie Kosteneffizienz und Langzeitstabilität gezeigt. Das flexible Design der Rückseite erlaubt auch bifaziale Anwendungen.

Die wirksamsten Schritte, um Kosten zu reduzieren sind (a) technologische Verbesserungen beim Schneiden und bei der Kristallisation von monokristallinen Substraten, (b) Verwendung größerer Substrate, (c) Verbesserung der Zelleffizienz, (d) Einführung von bifazialen Solarzellenkonzepten, (e) Verbesserung der Modultechnologien und (f) Verwendung von der Sonne nachgeführten Systeme, um damit die langfristige Konkurrenzfähigkeit der solaren PV-Energiegewinnung zu sichern. Die Stromgestehungskosten (LCOE) sanken unter Berufung auf Lazard Capital um ca. 14% im Jahresvergleich für 2018, wodurch Energiepreise im Bereich von 2 US Cents/kWh für viele Orte auf der Welt, die günstige Sonneneinstrahlbedingungen besitzen, ermöglicht werden. Niedrige Herstellungskosten allein genügen jedoch nicht, um das Wachstum zu fördern. Es bedarf auch der richtigen politischen Randbedingungen und einer angepassten Ausgestaltung der Energiemärkte. Die Gestehungskosten von Photovoltaikstrom haben noch Spielraum für weitere Senkungen; und erneuerbare Energien sind immer noch die einzigen Energieträger, die in Zukunft eher eine Senkung als eine Erhöhung der Preise in Aussicht stellen. Die Verbindung von verringerten Herstellungskosten und erhöhter Zell- und Modulleistungsfähigkeit wird am meisten dazu beitragen, die Systemkosten für Photovoltaik weiter zu senken und die Netzparität für Solarstrom überall auf der Welt zu erreichen. Aus diesem Grund hat sich diese Arbeit auf Verbesserungen der Leistungsfähigkeit von n-PERT-Solarzellen mit rückseitigem Emitter konzentriert. Abbildung 7.1. zeigt eine Prognose, wann sich an verschieden Orten in Europa, abhängig von Strompreisen und Strahlungsintensität, Netzparität einstellt. Laut der Prognose wird diese in Konstanz 2019 erreicht und bis 2030 soll sich die Netzparität bis nach Nordeuropa ausdehnen.

Die Verbindung von Sonnenstrahlung und Silizium (27,7% der Erdkruste bestehen daraus, es ist das zweithäufigste Element der Erde, das nur von Sauerstoff übertroffen wird) haben sich als Quelle von grüner Energie etabliert.

In den frühen Phasen diente Photovoltaik hauptsächlich in der Raumfahrt für Satelliten, die keine Verbindung zu unseren Energiequellen hatten. Wir läuten nun eine neue Ära ein, in der regenerative Energie zum selben oder sogar niedrigeren Preis und mit deutlich niedrigeren CO_2-Emissionen herstellt werden kann als Energie aus traditionellen Kraftwerken. Die Förderungen durch die Politik, wie Einspeisetarife und Subventionsregelungen, werden bald auslaufen und die Nachfrage der freien Märkte wird in Zukunft die treibende Kraft sein. Die Photovoltaik-Technologie wird sich weiterentwickeln und noch leistungsfähiger und kostengünstiger werden. Da PV-Module einfach zu installieren, erweitern und warten sind, eignen sie sich sehr gut für eine dezentrale Stromversorgung. Indem sie Energie in vielfältigen und lokalen Netzwerken zur Verfügung stellen, können sie den Wettbewerb erhöhen und die Energiepreise senken, da sich die Anzahl der Stromanbieter erhöht. Schließlich wird sich die Netzparität über die ganze Welt ausbreiten und den Übergang in das solare Energiezeitalter zu einer weltweiten Realität machen.

References

(1)   *CO₂ Emissions from Fuel Combustion*; International Energy Agency, 2017.

(2)   Jäger-Waldau, A. *Energies* **2019**, *12*, 769–775.

(3)   *World Energy Outlook 2017* ; International Energy Agency, 2018.

(4)   *Paris Agreement*; UNFCCC, 2015.

(5)   *Cost-Competitive Renewable: Potential across South East Europe*; IRENA, 2017.

(6)   Reinders, A.; Verlinden, P.; Sark, W. V.; Freundlich, A. *Photovoltaic solar energy: from fundamentals to applications*; John Wiley & Sons, 2017.

(7)   Arantegui, R. L.; Jäger-Waldau, A. *Renewable and Sustainable Energy Reviews* **2018**, *81*, 2460–2471.

(8)   Jones, D.; Sakhel, A.; Buck, M.; Graichen, P. *The European Power Sector in 2018*; Agora Energiewende and Sandbag, 2019.

(9)   Hemetsberger, W.; Schmela, M. *Global Market Outlook For Solar Power / 2019 - 2023*; SolarPower Europe, 2019.

(10)   Breyer, C.; Bogdanov, D.; Aghahosseini, A.; Gulagi, A.; Child, M.; Oyewo, A. S.; Farfan, J.; Sadovskaia, K.; Vainikka, P. *Progress in Photovoltaics: Research and Applications* **2018**, *26*, 505–523.

(11)   *China: Challenges and Prospects from an Industrial and Innovation Powerhouse*; Joint Research Centre, 2019.

(12)   Masson, G. *Trends in PV Market 2018*; IEA Photovoltaic Power Systems Programme (PVPS), 2018.

(13)   Glunz, S. W.; Preu, R.; Biro, D. *Comprehensive renewable energy* **2012**, *1*, 353–387.

(14)   Srivastava, H. *Crystalline Silicon PV Market by Type (Mono-Crystalline and Multi-Crystalline) and End-User (Residential and Commercial, Utility-Scale) - Global Opportunity Analysis and Industry Forecasts, 2014 - 2022*; Allied Market Research, 2016.

(15)   Jin, J.; Melkonyan, K.; Hu, H.; Zoco, E. *PV Module Supply Chain Tracker 2018*; IHS Markit, 2018.

(16)   *International Technology Roadmap for Photovoltaic (ITRPV)-Results 2018*; VDMA Photovoltaic Equipment, 2019.

(17)   Kopecek, R.; Libal, J.; Koduvelikulathu, L. J. *Is LeTID degradation in PERC cells another degradation crisis even worse than PID?*; PV-TECH, 2018.

(18)   Schmidt, J.; Aberle, A. G.; Hezel, R. In *Photovoltaic Specialists Conference,*

1997., Conference Record of the Twenty-Sixth IEEE; 1997; pp. 13–18.

(19)   Hashigami, H.; Itakura, Y.; Saitoh, T. *Journal of applied physics* **2003**, *93*, 4240–4245.

(20)   Knobloch, J.; Glunz, S. W.; Biro, D.; Warta, W.; Schaffer, E.; Wettling, W. In *Conference Record of the Twenty-Fifth IEEE Photovoltaic Specialists Conference-1996*; 1996; pp. 405–408.

(21)   Glunz, S. W.; Schaffer, E.; Rein, S.; Bothe, K.; Schmidt, J. In *3rd World Conference onPhotovoltaic Energy Conversion, 2003. Proceedings of*; 2003; Vol. 1, pp. 919–922.

(22)   Pernau, T.; Romer, O.; Scheiffele, W.; Reichart, A.; Jooß, W. In *Proceedings of the 31st European Photovoltaic Solar Energy Conference, Hamburg, Germany*; 2015; pp. 14–18.

(23)   Walter, D. C.; Steckenreiter, V.; Helmich, L.; Pernau, T.; Schmidt, J. In *Proceeding of the 33rd European Photovoltaic Solar Energy Conference, Amsterdam, The Netherlands*; 2017; pp. 377–381.

(24)   Vaqueiro-Contreras, M.; Markevich, V. P.; Coutinho, J.; Santos, P.; Crowe, I. F.; Halsall, M. P.; Hawkins, I.; Lastovskii, S. B.; Murin, L. I.; Peaker, A. R. *Journal of Applied Physics* **2019**, *125*, 185704.

(25)   Niewelt, T.; Schoen, J.; Warta, W.; Glunz, S. W.; Schubert, M. C. *IEEE Journal of Photovoltaics* **2016**, *7*, 383–398.

(26)   née Wenham, A. C.; Wenham, S.; Chen, R.; Chan, C.; Chen, D.; Hallam, B.; Payne, D.; Fung, T.; Kim, M.; Liu, S.; Wang, S.; Kim, K.; Samadi, A.; Sen, C.; Vargas, C.; Varshney, U.; Stefani, B. V.; Hamer, P.; Bourret-Sicotte, G.; Nampalli, N.; Hameiri, Z.; Chong, C.; Abbott, M. In *2018 IEEE 7th World Conference on Photovoltaic Energy Conversion (WCPEC)(A Joint Conference of 45th IEEE PVSC, 28th PVSEC & 34th EU PVSEC)*; 2018; pp. 0001–0008.

(27)   Herguth, A.; Derricks, C.; Sperber, D. *IEEE Journal of Photovoltaics* **2018**, *8*, 1190–1201.

(28)   Mihailetchi, V. D.; Chu, H.; Lossen, J.; Kopecek, R. *IEEE Journal of Photovoltaics* **2018**, *8*, 435–440.

(29)   Kopecek, R.; Peng, Z.-W.; Buck, T.; Comparotto, C.; Mihailetchi, V. D.; Koduvelikulathu, L. J.; Libal, J.; Lossen, J.; Nakahara, M.; Tsuji, K.; Dhamrin, M.; Jooss, W. *Low-cost standard nPERT solar cells towards 23% efficiency and 700mV voltage using Al paste technology*; 2019; Vol. 42, pp. 74–84.

(30)   Romijn, I. In *bifi PV Workshop*; 2017.

(31)   Hiroshi, M. *Radiation energy transducing device*; US Patent 3,278,811, 1966.

(32)   Bordina, N. M.; Zadde, V. V.; Zaitseva, A. K.; Landsman, A. P.; Strebkov, D. S.; Streltsova, V. I.; Unishkov, V. A. *Semiconductor photoelectric generator*; US

Patent 3,948,682, 1976.

(33)   Hauser, A.; Richter, A.; Leu, S. *Cell and module design from the LCOE perspective. Article PV Production Annual 2014*; Meyer Burger, 2014.

(34)   Jäger-Waldau, A. *PV Status Report 2018*; Office for Official Publications of the European Communities, Luxembourg, 2018.

(35)   *Wind energy in Europe in 2018, trends and statistics*; Europe, Wind, 2018.

(36)   Dullweber, T.; Kranz, C.; Baumann, U.; Hesse, R.; Walter, D.; Schmidt, J.; Altermatt, P.; Brendel, R. In *Photovoltaic Specialists Conference (PVSC), 2013 IEEE 39th*; 2013; pp. 3074–3078.

(37)   Schmidt, J.; Bothe, K.; Bock, R.; Schmiga, C.; Krain, R.; Brendel, R. In *Proceedings of the 22nd European Photovoltaic Solar Energy Conference, Milan, Italy*; 2007; pp. 998–1001.

(38)   Dai, X.; Green, M.; Wenham, S. In *Photovoltaic Specialists Conference, 1993., Conference Record of the 23th IEEE*; 1993; pp. 153–156.

(39)   Sinton, R. A.; Cuevas, A. *Applied Physics Letters* **1996**, *69*, 2510–2512.

(40)   Huster, F. In *Proceedings of the 20th European Photovoltaic Solar Energy Conference, Barcelona, Spain*; 2005; pp. 1466–1469.

(41)   Murray, J.; McAlister, A. *Journal of Phase Equilibria* **1984**, *5*, 74–84.

(42)   Beaucarne, G.; Choulat, P.; Ma, Y.; Dross, F.; UrueÀa, A.; Agostinelli, G.; Szlufcik, J.; John, J. In *1st Workshop on Metallization of Crystalline Silicon Solar Cells*; 2008.

(43)   Rüdiger, M.; Schmiga, C.; Rauer, M.; Hermle, M.; Glunz, S. W. In *Proceedings of the 25th European Photovoltaic Solar Energy Conference, Valencia, Spain*; 2010; pp. 2280–2286.

(44)   Rüdiger, M.; Greulich, J.; Richter, A.; Hermle, M. *IEEE Transactions on Electron Devices* **2013**, *60*, 2156–2163.

(45)   Rauer, M.; Schmiga, C.; Glatthaar, M.; Glunz, S. W. *IEEE Journal of Photovoltaics* **2013**, *3*, 206–211.

(46)   Swanson, R. M. *Solar Cells* **1986**, *17*, 85–118.

(47)   Sinton, R.; Kwark, Y.; Gan, J.; Swanson, R. M. *IEEE Electron Device Letters* **1986**, *7*, 567–569.

(48)   King, R.; Sinton, R.; Swanson, R. In *Photovoltaic Specialists Conference, 1988., Conference Record of the Twentieth IEEE*; 1988; pp. 538–544.

(49)   Blakers, A. W.; Wang, A.; Milne, A. M.; Zhao, J.; Green, M. A. *Applied Physics Letters* **1989**, *55*, 1363–1365.

(50)   Zhao, J.; Wang, A.; Green, M. A. *Progress in Photovoltaics: Research and Applications* **1999**, *7*, 471–474.

(51)   McIntosh, K. R.; Cudzinovic, M. J.; Smith, D. D.; Mulligan, W. P.; Swanson, R. M. In *Photovoltaic Energy Conversion, 2003. Proceedings of 3rd World Conference on*; 2003; Vol. 1, pp. 971–974.

(52)   Meemongkolkiat, V.; Nakayashiki, K.; Kim, D. S.; Kim, S.; Shaikh, A.; Kuebelbeck, A.; Stockum, W.; Rohatgi, A. In *Photovoltaic Energy Conversion, Conference Record of the 2006 IEEE 4th World Conference on*; 2006; Vol. 2, pp. 1338–1341.

(53)   Bähr, M.; Heinrich, G.; Doll, O.; Köhler, I.; Maier, C.; Lawerenz, A. In *26th European Photovoltaic Solar Energy Conference and Exhibition, Hamburg, Germany*; 2011; pp. 1203–1209.

(54)   Preu, R.; Glunz, S.; Schäfer, S.; Lüdemann, R.; Wettling, W.; Pfleging, W. In *Proceedings of the 16th European Photovoltaic Solar Energy Conference*; 2000; pp. 1181–1184.

(55)   Agostinelli, G.; Szlufcick, J.; Choulat, P.; Beaucarne, G. In *Proceedings of the 20th European Photovoltaic Solar Energy Conference*; 2005; pp. 1011–1014.

(56)   Gatz, S.; Hannebauer, H.; Hesse, R.; Werner, F.; Schmidt, A.; Dullweber, T.; Schmidt, J.; Bothe, K.; Brendel, R. *physica status solidi (RRL)-Rapid Research Letters* **2011**, *5*, 147–149.

(57)   Heinrich, G.; Bähr, M.; Stolberg, K.; Wütherich, T.; Leonhardt, M.; Lawerenz, A. *Energy Procedia* **2011**, *8*, 592–597.

(58)   Wütherich, T.; Katkhouda, K.; Bornschein, L.; Grohe, A.; Krokoszinski, H. *Energy Procedia* **2012**, *27*, 537–542.

(59)   Engelhardt, J.; Ohl, S.; Hahn, G.; Terheiden, B. *Energy Procedia* **2013**, *38*, 707–712.

(60)   Rapp, S.; Heinrich, G.; Domke, M.; Huber, H. P. *Physics Procedia* **2014**, *56*, 998–1006.

(61)   Glunz, S. W.; Preu, R.; Schaefer, S.; Schneiderlochner, E.; Pfleging, W.; Ludemann, R.; Willeke, G. In *Photovoltaic Specialists Conference, 2000. Conference Record of the Twenty-Eighth IEEE*; 2000; pp. 168–171.

(62)   Mader, C.; Müller, J.; Gatz, S.; Dullweber, T.; Brendel, R. In *Photovoltaic Specialists Conference (PVSC), 2010 35th IEEE*; 2010; pp. 001446–001449.

(63)   Engelhart, P.; Harder, N.; Neubert, T.; Plagwitz, H.; Fischer, B.; Meyer, R.; Brendel, R. In *21th European Photovoltaic Solar Energy Conference and Exhibition, Dresden, Germany*; 2006; pp. 773–776.

(64)   Kim, T.; Harley, G.; Smith, D. D.; Cousins, P. J. *High throughput laser ablation*

References

processes and structures for forming contact holes in solar cells; US Patent 8,692,111, 2014.

(65)   Tao, Y.; Payne, A.; Upadhyaya, V. D.; Rohatgi, A. *Progress in Photovoltaics: Research and Applications* **2014**, *22*, 1030–1039.

(66)   Du, Z.; Zhang, C.; Li, F.; Zhou, R.; Hong, M. *IEEE Journal of Photovoltaics* **2016**, *6*, 617–623.

(67)   Mader, C.; Müller, J.; Eidelloth, S.; Brendel, R. *Solar Energy Materials and Solar Cells* **2012**, *107*, 272–282.

(68)   Schneiderlöchner, E.; Preu, R.; Lüdemann, R.; Glunz, S. W. *Progress in Photovoltaics: Research and Applications* **2002**, *10*, 29–34.

(69)   Wolf, A.; Wotke, E. A.; Mack, S.; Nekarda, J.-F.; Biro, D.; Preu, R.; Schlegel, K.; Weber, T.; Lossen, J.; Böscke, T.; Grohe, A.; Engelhart, P.; Müller, J. W.; Schubert, G.; Plagwitz, H.; Gassenbauer, Y. In *Proceedings of the 25th European Photovoltaic Solar Energy Conference and Exhibition, Valencia, Spain*; 2010; pp. 1391–1395.

(70)   Mohr, A.; Wanka, S.; Stekolnikov, A.; Scherff, M.; Seguin, R.; Engelhart, P.; Klenke, C.; Lee, J. Y.; Tardon, S.; Diez, S.; Wendt, J.; Hintze, B.; Hoyer, R.; Schmidt, S.; Müller, J. W.; Wawer, P. *Energy Procedia* **2011**, *8*, 390–395.

(71)   Nekarda, J.; Hörteis, M.; Lottspeich, F.; Wolf, A.; Preu, R. In *Proceedings of the 25th European Photovoltaic Solar Energy Conference and Exhibition, Valencia, Spain*; 2010; pp. 2245–2249.

(72)   Grohe, A.; Schneiderlochner, E.; Hermle, M.; Preu, R.; Glunz, S. W.; Willeke, G.; Walz, S. In *Photovoltaic Energy Conversion, 2003. Proceedings of 3rd World Conference on*; 2003; Vol. 2, pp. 1032–1035.

(73)   Glunz, S. W.; Grohe, A.; Hermle, M.; Schneiderlochner, E.; Dicker, J.; Preu, R.; Mackel, H.; Macdonald, D.; Cuevas, A. In *Photovoltaic Energy Conversion, 2003. Proceedings of 3rd World Conference on*; 2003; Vol. 2, pp. 1332–1335.

(74)   Glunz, S. W.; Schneiderlöchner, E.; Kray, D.; Grohe, A.; Hermle, M.; Kampwerth, H.; Preu, R.; Willeke, G. In *Proceedings of the 19th European Photovoltaic Solar Energy Conference, Paris, France*; 2004; pp. 408–411.

(75)   Naumann, V.; Hagendorf, C.; Werner, M.; Henke, B.; Schmidt, C.; Nekarda, J.; Bagdahn, J. In *Proceedings of the 24th European Photovoltaic Solar Energy Conference, Hamburg, Germany*; 2009; pp. 2180–2184.

(76)   Ortega, P.; Orpella, A.; Martin, I.; Colina, M.; López, G.; Voz, C.; Sánchez, M.; Molpeceres, C.; Alcubilla, R. *Progress in Photovoltaics: Research and Applications* **2012**, *20*, 173–180.

(77)   Böscke, T.; Hellriegel, R.; Wütherich, T.; Bornschein, L.; Helbig, A.; Carl, R.; Dupke, M.; Stichtenoth, D.; Aichele, T.; Jesswein, R.; others. In *Photovoltaic Specialists Conference (PVSC), 2011 37th IEEE*; 2011; pp. 003663–003666.

(78)   Gatz, S.; Müller, J.; Dullweber, T.; Brendel, R. *Energy Procedia* **2012**, *27*, 95–102.

(79)   Lauermann, T.; Zuschlag, A.; Scholz, S.; Hahn, G.; Terheiden, B. In *26th European Photovoltaic Solar Energy Conference and Exhibition*; 2011; pp. 1137–1143.

(80)   Müller, J.; Bothe, K.; Gatz, S.; Plagwitz, H.; Schubert, G.; Brendel, R. *IEEE transactions on electron devices* **2011**, *58*, 3239–3245.

(81)   Müller, J.; Bothe, K.; Gatz, S.; Brendel, R. *physica status solidi (RRL)-Rapid Research Letters* **2012**, *6*, 111–113.

(82)   Münzer, K.; Schöne, J.; Teppe, A.; Schlosser, R.; Hein, M.; Hammer, D.; Hüls, S.; Hanke, M.; Keller, S.; Fath, P. In *Proceedings of the 25th European Photovoltaic Solar Energy Conference, Valencia, Spain*; 2010; pp. 2314–2318.

(83)   Lachowicz, A.; Ramspeck, K.; Roth, P.; Manole, M.; Blanke, H.; Hefner, W.; Brouwer, E.; Schum, B.; Metz, A. In *Proceedings of the 27th European Photovoltaic Solar Energy Conference and Exhibition, Frankfurt, Grmany*; 2012; pp. 1846–1850.

(84)   Rauer, M.; Schmiga, C.; Woehl, R.; Ruhle, K.; Hermle, M.; Horteis, M.; Biro, D.; Glunz, S. W. *IEEE Journal of Photovoltaics* **2011**, *1*, 22–28.

(85)   Rauer, M.; Woehl, R.; Ruhle, K.; Schmiga, C.; Hermle, M.; Horteis, M.; Biro, D. *IEEE Electron Device Letters* **2011**, *32*, 916–918.

(86)   Peng, Z.-W.; Nakahara, M.; Buck, T.; Kopecek, R. In *AIP Conference Proceedings*; 2018; Vol. 1999, p. 100002.

(87)   Fischer, B. *Loss analysis of crystalline silicon solar cells using photoconductance and quantum efficiency measurements*; Cuvillier Göttingen, 2003.

(88)   Shockley, W. *Bell System Technical Journal* **1949**, *28*, 435–489.

(89)   Dressler, K.; Dauwe, S.; Droste, T.; Rossa, J.; Meidel, R.; Schünemann, K.; Ramspeck, K.; Gassenbauer, Y.; Metz, A. *Proceedings of the 27th European Photovoltaic Solar Energy Conference and Exhibition, Frankfurt, Grmany* **2012**, 755–758.

(90)   Dressler, K.; Rauer, M.; Kaloudis, M.; Dauwe, S.; Herguth, A.; Hahn, G. *IEEE Journal of Photovoltaics* **2015**, *5*, 70–76.

(91)   Horbelt, R.; Hahn, G.; Job, R.; Terheiden, B. *Energy Procedia* **2015**, *84*, 47–55.

(92)   Liu, J.; Janssen, G. J. M.; Koppes, M.; Kossen, E. J.; Tool, K.; Komatsu, Y.; Anker, J.; Gutjahr, A.; Vlooswijk, A.; Luchies, J. M.; Siareyeva, O.; Granneman, E.; Romijn, I. In *Proceedings of the 31st European Photovoltaic Solar Energy Conference and Exhibition, Hamburg, Germany*; 2015; pp. 633–636.

(93)   Rauer, M.; Mondon, A.; Schmiga, C.; Bartsch, J.; Glatthaar, M.; Glunz, S. W.

Energy Procedia **2013**, *38*, 449–458.

(94)   Schiele, Y.; Joos, S.; Hahn, G.; Terheiden, B. *Energy Procedia* **2014**, *55*, 295–301.

(95)   Rauer, M.; Schmiga, C.; Hermle, M.; Glunz, S. W. In *Proceedings of the 24th European Photovoltaic Solar Energy Conference, Hamburg, Germany*; 2009; pp. 20–25.

(96)   Liang, Z.; Chen, D.; Zhu, Y.; Shen, H. *Science China Technological Sciences* **2010**, *53*, 3209–3213.

(97)   Meier, D.; Good, E.; Garcia, R.; Bingham, B.; Yamanaka, S.; Chandrasekaran, V.; Bucher, C. In *Photovoltaic Energy Conversion, Conference Record of the 2006 IEEE 4th World Conference on*; 2006; Vol. 2, pp. 1315–1318.

(98)   Yang, Y.; Xu, G.; Zhang, K.; Zhang, X.; Shen, H.; Altermatt, P. P.; Verlinden, P.; Feng, Z. In *Proceedings of the 28th European Photovoltaic Solar Energy Conference, Paris, France*; 2013; pp. 1558–1561.

(99)   Katkhouda, K.; Schubert, D.; Grohe, A.; Schaaf, P. *Photovoltaics, IEEE Journal of* **2015**, *5*, 299–306.

(100)   Green, M. A. *Solar cells: operating principles, technology, and system applications*; Englewood Cliffs, NJ, Prentice-Hall, Inc., 1982. 288 p., 1982.

(101)   Sinton, R.; Cuevas, A. In *Proceedings of the 16th European Photovoltaic Solar Energy Conference*; 2000; Vol. 1152.

(102)   Schmidt, J. In *Solid State Phenomena*; 2004; Vol. 95, pp. 187–196.

(103)   Bordihn, S.; Mertens, V.; Cieslak, J.; Hörnlein, S.; Müller, J. W. *Status of high efficiency, low cost n-type silicon solar cells*; Elsevier, 2017; Vol. 124, pp. 643–648.

(104)   Lammert, M. D.; Schwartz, R. J. *IEEE Transactions on Electron Devices* **1977**, *24*, 337–342.

(105)   Richter, A.; Benick, J.; Kalio, A.; Seiffe, J.; Hörteis, M.; Hermle, M.; Glunz, S. W. *Energy Procedia* **2011**, *8*, 479–486.

(106)   Lim, B.; Brendemühl, T.; Berger, M.; Christ, A.; Dullweber, T. In *Proceeding of the 29th European Photovoltaic Solar Energy Conference, Amsterdam, The Netherlands*; 2014; pp. 661–665.

(107)   Kopecek, R.; Buck, T.; Libal, J.; Rover, I.; Wambach, K.; Geerligs, L.; Sánchez-Friera, P.; Alonso, J.; Wefringhaus, E.; Fath, P. In *Photovoltaic Energy Conversion, Conference Record of the 2006 IEEE 4th World Conference on*; 2006; Vol. 1, pp. 1044–1047.

(108)   Schmiga, C.; Hermle, M.; Glunz, S. W. In *Proceedings of 23rd European Photovoltaic Solar Energy Conference, Valencia, Spian*; 2008; pp. 982–987.

(109) Bock, R.; Schmidt, J.; Mau, S.; Hoex, B.; Brendel, R. *IEEE Transactions on Electron Devices* **2010**, *57*, 1966–1971.

(110) Bordihn, S.; Mertens, V.; Engelhart, P.; Florian, T.; Cieslak, J.; Stenzel, F.; Kappe, P.; Lee, J.; Lindner, T.; Junghänel, M.; Müller, J. W.; Kessels, W. M. M.; Wawer, P. In *26th European Photovoltaic Solar Energy Conference, Hamburg, Germany*; 2011; pp. 429–432.

(111) Lee, J.; Choi, Y.; Lee, J.; Oh, H.; Kyeong, D.; Kim, T.; Hwang, M.-I.; Cho, E.-C. In *Proceedings of the 32nd European Photovoltaic Solar Energy Conference, Munich, Germany*; 2016; pp. 951–954.

(112) Cho, J.; Lee, J.; Choi, Y.; Lee, J.; Oh, H.; Kim, T.; Hwang, M.; Cho, E.-C. *21%-Efficient n-type rear-junction PERT solar cell with industrial thin 156mm Cz single crystalline silicon wafer*; Elsevier, 2015; Vol. 77, pp. 279–285.

(113) Dullweber, T.; Wehmeier, N.; Nowack, A.; Brendemühl, T.; Kajari-Schröder, S.; Brendel, R. *physica status solidi (a)* **2016**, *213*, 3046–3052.

(114) Wang, W.; Sheng, J.; Yuan, S.; Sheng, Y.; Cai, W.; Chen, Y.; Zhang, C.; Feng, Z.; Verlinden, P. J. *IEEE Journal of Photovoltaics* **2015**, *5*, 1245–1249.

(115) Bassi, N.; Clerc, C.; Pelet, Y.; Hiller, J.; Fakhfouri, V.; Droz, C.; Despeisse, M.; Levrat, J.; Faes, A.; Bätzner, D.; Papet, P. In *Proceeding of the 29th European Photovoltaic Solar Energy Conference, Amsterdam, The Netherlands*; 2014; pp. 1180–1185.

(116) Tous, L.; Chen, J.; Choulat, P.; Singh, S.; van der Heide, A. S. H.; Aleman, M.; Kuzma-Filipek, I.; J. John, F. D.; Szlufcik, J. In *Proceedings of the 35th European Photovoltaic Solar Energy Conference, Brussels, Belgium*; 2018; pp. 354–358.

(117) Deng, W.; Ye, F.; Liu, R.; Li, Y.; Chen, H.; Xiong, Z.; Yang, Y.; Chen, Y.; Wang, Y.; Altermatt, P. P.; Feng, Z.; Verlinden, P. J. In *Photovoltaic Specialists Conference, 2017. Conference Record of the Forty-fourth IEEE*; 2017.

(118) Meier, S.; Saint-Cast, P.; Wöhrle, N.; Fell, A.; Greulich, J.; Wolf, A.; Glunz, S. W. *Journal of Applied Physics* **2017**, *122*, 183102.

(119) Zanuccoli, M.; De Rose, R.; Magnone, P.; Sangiorgi, E.; Fiegna, C. *IEEE Transactions on Electron Devices* **2012**, *59*, 1311–1319.

(120) Gérenton, F.; Mandorlo, F.; Brette, J.-B.; Lemiti, M. *Energy Procedia* **2015**, *77*, 677–686.

(121) *International Technology Roadmap for Photovoltaic (ITRPV), 9th Edition*; 2018.

(122) Xie, M.; Ren, C.; Fu, L.; Qiu, X.; Yu, X.; Yang, D. *Frontiers in Energy* **2017**, *11*, 67–71.

(123) Fertig, F.; Lantzsch, R.; Mohr, A.; Schaper, M.; Bartzsch, M.; Wissen, D.; Kersten, F.; Mette, A.; Peters, S.; Eidner, A.; Cieslak, J.; Duncker, K.; Junghänel, M.; Jarzembowski, E.; Kauert, M.; Faulwetter-Quandt, B.; Meißner, D.; Reiche, B.;

References

Geißler, S.; Hörnlein, S.; Klenke, C.; Niebergall, L.; Schönmann, A.; Weihrauch, A.; Stenzel, F.; Hofmann, A.; Rudolph, T.; Schwabedissen, A.; Gundermann, M.; Fischer, M.; Müller, J. W.; Jeong, D. J. W. *Energy Procedia* **2017**, *124*, 338–345.

(124) Herguth, A.; Derricks, C.; Keller, P.; Terheiden, B. *Energy Procedia* **2017**, *124*, 740–744.

(125) Lim, B.; Merkle, A.; Peibst, R.; Dullweber, T.; Wang, Y.; Zhou, R. In *Proceeding of the 35th European Photovoltaic Solar Energy Conference, Brussels, Belgium*; 2018; pp. 359–365.

(126) Haschke, J.; Seif, J. P.; Riesen, Y.; Tomasi, A.; Cattin, J.; Tous, L.; Choulat, P.; Aleman, M.; Cornagliotti, E.; Uruena, A.; Russell, R.; Duerinckx, F.; Champliaud, J.; Levrat, J.; Abdallah, A. A.; Aïssa, B.; Tabet, N.; Wyrsch, N.; Despeisse, M.; Szlufcik, J.; Wolf, S. D.; Ballif, C. *Energy & Environmental Science* **2017**, *10*, 1196–1206.

(127) Comparotto, C.; Theobald, J.; Lossen, J.; Mihailetchi, V. In *Proceedings of the 33rd European Photovoltaic Solar Energy Conference, Amsterdam, The Netherlands*; 2017; pp. 832–836.

(128) Peiner, E.; Schlachetzki, A.; Krüger, D. *Journal of the Electrochemical Society* **1995**, *142*, 576–580.

(129) Meier, D. L.; Schroder, D. K. *IEEE transactions on electron devices* **1984**, *31*, 647–653.

(130) Ramspeck, K.; Schenk, S.; Komp, L.; Metz, A.; Meixner, M. In *Proceedings of the 29th European Photovoltaic Solar Energy Conference and Exhibition, Amsterdam, The Netherlands*; 2014; pp. 1253–1256.

(131) McIntosh, K. R.; Altermatt, P. P.; Ratcliff, T. J.; Fong, K. C.; Black, L. E.; Baker-Finch, S. C.; Abbott, M. D. **2013**, 1672–1679.

(132) King, R.; Sinton, R.; Swanson, R. *IEEE Transactions on electron devices* **1990**, *37*, 365–371.

(133) Weber, J.; Gutscher, S.; Lohmüller, S.; Lohmüller, E.; Brand, A. A. In *35th European Photovoltaic Solar Energy Conference and Exhibition*; 2018; pp. 379 – 384.

(134) Singh, S.; Tous, L.; Choulat, P.; Chen, J.; Liu, R.; Ma, L.; Wu, X.; Wang, J.; Liu, Z.; Duerinckx, F.; Gordon, I.; Szlufcik, J.; Poortmans, J. 35th European Photovoltaic Solar Energy Conference and Exhibition, Brussels, Belgium, 2018; pp. 580 – 583.

(135) Raabe, B.; Book, F.; Dastgheib-Shirazi, A.; Hahn, G. In *25th European Photovoltaic Solar Energy Conference and Exhibition 5th World Conference on Photovoltaic Energy Conversion, 6-10 September 2010, Valencia, Spain*; 2010; pp. 1174 – 1178.

(136) Yan, D.; Cuevas, A.; Bullock, J.; Wan, Y. In *Photovoltaic Specialists Conference*

(PVSC), 2014 IEEE 40th; 2014; pp. 2545–2549.

(137)   Edwards, M.; Bocking, J.; Cotter, J. E.; Bennett, N. *Progress in Photovoltaics: Research and Applications* **2008**, *16*, 31–45.

(138)   Shanmugam, V.; Khanna, A.; Perez, D. J.; Tabajonda, R. V.; Ali, J. M. Y.; Ortega, A. L. M.; Garcia, I. J.; Lim, B.; Mueller, T. *Solar Energy Materials and Solar Cells* **2018**, *186*, 124–130.

(139)   Ok, Y.-W.; Tam, A. M.; Huang, Y.-Y.; Yelundur, V.; Das, A.; Payne, A. M.; Chandrasekaran, V.; Upadhyaya, A. D.; Jain, A.; Rohatgi, A. **2018**.

(140)   Fell, A.; Schön, J.; Schubert, M. C.; Glunz, S. W. *Solar Energy Materials and Solar Cells* **2017**, *173*, 128–133.

(141)   Chu, H.; Preis, P.; Lossen, J.; Mojrová, B.; Buchholz, F.; Becht, G.; Mayberry, R. W.; Hörteis, M.; Mihailetchi, V. D. *IEEE Journal of Photovoltaics* **2018**, *8*, 923–929.

(142)   Mihailetchi, V. D.; Chu, H.; Lossen, J.; Kopecek, R. *IEEE Journal of Photovoltaics* **2018**, *8*, 435–440.

(143)   Kerr, M. J.; Schmidt, J.; Cuevas, A.; Bultman, J. H. *Journal of Applied Physics* **2001**, *89*, 3821–3826.

(144)   Sai, H.; Umishio, H.; Matsui, T.; Nunomura, S.; Kawatsu, T.; Takato, H.; Koji. *Japanese Journal of Applied Physics* **2018**, *57*, 08RB10.

(145)   Feldmann, F.; Bivour, M.; Reichel, C.; Hermle, M.; Glunz, S. W. *Solar energy materials and solar cells* **2014**, *120*, 270–274.

(146)   Stodolny, M. K.; Lenes, M.; Wua, Y.; Janssen, G. J. M.; Romijn, I. G.; Luchies, J. R. M. *Solar Energy Materials and Solar Cells* **2016**, *158*, 24–28.

(147)   Peibst, R.; Römer, U.; Larionova, Y.; Rienäcker, M.; Merkle, A.; Folchert, N.; Reiter, S.; Turcu, M.; Min, B.; Krügener, J.; Tetzlaff, D.; Bugiel, E.; Wietler, T.; Brendel, R. *Solar Energy Materials and Solar Cells* **2016**, *158*, 60–67.

(148)   Nandakumar, N.; Rodriguez, J.; Kluge, T.; Grosse, T.; Fondop, L.; Padhamnath, P.; Balaji, N.; König, M.; Duttagupta, S. *Progress in Photovoltaics: Research and Applications* **2019**, *27*, 107–112.

(149)   Wang, Y. In *nPV Workshop*; 2018.

(150)   PVinsight: All Solar PV Price http://pvinsights.com/.

(151)   Peibst, R.; Larionova, Y.; Reiter, S.; Wietler, T. F.; Orlowski, N.; Schäfer, S.; Min, B.; Stratmann, M.; Tetzlaff, D.; Krügener, J.; others. *IEEE Journal of Photovoltaics* **2018**, *8*, 719–725.

(152)   Liu, Y. In *nPV Workshop*; 2018.

References

(153)   Stodolny, M. K.; Anker, J.; Geerligs, B. L.; Janssen, G. J.; Van De Loo, B. W.; Melskens, J.; Santbergen, R.; Isabella, O.; Schmitz, J.; Lenes, M.; others. *Energy Procedia* **2017**, *124*, 635–642.

(154)   Schroder, D. K.; Meier, D. L. *IEEE Transactions on electron devices* **1984**, *31*, 637–647.

(155)   Chang, C.; Fang, Y.; Sze, S. *Solid-State Electronics* **1971**, *14*, 541–550.

(156)   Huber, M. R.; Dörr, M.; Wohlfart, P. In *Proceedings of the 27th European Photovoltaic Solar Energy Conference, Frankfurt, Germany*; 2012; pp. 1185–1187.

(157)   Heinemeyer, F.; Mader, C.; Münster, D.; Dullweber, T.; Harder, N.-P.; Brendel, R. In *2nd Workshop on Metallization for Crystalline Silicon Solar Cells*; 2010.

(158)   Knorz, A.; Peters, M.; Grohe, A.; Harmel, C.; Preu, R. *Progress in Photovoltaics: Research and Applications* **2009**, *17*, 127–136.

(159)   Hermann, S.; Dezhdar, T.; Harder, N.-P.; Brendel, R.; Seibt, M.; Stroj, S. *Journal of Applied Physics* **2010**, *108*, 114514.

(160)   Chichkov, B. N.; Momma, C.; Nolte, S.; Von Alvensleben, F.; Tünnermann, A. *Applied Physics A* **1996**, *63*, 109–115.

(161)   Stuart, B. C.; Feit, M. D.; Rubenchik, A. M.; Shore, B. W.; Perry, M. D. *Physical review letters* **1995**, *74*, 2248–2251.

(162)   Rublack, T.; Seifert, G. *Optical Materials Express* **2011**, *1*, 543–550.

(163)   Liu, P. L.; Yen, R.; Bloembergen, N.; Hodgson, R. T. *Applied Physics Letters* **1979**, *34*, 864–866.

(164)   Kakkad, R.; Smith, J.; Lau, W. S.; Fonash, S. J.; Kerns, R. *J. Appl. Phys.* **1989**, *65*, 2069–2072.

(165)   Liu, G.; Fonash, S. J. *Applied Physics Letters* **1989**, *55*, 660–662.

(166)   Krause, J.; Woehl, R.; Rauer, M.; Schmiga, C.; Wilde, J.; Biro, D. *Solar Energy Materials and Solar Cells* **2011**, *95*, 2151–2160.

(167)   Woehl, R.; Gundel, P.; Krause, J.; Ruhle, K.; Heinz, F. D.; Rauer, M.; Schmiga, C.; Schubert, M. C.; Warta, W.; Biro, D. *IEEE Transactions on Electron Devices* **2010**, *58*, 441–447.

(168)   *Grid parity and the solar renaissance*; BayWa Renewable Energy GmbH, 2019.

Appendix

A.I   Calibration certificate

Fraunhofer ISE CalLab PV Cells

Heidenhofstr.2

79110 Freiburg

Fraunhofer
ISE

CalLab
PV Cells

akkreditiert durch die / *accredited by the*

Deutsche Akkreditierungsstelle GmbH

als Kalibrierlaboratorium im / *as calibration laboratory in the*

Deutschen Kalibrierdienst   **DKD**

ilac-MRA   DAkkS
Deutsche
Akkreditierungsstelle
D-K-11140-01-00

Kalibrierschein	1003059ISC
Calibration certificate	D-K-11140-01-00
Kalibrierzeichen	
Calibration mark	2018-03

Gegenstand *Object*	**Solar cell**	Dieser Kalibrierschein dokumentiert die Rückführung auf nationale Normale zur Darstellung der Einheiten in Übereinstimmung mit dem Internationalen Einheitensystem (SI).
Hersteller *Manufacturer*	-	Die DAkkS ist Unterzeichner der multilateralen Übereinkommen der European co-operation for Accreditation (EA) und der International Laboratory Accreditation Cooperation (ILAC) zur gegenseitigen Anerkennung der Kalibrierscheine.
Typ *Type*	**monocrystalline silicon**	Für die Einhaltung einer angemessenen Frist zur Wiederholung der Kalibrierung ist der Benutzer verantwortlich.
Fabrikat/Serien-Nr. *Serial number*	**ISC003 / 2376-197**	*This calibration certificate documents the traceability to national standards, which realize the units of measurement according to the International System of Units (SI).*
Auftraggeber *Customer*	**ISC Konstanz e.V.** **Rudolf-Diesel-Str. 15** **78467 Konstanz** **Germany**	*The DAkkS is signatory to the multilateral agreements of the European co-operation for Accreditation (EA) and of the International Laboratory Accreditation Cooperation (ILAC) for the mutual recognition of calibration certificates.*
Auftragsnummer *Order No.*	**059ISC0318**	*The user is obliged to have the object recalibrated at appropriate intervals.*
Anzahl der Seiten des Kalibrierscheins *Number of pages of the certificate*	**9**	
Datum der Kalibrierung *Date of calibration*	**15.03.2018**	

Dieser Kalibrierschein darf nur vollständig und unverändert weiterverbreitet werden. Auszüge oder Änderungen bedürfen der Genehmigung sowohl der Deutschen Akkreditierungsstelle GmbH als auch des ausstellenden Kalibrierlaboratoriums. Kalibrierscheine ohne Unterschrift haben keine Gültigkeit.
This calibration certificate may not be reproduced other than in full except with the permission of both the Deutsche Akkreditierungsstelle GmbH and the issuing laboratory. Calibration certificates without signature are not valid.

Datum *Date*	Leiter des Kalibrierlaboratoriums *Head of the calibration laboratory*	Bearbeiter *Person in charge*
15.03.2018	Wilhelm Warta	Astrid Semeraro

≡ Fraunhofer
ISE

CalLab
PV Cells

1003059ISC
D-K-
11140-01-00
2018-03

1. Beschreibung des Kalibriergegenstandes
Description of the calibrated object

Das Messobjekt ist eine Solarzelle, Typ: monokristallines Silicium. Die Kontaktierung erfolgt an der Vorderseite der Zelle über die Busbars und ganzflächig auf der Rückseite. Die Stabilität der Solarzelle wurde nicht untersucht.
The device under test is a monocrystalline silicon solar cell. The front contact is realised by the contact grid. The back contact is formed by the whole backside area of the cell. The temporal stability of the solar cell performance was not controlled.

2. Messverfahren
Measurement procedure

Die Kalibrierung des Kalibrierobjektes wird gemäß /1/ mit einem DC-Sonnensimulator Klasse A nach /6/ unter Standardtestbedingungen (STC) durchgeführt. Die Einstrahlung wird mit Hilfe einer Monitorzelle während der gesamten Messdauer aufgenommen und deren Schwankungen bezüglich der Messung korrigiert. Die Divergenz der Randstrahlen ist < 8°. Die Solarzelle wird auf einem Vakuumprobentisch thermisch stabilisiert.
The calibration of the test sample was performed at Standard Testing Conditions (STC) in accordance with /1/ under irradiation with a steady-state class A solar simulator according to /6/. The irradiance is controlled with a monitor cell during the measurement in order to correct fluctuations. The divergence of the peripheral beams is < 8°. The solar cell is kept at a constant temperature on a vacuum chuck.

Rückführung der Referenzsolarzelle / *Traceability of the reference solar cell* :

Identitäts-Nr. / *Identity-Nr.* :	Kalibrierschein-Nr./ *Certificate-Nr.* :	Rückführung/ *Traceability* :
041-2015	47003-PTB-16	PTB

Das Messergebnis für den Kurzschlussstrom enthält eine Korrektur der spektralen Fehlanpassung (Mismatch), die durch die Abweichung der spektralen Verteilung des Klasse A Simulators vom Standard-Spektrum AM1.5G /3/ in Kombination mit den verschiedenen spektralen Empfindlichkeiten von Referenzzelle und Messobjekt entsteht /4/.
Dazu wurde die spektrale Verteilung der Bestrahlung (Sonnensimulator) mit einem Spektralradiometer und die spektrale Empfindlichkeit des Messobjektes mit einem Filtermonochromator /5/ gemessen (s. Kalibrierschein Nr: 3003059ISC2018-03).
The spectral mismatch - caused by the deviation of the simulator spectrum from the standard spectrum AM1.5G /3/ in combination with the difference between the spectral response of the reference cell and that of the device under test (DUT) – is calculated according to /4/ and corrected.
For the spectral mismatch correction the spectral distribution of the solar simulator is measured with a spectroradiometer, the spectral response of the DUT is measured with a filter monochromator according to /5/ (cf. Calibration Mark: 3003059ISC2018-03).

Fraunhofer
ISE

CalLab
PV Cells

1003059ISC
D-K-
11140-01-00
2018-03

Die Rückführung der Spektralmessung auf SI-Einheiten erfolgte über den Vergleich mit einer Standardlampe.
The traceability of the measurement of the spectral distribution to SI-Units is achieved using a standard lamp for the calibration of the spectroradiometer.

Identitäts-Nr. / *Identity-Nr.:*	Kalibrierschein-Nr./ Certificate-Nr.:	Rückführung/ Traceability:
BN-9101-451	40002-14-PTB	PTB

3. Messbedingungen
Measurement conditions

Standardtestbedingungen (STC) / *Standard Testing Conditions (STC)* :

Absolute Bestrahlungsstärke / *Total irradiance* :	1000	W/m²
Temperatur des Messobjektes / *Temperature of the DUT* :	25	°C
Spektrale Bestrahlungsstärke / *Spectral irradiance distribution* :	AM1.5G Ed.2 (2008) /3/	

Die Messung der IV-Kennlinie (Strom-Spannungs-Kennlinie) des Messobjektes erfolgt mit Hilfe eines Vierquadranten-Netzteiles und eines Kalibrierwiderstandes.
The measurement of the IV-curve is performed with a 4-quadrant power amplifier and a calibration resistor.

4. Messergebnis
Measurement results

Kennlinienparameter des Messobjektes unter Standardtestbedingungen (STC) / *IV-curve parameter under Standard Testing Conditions (STC)* :

Leerlaufspannung / *Open-circuit voltage* :	V_{OC}	= (	685.6	±	2.3	) mV
Kurzschlussstrom / *Short-circuit current* (Ed.2-2008):	I_{SC}	= (	9.64	±	0.18	) A
Füllfaktor / *Fill factor* :	FF	= (	80.43	±	0.52	) %
Wirkungsgrad / *Efficiency* :	η	= (	21.78	±	0.44	) %
maximale Leistung / *maximum power* :	P_{MPP}	= (	5.32	±	0.11	) W

Fraunhofer
ISE

CalLab
PV Cells

1003059ISC
D-K-
11140-01-00
2018-03

5. Zusatzinformationen
Additional information

Nur zum Vergleich / *For comparison purposes* :
Berechneter Wert nach bisherigem Normspektrum / *Calculated value according to previous standard spectrum* :

Kurzschlussstrom / I_{SC} = (9.57   ±   0.18   ) A
Short-circuit current
(Ed.1-1989)/2/:

Mismatch-Faktor / MM =   1.0031
Mismatch factor :

(Spektral-Korrektur / *spectral correction*)

Fläche / Area (t)[1]: A = (244.15   ±   0.24   ) cm²

Weitere Kennlinienparameter des Messobjektes unter Standardtestbedingungen (STC) / *Additional IV-curve parameter under Standard Testing Conditions (STC)* :

Kurzschlussstromdichte / *Short-* J_{SC} = (39.49   ±   0.75   ) mA/cm²
circuit current density :

Strom am Punkt max. Leistung / I_{MPP} =   9.07   A
Current at max. power point :

Spannung am Punkt max.
Leistung / *Voltage at max.* V_{MPP} =   586.0   mV
power point :

[1] : (t) = total area, (ap) = aperture area, (da) = designated illumination area /7/

Angegeben ist jeweils die erweiterte Messunsicherheit, die sich aus der Standardmessunsicherheit durch Multiplikation mit dem Faktor k=2 ergibt. Sie wurde gemäß dem "Guide to the expression of Uncertainty in Measurement" ermittelt. Sie entspricht bei einer Normalverteilung der Abweichungen vom Messwert einer Überdeckungswahrscheinlichkeit von 95%.
The expanded measurement uncertainty resulting from the standard measurement uncertainty multiplied with a factor k=2 is specified. The calculation was carried out according to the "Guide to the expression of Uncertainty in Measurement". The value corresponds to a Gaussian distribution denoting the deviations of the measurement value within a probability of 95%.

Fraunhofer

ISE

CalLab
PV Cells

1003059ISC
D-K-
11140-01-00
2018-03
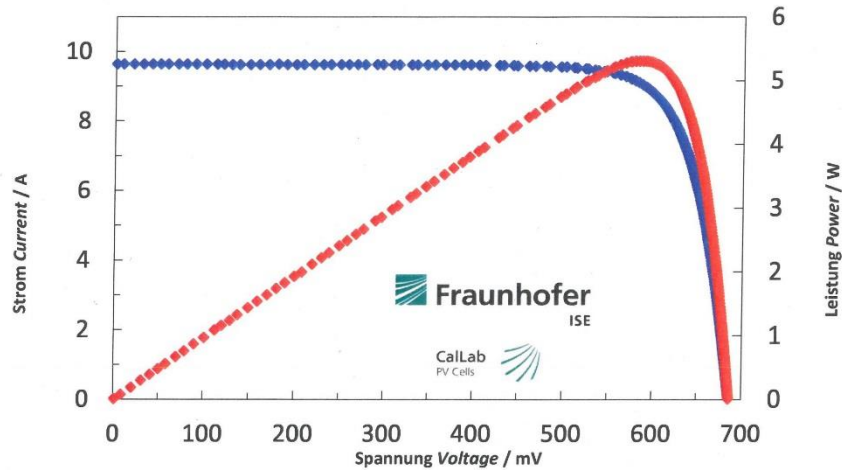
6. Literatur

Literature

/1/ IEC 60904-1-Ed.2:2006, *Photovoltaic devices - Part 1: Measurement of photovoltaic current-voltage characteristics*

/2/ IEC 60904-3-Ed.1:1989, *Photovoltaic devices - Part 3: Measurement principles for terrestrial photovoltaic (PV) solar devices with reference spectral irradiance data*

/3/ IEC 60904-3-Ed.2:2008, *Photovoltaic devices - Part 3: Measurement principles for terrestrial photovoltaic (PV) solar devices with reference spectral irradiance data*

/4/ IEC 60904-7-Ed.3:2008, *Photovoltaic devices - Part 7: Computation of the spectral mismatch error introduced in the testing of a photovoltaic device*

/5/ IEC 60904-8-Ed.3:2014, *Photovoltaic devices - Part 8: Measurement of the spectral responsivity of a photovoltaic (PV) device*

/6/ IEC 60904-9-Ed.2:2010, *Photovoltaic devices - Part 9: Solar simulator performance requirements*

A.II   The history of *n*-PERT rear junction solar cell technology in the last fifteen years

p^+ - Emitter *(Al)*
alloy *(Al-Si)*
rear contact *(SP -Al)*

p^+ - Emitter *(Al)*
a-Si
SiO_X
rear contact *(PVD -Al)*

p^+ - Emitter *(BBr$_3$ -DF)*
passivation layer
rear contact *(PVD -Al)*

2011
[5]*S. Bordihn (Q-Cells), et al.,*
20.2%

2010
[4]*R. Bock (ISFH), et al.,*
20.0%

2009
[3]*C. Schmiga (FhG-ISE), et al.,*
18.2%

2006
[1]*R. Kopecek (ISC-Konstanz), et al.,*
[2]*V. Mihailetchi (ECN), et al.,*
16.4%

[1]IEEE 4th World Conference on Photovoltaic Energy Conversion. Hawaii, USA (2006)
[2]16th Annual NREL Crystalline Silicon Workshop, Colorado, USA (2006)
[3]24th European Photovoltaic Solar Energy Conference, Hamburg, Germany (2009)
[4]IEEE Trans. Electron Devices, vol. 57, no. 8, pp. 1966-1971 (2010)
[5]26th European Photovoltaic Solar Energy Conference, Hamburg, Germany (2011)

p^+ - Emitter *(BBr$_3$ -DF)*
p^+ - Emitter *(Al)*
alloy *(Al-Si)*
rear contact *(Al screen-printed)*

A "hybrid" rear emitter

2017
[10]*S. Bordihn (Q-Cells) et al,*
21.9%

2016
[8]*T, Dullweber (ISFH) et al.,*
21%
[9]*J, LEE (Hyundai HI) et al.,*
21.8%

2015
[6]*W. Wang (Trina Solar), et al.,*
20.6%
[7]*J, Cho (Hyundai HI) et al.,*
21.2%

[6]IEEE J. Photovoltaics, vol. 5, no. 4, pp. 1245-1249. (2015)
[7]Energy Procedia, vol. 77, pp. 279–285. (2015)
[8]Phys. Status Solidi A, 213: 3046–3052. (2016)
[9]32nd European Photovoltaic Solar Energy Conference, Munich, Germany (2016)
[10]Energy Procedia, vol. 124, pp. 643–648. (2017)

A.III   The impact of bulk resistivity on *n*-PERT rear junction solar cells

A.III.1   Light-generated excess carriers flow behavior in the bulk

For *n*-type rear junction solar cells, electron transport in the bulk is more complicated than hole transport, which simply moves toward the rear hole collector (Fig. A.III.1(f)). Since most of the excess carriers are generated near the illuminated surface, a carrier concentration gradient is formed (Fig. A.III.1(g)). It's the main driving force for excess carrier movement. In Fig. A.III.1(a) and (b), the electrons will first diffuse down in the bulk and flow toward the front contacts. When the cross-section location is approaching front contacts, the domination of the electron flow behavior is a trade-off between the illumination-induced and contact-induced concentration gradient (Fig. A.III.1(c)). Fig. A.III.1(e) shows in overall, the electrons move toward the front contacts.
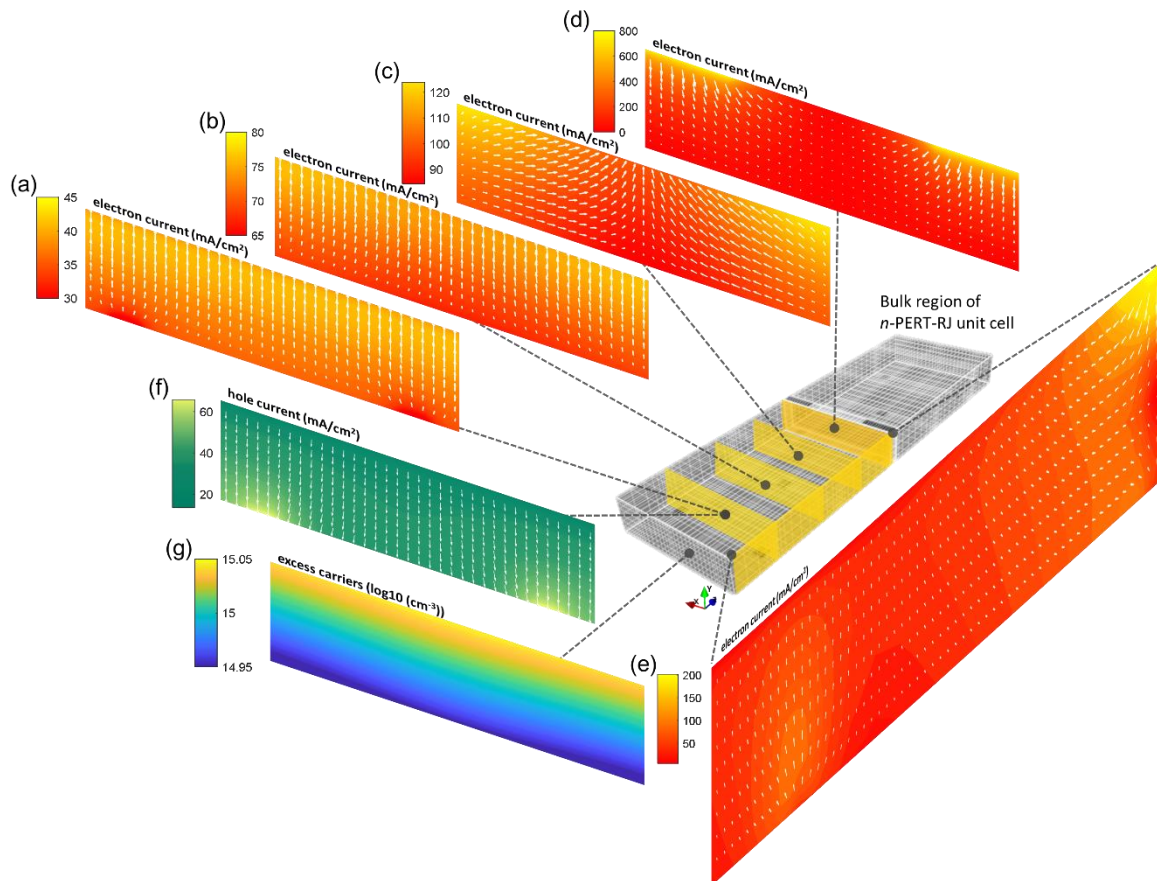

FIGURE A.III.1. The Quokka3 simulation results of the carrier behaviors in the bulk region of *n*-PERT-RJ unit cell at the maximum power point (MPP) condition. The bulk's *xy* plane electron current at *z* = (a) 250 µm, (b) 500 µm, (c) 750 µm and (d) 1000 µm (underneath the front Ag contacts); (e) is the electron current of *yz* plane at *x* = 0 µm. (f) The bulk's *xy* plane hole current at *z* = 250 µm. The white arrows represent the electrical current flow direction. (g) The distribution of light-generated excess carriers in the bulk.

## A.III.2   Regulator for the electron flow distributary

The bulk of *n*-type rear junction solar cells is in a parallel circuit with the FSF, therefore, sharing the resistive loss induced by the lateral electron transport in FSF before being collected by the contacts. As shown in Chapter 4, the bulk resistivity (ρ_b) and thickness are 3 Ω·cm and 165 µm, respectively. The equivalent $R_{sheet, Bulk}$ is 180 Ω/sq, which is equal to $R_{sheet, FSF}$. Half of the electrons will transport through the FSF and half will transport through the bulk to the contacts. This can be verified by the simulated solar cell efficiency losses which are extracted from the FELA of Quokka3. In Fig. A.III.2, the ratio between the efficiency losses induced by the lateral electron transport in FSF and by the electron transport in bulk is almost 50:50. When ρ_b is increased to 13 Ω·cm, the equivalent $R_{sheet, Bulk}$ will increase to 788 Ω/sq, higher than $R_{sheet, FSF}$. More electrons prefer to transport through FSF to the contacts, making the efficiency loss ratio become 60:40. On the contrary, when ρ_b is down to 0.5 Ω·cm, the equivalent $R_{sheet, Bulk}$ will decrease to 30 Ω/sq, the efficiency losses ratio will become 24:76, more electrons prefer to transport through bulk to the contacts. The bulk of *n*-type rear junction solar cells is not only a photon absorber but also a "regulator" for the electron flow distributary, opens the way for ultra-lowly doped FSF profiles that are no longer suited for *p*-PERC's emitter applications. The aim is to obtain lower recombination and free carrier absorption.
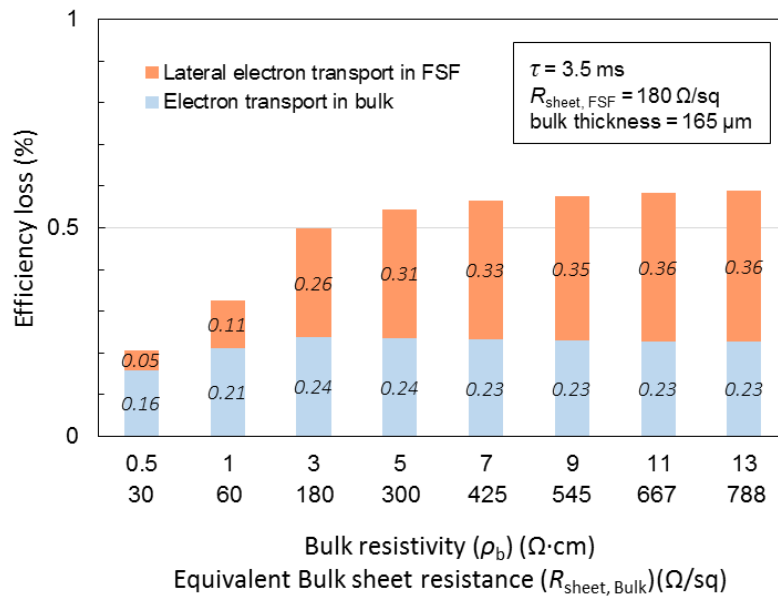
FIGURE A.III.2. The simulated efficiency loss results of the *n*-PERT-RJ solar cells (at the MPP condition) which are extracted from the FELA of Quokka3: (a) induced by the lateral electron transport in FSF (coral color); (b) induced by electron transport in bulk (light blue).

A.III.3   Degradation of the FSF performance induced by the decreasing ρ_b

In Fig. A.III.2, when ρ_b is lower than 3 Ω·cm, the electron transport losses begin to decrease, which corresponds to the FF trend in Fig. 5.4 (directly affected by the R_S). By reducing only ρ_b from 3 to 0.5 Ω·cm, a solar cell efficiency of 0.3% can be directly obtained. But actually, there is an efficiency drop (-0.4%) instead, which is mainly due to the decline in J_{SC}. Applying low ρ_b wafers to our *n*-PERT-RJ solar cells will result in the performance degradation of FSF. The *n*-type rear junction solar cells generally are applied a highly doped n^+ region on the front surface to create a high-low unipolar junction that will shield the holes generated in the bulk. The electric field has no effect on accelerating or slowing down the flow of the holes. Its role is to hold the concentration of electrons in the n^+ region higher than the *n*-bulk region. Any force that may apply on the hole flow toward the front surface is completely neutralized by the gradient of chemical potential. The intensity of the shielding highly correlates to the chemical potential gradient between the bulk and the FSF. Fig. A.III.3 reveals clearly that when ρ_b is reduced from 3 to 0.5 Ω·cm, the dopant concentration will increase one order, strongly reducing the chemical potential gradient between the bulk and the FSF. For shallow FSF doping profiles (the orange and coral color ECV profiles in Fig. A.III.3), changing to lower ρ_b has much obvious impact on the FSF performance than changing the doping profile of the FSF itself.
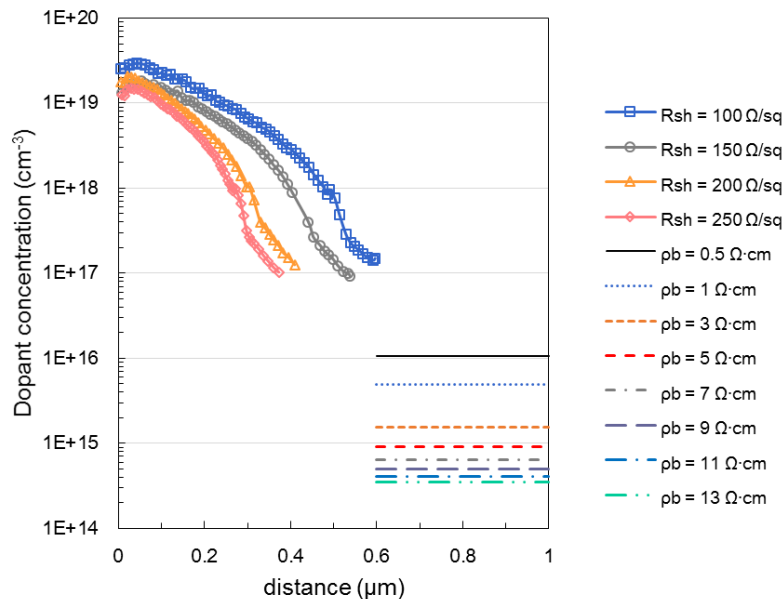
FIGURE A.III.3. The ECV doping profiles of the FSF (the $R_{sheet,\ FSF}$ is varying from 100 to 250 Ω/sq) and the calculated bulk dopant concentration (the ρ_b varying from 0.5 to 13 Ω·cm).

Further investigations of the hole flow in the bulk by Quokka3 simulation at the MPP condition are shown in Fig. A.III.4. When ρ_b is reduced, the holes near the high-low junction underneath the front contacts start to flow toward the FSF, this is because the shielding is not strong enough; the high electron density underneath the contacts makes the chemical potential gradient even smaller. Then explains well why in Fig. 5.4, there is a huge J_{SC} drop when applying the low ρ_b value wafers and reveals the selective doping structures under the metal contacts bring more benefits to the low ρ_b devices (in addition to the lower $J_{0,\,Met}$, the higher FF and the lower J_{SC} losses are more noteworthy). When the holes diffusing cross the high-low junction induces not only leakage current but also leads to higher recombination loss in the FSF. A lower FSF recombination induced efficiency loss indicates that the n^+ region (FSF) blocks holes quite effectively because there is less recombination in its volume or at the metal contacting surface.
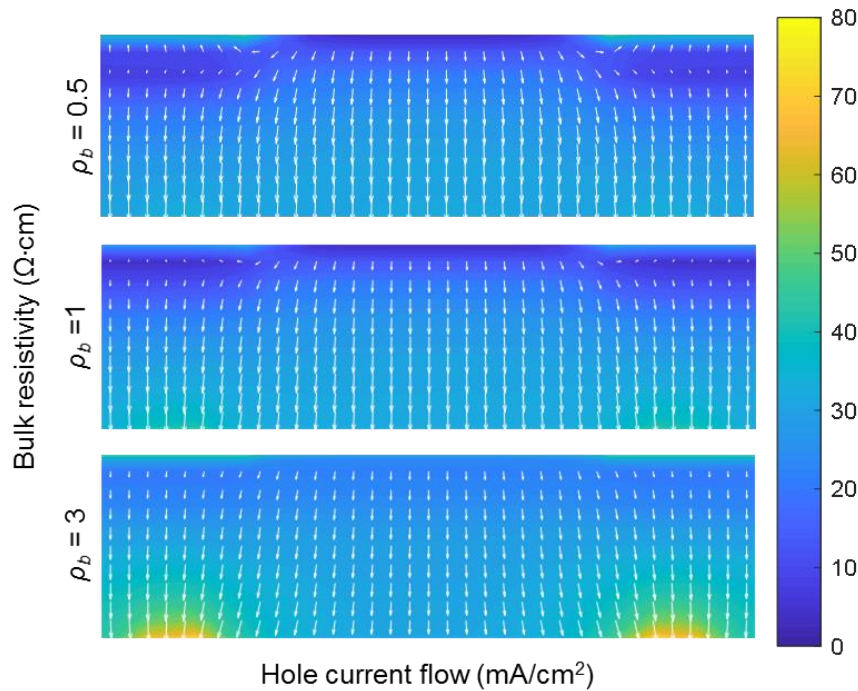

FIGURE A.III.4. The hole current flow in the bulk of the *n*-PERT-RJ unit cells with different ρ_b values simulated by Quokka3 (at the MPP condition). The white arrows represent the electrical current flow direction and the cross-section position is as same as Fig. A.III.1(d). The front Ag contact design is shown in Fig. 4.2.

The external quantum efficiency (EQE) results simulated by Quokka3 are depicted in Fig. A.III.5, which help to understand more clearly the root cause of J_{SC} loss is the adoption of low ρ_b wafers. When ρ_b is reduced below 3 $\Omega \cdot$cm, more holes couldn't be collected by the rear hole collector, resulting in lower EQE values in the wavelength interval between 400-1000 nm. This is due to the fact that some of the holes diffuse towards the front side as described in Fig. A.III.4. In addition, after the holes diffuse cross the high-low junction, there is additional recombination in the FSF, resulting in a slightly lower EQE for the lower ρ_b devices in the wavelength interval between 300-400 nm. Fig. A.III.6 summarized the impacts induced by applying different ρ_b on the *n*-PERT-RJ solar cells. When applying low ρ_b wafers, the efficiency losses caused by electron transport in FSF (coral color) and bulk (light blue) are reduced, mainly due to the reducing resistive losses. However, the efficiency losses induced by the hole transport in the bulk (blue) and the FSF recombination (orange) will increase simultaneously. The lowest ρ_b can be applied to our *n*-PERT-RJ solar cells without degrading efficiency is 1 $\Omega \cdot$cm (see Fig. 5.4).
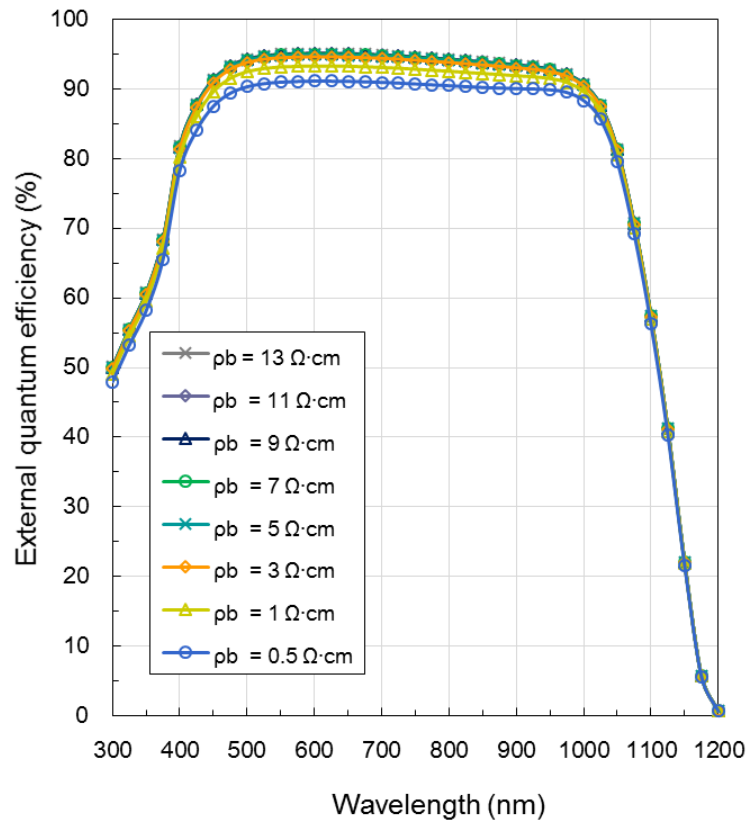

FIGURE A.III.5. The EQE of the *n*-PERT-RJ solar cells with different ρ_b values which are simulated by Quokka3. (the ρ_b varying from 0.5 to 13 $\Omega \cdot$cm).
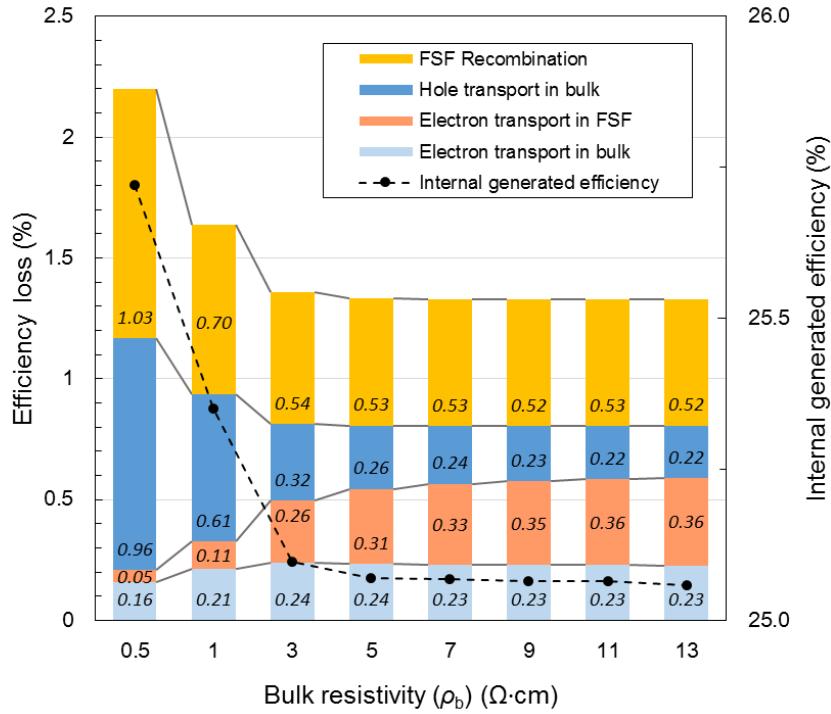
FIGURE A.III.6. The efficiency losses (at the MPP condition) of the *n*-PERT-RJ solar cells with different ρ_b values which are extracted from the FELA of Quokka3. (the ρ_b varying from 0.5 to 13 Ω·cm).

A.III.4   Degradation of the bulk lifetime induced by the decreasing ρ_b

Under one-sun illumination, ρ_b also affects the bulk lifetime. The excess minority carrier concentration (in our case is hole) at the MPP condition is lower than the bulk dopant concentration as when ρ_b is lower than 5 Ω·cm (Fig. A.III.7). When the excess carrier concentration is lower than the bulk dopant concentration, the holes have a higher possibility to be recombined and the dominated bulk recombination mechanism starts to change from SRH to Auger recombination. That is why the effective bulk lifetime of the low ρ_b at the MPP condition is much lower (see Fig. A.III.8). The bulk lifetime is particularly important to the rear junction solar cells because the minority carriers need to travel a longer distance to the rear before being collected.
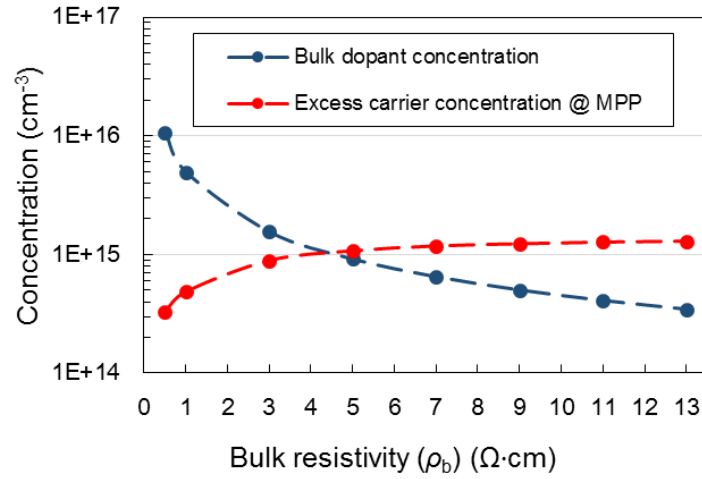
FIGURE A.III.7. For *n*-type wafers with different ρ_b values at the MPP condition, their calculated bulk dopant concentration and excess carrier concentration. The nominal bulk lifetime is 3.5 ms.
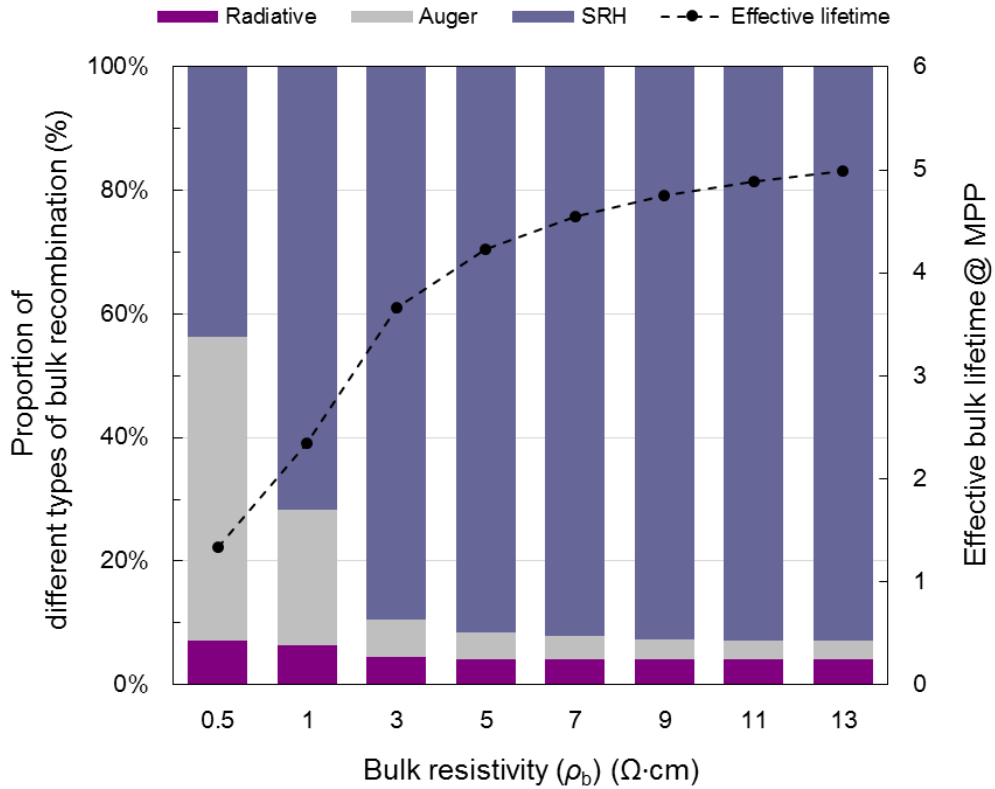
FIGURE A.III.8. For *n*-type wafers with different ρ_b values at the MPP condition, their proportion of different types of bulk recombination and effective bulk lifetime. The nominal bulk lifetime is 3.5 ms.

Curriculum Vitae

Zih-Wei Peng
06 Dec. 1985 Born in Taipei, Taiwan.
e-mail: zihw.peng@gmail.com

About
Photovoltaic (PV) scientist with 7 years of experience in n-type passivated emitter rear diffused totally (n-PERT) silicon solar cells. Design, process development and integration, simulation and characterization.

Education
PhD candidate (Chemistry) - University of Tübingen, Tübingen, Germany. 2019. Dissertation: *Development of Industrial n-PERT Rear Junction Solar Cells with Screen-Printed Aluminum Point Contacts.*

M.Sc. (Chemistry) - National Cheng Kung University, Tainan, Taiwan. 2011.

B.Sc. (Chemistry) - National Taiwan Normal University, Taipei, Taiwan. 2009.

Working experience
Oct. 2012 - Sep. 2015: R&D engineer for developing n-PERT front junction silicon solar cell at Motech Industries, Inc., Tainan, Taiwan.

Jan. 2016 - now: researcher for developing n-PERT rear junction silicon solar cell at International Solar Energy Research Center Konstanz e.V., Konstanz, Germany.

Achievements
In 2015, oral presentation, *Progress of n-PERT solar Cells / Modules Production.* The 5th International Conference on Silicon Photovoltaics, and the nPV Workshop, Constance, Germany.

In 2015, joint development of n-PERT bifacial (front junction) silicon solar cell with 2nd highest mass production cell efficiency (20.8% with 3BB grid design) in the world.

In 2018, dominant development of n-PERT bifacial (rear junction) silicon solar cell with V_{OC} beyond 690 mV by using mass production process tool.

In 2018, oral presentation, *Towards 22% Efficiency n-PERT Rear Junction Solar Cells with Screen Printed Al Point Back Contact.* The 8th International Conference on Silicon Photovoltaics, and the nPV Workshop, Lausanne, Switzerland.

In 2019, oral presentation, *693 mV Voc Industrial Screen-Printed n-PERT Rear Junction Solar Cells (MoSoN) with Stable Efficiency Beyond 22%.* The 9th International Conference on Silicon Photovoltaics, and the nPV Workshop, Leuven, Belgium.